Classification, Identification, and Modeling of Unexploded Ordnance in Realistic Environments

by

Beijia Zhang

S. B. Electrical Engineering and Computer Science
Massachusetts Institute of Technology, 2002

M. Eng. Electrical Engineering and Computer Science
Massachusetts Institute of Technology, 2004

Submitted to the Department of Electrical Engineering and Computer Science
in partial fulfillment of the requirements for the degree of

Doctor of Philosophy in Electrical Engineering and Computer Science

at the

MASSACHUSETTS INSTITUTE OF TECHNOLOGY
[June 2008]
May 2008

Author .....
Department of Electrical Engineering and Computer Science
May 16, 2008

Certified by .....
Bae-Ian Wu on behalf of Jin Au Kong
Professor of Electrical Engineering and Computer Science
Thesis Supervisor

Accepted by .....
Terry Philip Orlando
Chairman, Department Committee on Graduate Students

Classification, Identification, and Modeling of Unexploded Ordnance in Realistic Environments

by

Beijia Zhang

Submitted to the Department of Electrical Engineering and Computer Science
on May 16, 2008, in partial fulfillment of the
requirements for the degree of
Doctor of Philosophy in Electrical Engineering and Computer Science

Abstract

Recovery of buried unexploded ordnance (UXO) is very slow and expensive due to the high false alarm rate created by clutter. Electromagnetic induction (EMI) has been shown to be a promising technique for UXO detection and discrimination. This thesis uses the EMI response of buried targets to identify or classify them.

To perform such discrimination, accurate forward models of buried UXO are needed. This thesis provides a survey of existing target models: the dipole model, the spheroid model, and the fundamental mode model. Then the implementation of a new model, the spheroidal mode model, is described and validated against measurements of a UXO. Furthermore, an in-depth study of the effects of permeable soil, modeled as a permeable halfspace, is presented. This study concludes that the discontinuity created by the air to permeable soil interface produces minimal effect in the response of a buried object. The change is limited to a magnitude shift of the real portion of the EMI response and can be reproduced by superposition of a permeable halfspace response on the response of the same object in freespace. Accurate soil modeling also allows one to invert for soil permeability values from measured data if such data are in known units. However, the EMI sensor used in this study provides measurements in consistent but unknown units. Furthermore, the instrument is from a third party and is proprietary. Therefore, this thesis describes the development of a non-invasive method to model and calibrate non-adaptive instruments so that all measurements can be converted into units consistent with modeled data. This conversion factor is shown to be a constant value across various conditions, thus demonstrating its validity.

Given that now a more complete model of the measurable response of a buried UXO is implemented, this study proceeds to demonstrate that EMI responses from UXO and clutter objects can be used to identify the objects through the application of Differential Evolution

(DE), a type of Genetic Algorithm. DE is used to optimize the parameters of the UXO fundamental mode model to produce a match between the modeled response and the measured response of an unknown object. When this optimization procedure is applied across a library of models for possible UXO, the correct identity of the unknown object can be ascertained because the corresponding library member will produce the closest match. Furthermore, responses from clutter objects are shown to produce very poor matches to library objects, thus providing a method to discriminate UXO from clutter. These optimization experiments are conducted on measurements of UXO in air, UXO in air but obscured by clutter fragments, buried UXO, and buried UXO obscured by clutter fragments. It is shown that the optimization procedure is successful for shallow buried objects obscured by light clutter contributing to roughly 20 dB SNR, but is limited in applicability towards very deeply buried UXO or those in dense clutter environments.

The DE algorithm implemented in this study is parallelized and the optimization results are computed with a multi-processor supercomputer. Thus, the computational requirement of DE is a considerable drawback, and the method cannot be used for real time, on-site inversion of measured UXO data. To address this concern, a different approach to inversion is also implemented in this study. Rather than identifying particular UXO, one may do a discrimination between general UXO and general clutter items. Previous work has shown that the expansion coefficients of EMI responses in the spheroidal coordinate system can uniquely characterize the corresponding targets. Therefore, these coefficients readily lend themselves for use as features by which objects can be classified as likely to be UXO or unlikely to be UXO. To do such classification, the relationship between these coefficients and the physical properties of UXO and clutter, such as differences in size or body-of-revolution properties or material heterogeneity properties, must be found. This thesis shows that such relationships are complex and require the use of the automated pattern recognition capability of machine learning. Two machine learning algorithms, Support Vector Machines and Neural Networks, are used to identify whether objects are likely to be UXO. Furthermore, the effects of small diffuse clutter fragments and uncertainty about the target position are investigated. This discrimination procedure is applied on both synthetic data from models and measurements of UXO and clutter. It is found that good discrimination is possible for up to 20 dB SNR. But the discrimination is sensitive to inaccurate estimations of a target's depth. It is found that the accuracy must be within a 10 cm deviation of an object's true depth.

The general conclusion forwarded by this work is that while increasingly accurate discrimination capabilities can be produced through more detailed forward modeling and application of robust optimization and learning algorithms, the presence of noise and clutter is still of great concern. Minimization or filtering of such noise is necessary before field deployable discrimination techniques can be realized.

Thesis Supervisor: Bae-Ian Wu on behalf of Jin Au Kong
Title: Professor of Electrical Engineering and Computer Science

Acknowledgments

First I would like to thank my parents for supporting me and for reminding me that, regardless of everything, I am always loved and cherished. Thank you for being my protectors, advisors, teachers, confidants, and friends. Thank you for your empathy whenever I went through difficult times. Thank you for sharing my interests and fascinations. Since your education was curtailed by the Cultural Revolution in China and your opportunities in life were very limited, we came to this country and struggled through many difficult years so I would have opportunities you never had. I hope the success of my current and future endeavors makes our long journey all worthwhile. I want to share my happiness with you, always. Let us hope we will have many more cheerful memories together in good health and good spirits.

Secondly, I want to thank Dr. Kevin O'Neill from CRREL without whom none of this thesis work would have been possible. Thank you for the many patient hours you spent teaching me all about UXO and EMI. Thank you to Dr. Henning Braunisch, Dr. Chi Ao, Dr. Benjamin Barrowes, Professor Xudong Chen, and Dr. Keli Sun for their solid UXO research work which has become the foundation I have build upon. Truly, I have only come so far because I stood on the shoulders of giants.

I want to thank Dr. Robert Shin and Dr. Robert Atkins at MIT Lincoln Laboratory who took me into their fold many years ago as a bewildered sophomore and introduced me to the always stimulating and challenging world of electromagnetics research. Without their constant support, none of my graduate work could have been possible. For that and their

kindness, I will always be deeply indebted to them. Also, thank you to Dr. Joe Pacheco who has helped me out greatly in my work. And since you were my T.A., I will always look up to you as a teacher.

I would like to thank the post-docs at CETA, Dr. Tomasz Grzegorczyk and Dr. Bae-Ian Wu who have taught me how to do research and shown me how to survive being a graduate student. Thank you for always giving me your sound and thorough advice on my research work. Thank you for running our group meetings so smoothly each week. Thank you to Dr. Wu for signing this thesis and offering a detailed proof reading. Thank you both for being my teachers. I know being a post-doc must be really hard because you have to take care of grad students. I hope I did not contribute greatly to your stress levels. Thank you for your patience with me.

I want to thank Professors David Staelin and Qing Hu for serving on my thesis committee and for their comments and suggestions. Every comment is always an opportunity for me to refine my research ability. Thank you to various graduate students whom I have met in CETA and who have preceded me: Dr. Jie Lu, Dr. James Chen, and Dr. Brandon Kemp. I will always try hard to be worthy of being in the long line of PhD students who have graduated from CETA. Thank you also to Baile Zhang who will succeed me in this line. I will not forget the interesting and crazy times we had being TA's for 6.013. Thank you to the various visiting professors and students who have come through CETA. You have really enriched my understanding of research in other countries and places.

I would like to thank my high school math teacher Mrs. Voula Steinberg for being the

first one to convince me that going to MIT was entirely possible. It has been many years since your passing, but I will never forget your belief in me.

And finally, I would like to thank my professor, Professor Jin Au Kong. I still have difficulty comprehending your sudden departure from this world a few months ago. I regret that in my shyness as I stood in the shadow of your greatness, I never really let you know how grateful I was for all the help you gave me throughout my graduate career. Seven years ago I timidly asked you for a recommendation letter to get into grad school, and you joked, "Why do you want to do this crazy thing? You can live a happy life and not do this." I have always been flabbergasted by everything you have said. But what I remember most is the little joke you once made over one of our group dinners. When prompted to comment about your grad students, you said that "Beijia can do everything!" While that was just a joke and not at all true, I am still grateful for what you said. Nobody can do everything, but I want to work hard to attempt to achieve such a goal. Life is the great struggle to do the impossible because only difficult pursuits are worth following. That is why I did this crazy thing. Thank you for helping me believe in myself and allowing me to understand my capacity for learning and growth. My memory of you and your words will always propagate throughout all my future work, and it will never be evanescent.

Beijia Zhang

May 16, 2008

Contents

List of Figures

List of Tables

Chapter 1

Buried Unexploded Ordnance: General Introduction

1.1 Motivation

Buried unexploded ordnance (UXO) constitute a class of launched munitions or explosives which have not detonated and still remain in the ground despite not serving any purpose. Normally about 5 to 10% of expended munitions are "duds" and do not explode when deployed [7]. Their continued presence in the soil is dangerous due to the possibility of future detonation or the leeching of dangerous chemicals into the ground water. At present, the ability to detect and discriminate UXO with good reliability does not exist. Therefore, the clean up of land contaminated by UXO is extremely expensive and slow due to a high false alarm rate. Much of the cost of UXO clean up is expended on the pursuit of these false alarms [56] which are usually from pieces of metal refuse, shell casings of exploded ordnance,

or other remnants of civilization. A quick and reliable method to distinguish UXO from these surrounding clutter objects would be a valuable tool in aiding the clean up process. Therefore, the ultimate goal of this research is to identify buried UXO through their response signature or, more generally, distinguish UXO from clutter.

The problem of distinguishing UXO from clutter encompasses many areas of investigation. Figure 1-1 illustrates the topics of concern when addressing the UXO problem. In broad terms, one must deal with the UXO target itself, the surrounding soil environment, the nearby clutter objects, and the sensor in use. For example, signals used to detect a subsurface object may be reflected by the air-to-earth interface created by the soil or attenuated by the soil before reaching the target of interest. And nearby objects that are not of interest may create additional response signals. Large clutter items may be mistaken for UXO and contribute to false alarms. Small diffuse clutter pieces may distort the target's response.

As a result, there are several key issues that must be addressed and are the focus of each chapter in this thesis.

1. **Chapter 1**: What techniques are used to detect buried? What are the benefits and drawbacks of each?

   Given that UXO are buried, a remote detection system must be used to exploit some measurable response of the target. Since UXO are always metal, electromagnetic phenomenology can be exploited. Several techniques will be discussed, and motivation will be given for concentrating current research efforts on one of the techniques, electromagnetic induction (EMI).

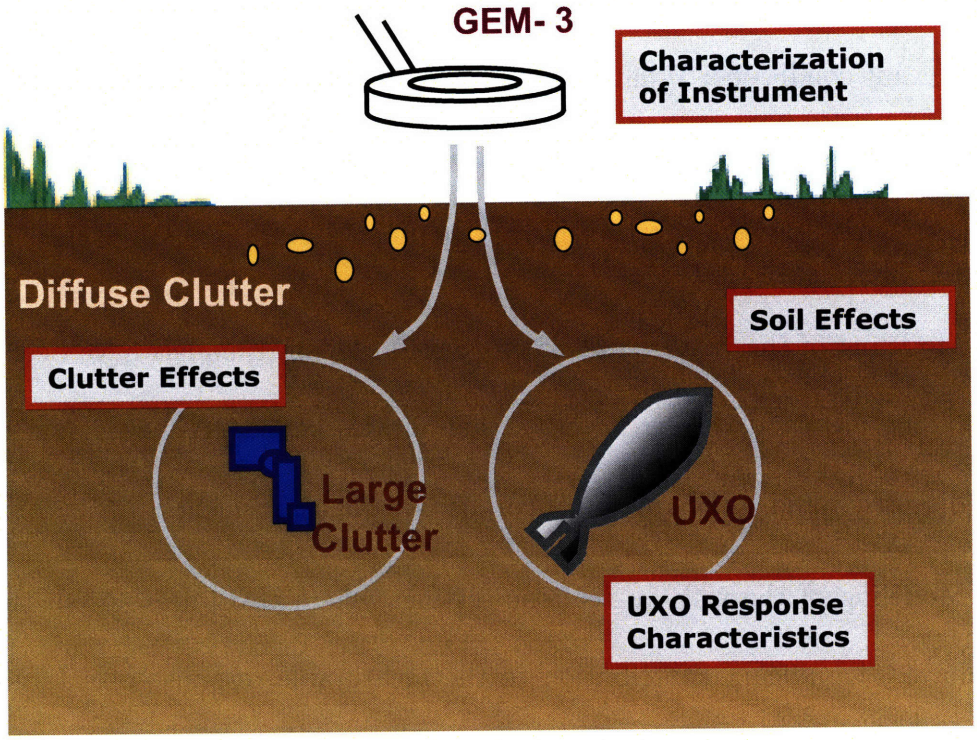

Figure 1-1: This graphic depicts an overview of the relevant areas of interest in UXO inversion research. Understanding a UXO's response characteristics is not enough to realize a method to do discrimination in a realistic setting. One must account for the effect of permeable soil and the influence of both large and small, diffuse clutter. Furthermore, the sensor in use must be characterized. The complexity of this system makes discrimination a challenging task.

2. **Chapter 2**: Are accurate forward models available? To what extent are these models accurate?

   As will be shown, distinguishing UXO from clutter first requires understanding the characteristics of the detected response for the targets of interest. This requirement can be fulfilled with forward models that are able to predict the response of targets under any relevant conditions. What distinguishes the work in this thesis is the inclusion of environmental effects and the practical implications of utilizing proprietary instruments to detect buried objects. To this effect, Chapter 2 has three main parts:

   (a) Modeling of the UXO target itself: Several forward models have been developed in the past and the strengths of each are examined. A new model for UXO is discussed, and its prediction is compared to measurements.

   (b) Modeling of the soil: In realistic settings where UXO are buried, the soil may have a significant contribution to the measurable response of a target. Understanding the extent of this effect is necessary before implementing any method to discriminate or identify buried objects. Previous work on calculating source and permeable halfspace interaction is discussed. A new approximation for the response of a halfspace with an embedded target is introduced and validated through comparison to measurements. Furthermore, soil permeability values are recovered from measured soil responses.

   (c) Modeling of the effect of the sensor: To fully understand UXO and clutter responses and to distinguish between objects, one must first be able to characterized

the sensor in use. Given that many UXO detecting instruments are proprietary and manufactured by third parties [93], part of this research is in developing a novel method to characterize instruments in a non-destructive manner. This chapter discusses this development and identifies aspects of sensors which must be analyzed prior to any identification or classification attempts.

3. **Chapter 3**: How can a UXO be identified through its electromagnetic response signature? In other words, how can sensor measurements of a buried object be inverted to produce the identity of the object?

   Once the responses of known objects are sufficiently characterized, one can match these known signals to the measured response signals of an unknown target in order to ascertain its correct identity. Identifying each particular target is one method of distinguishing UXO from clutter. Therefore, this chapter will discuss a new implementation of a searching and matching algorithm that can identify unknown objects among a library of possible candidates. The performance of this algorithm on both measured and synthetic data will be presented.

4. **Chapter 4**: What key discriminators can be extracted from UXO signatures and used to distinguish UXO from clutter? How are these features reflected in EMI measurements? What method or algorithm can be used to separate UXO from clutter on the basis of these key features?

   Rather than identifying each particular target, one may be able to extract information about their physical properties from the received response signal. UXO and clutter

items are often very physically dissimilar so unknown targets can be recognized as UXO or clutter on the basis of their distinct physical properties which can be inferred from the EMI responses. Therefore, this chapter will discuss the spheroidal mode coefficients, which can be extracted from EMI responses. These coefficients can be shown to be properties of the object and relate to the object's physical characteristics. Therefore these coefficients are well-suited for use in a classification scheme to discriminate objects that are likely to be UXO.

1.2 Overview of UXO Detection Techniques

The basis of any detection system is the exploitation of a physical phenomenology of the target that produces a response. That response may either be passively detected or actively created. Electromagnetic techniques have a long history of application in remote sensing and detection of obscured targets [10, 48, 49, 66, 93]. However, there are four principle electromagnetic techniques generally used in detecting landmines and UXO [38]:

1. **Electromagnetic induction** (EMI) relies upon the secondary magnetic field created by induced currents and possibly polarization in the buried target. EMI instruments can be further subdivided into time domain and frequency domain instruments.

   (a) **Frequency domain EMI** instruments operate at frequencies under roughly 300kHz. As will be discussed in more detail, in this regime the natural environment is transparent. These instruments are continuous wave and often incor-

porate complex designs to cancel out "primary" transmitted fields in the vicinity of the receiver so that only secondary fields are measured.

(b) **Time domain EMI** instruments saturate the target with a static magnetic primary field and record any transient response once the primary field is shut off. One large disadvantage is that instead of querying the object equally at all frequencies like frequency domain EMI instruments, time domain instruments only provide a response equivalent to an unevenly weighted frequency response of the object. Very late time transients past 0.01 seconds, corresponding to low frequency responses roughly below 100 Hz, are often poorly represented in time domain responses. As will be shown, much discriminatory ability can be derived from the behavior of a target at extremely low frequencies.

2. **Ground penetrating radar (GPR)** describe frequency domain instruments operating usually in the range of 50 MHz to about 1000 MHz. While often useful in locating the depth of UXO targets because GPR can resolve objects on the order of one half a wavelength, GPR is often hampered by signficant noise due to soil [16, 70]. Even in only moderately conducting media such as clay or wet soils, GPR often has poor penetration.

3. **Magnetometers** are passive instruments which utilize the Earth's natural magnetic fields and detect the minute perturbations of the fields caused by ferrous objects. These instruments are therefore only usable on ferrous objects and have limited resolution.

4. **Infrared cameras** are passive instruments that utilize the different heat transfer

properties of soil that does and does not contain UXO targets. Thermal contrast can be seen with such cameras. However, this method is highly dependent on surface vegetation, time of day, and weather conditions.

While each of these sensing techniques has its proponents within the UXO research community, the relative transparency of background media when using the EMI method is highly attractive. Thus, the majority of the research presented in this thesis involves using frequency domain EMI data to distinguish UXO from clutter.

1.3 EMI Background

When an time varying electromagnetic field interacts with a conducting body, electric currents will be induced on the target. At higher frequencies for wavelengths on the order of a meter or less, this activity is confined to the surface and scattering of the incident waves occurs. The general behavior has been extensively studied [82]. Radar is a common example of a useful application of this phenomenon. For electromagnetic waves at very low frequencies where the wavelengths are on the order of kilometers, the induced currents can penetrate into imperfectly conducting targets and are called "eddy currents." These eddy currents create a secondary magnetic field which can be detected by the appropriate sensors. Furthermore, permeable targets will have a magnetic polarization aligned with the incident magnetic field.

Detecting the currents and magnetic polarization induced by low-frequency magnetic fields forms the basis of the electromagnetic induction (EMI) technique which has been

regarded as a useful tool in UXO detection and discrimination [10, 49]. In this method, a magneto-quasistatic field of under roughly 300 kHz is transmitted above ground, near the buried object of interest. This field generates currents in conducting targets and also magnetic polarization in permeable targets. The currents and possible polarization in the target produce additional magnetic fields. These induced "secondary" magnetic fields are picked up by a receiver, often a wire loop. The received signals can then be studied in the time domain or frequency domain to identify buried objects as UXO or to distinguish potential false alarms [18, 37].

1.4 EMI Formulation and Assumptions

Quasistatic approximations can be shown to be valid under certain conditions. Maxwell's equations are applicable at all frequencies [50]. From Ampere's Law,

$$\nabla \times \vec{H} = \sigma \vec{E} - i\omega\epsilon\vec{E} \tag{1.1}$$

one can take the curl and apply Gauss's Law and Faraday's Law to obtain

$$\nabla^2 \vec{H} = -i\omega\sigma\mu\vec{H} - \omega^2\mu\epsilon\vec{H} \tag{1.2}$$

for homogeneous media. In all calculations, homogeneous media are assumed. The first term on the right of Equation 1.2 is the conduction current and the second term is the displacement current. In the low frequency quasistatic regime, the displacement current can be neglected

in comparison to the much larger conduction current [40, 76]. This approximation leads to the diffusion equation,

$$\nabla^2 \vec{H} = -i\omega\sigma\mu\vec{H}. \tag{1.3}$$

No true waves are generated because $i\omega$ represents only the first derivative with respect to time.

It behooves the UXO researcher to then demonstrate that this quasistatic approximation is indeed accurate for the frequency range of the EMI detection and for the problem at hand. Generally, there are three media of interest in the UXO problem: air, soil, and the metal which comprises the target.

1.4.1 Quasistatic Argument for Air

Air is normally regarded as freespace. In freespace, there is no conduction current term. However, given that top of the EMI frequency range is 300 kHz, the corresponding wavelengths of interest are one kilometer or more. In the UXO problem, the typical distances between sensor and target are on the order of one meter. Thus, over these short distances, the field is essentially static, and the displacement current can also be ignored. Therefore, the magnetic fields in air are irrotational with $\nabla \times \vec{H} = 0$ and can be represented by the gradient of a scalar potential,

$$\vec{H} = -\nabla U. \tag{1.4}$$

1.4.2 Quasistatic Argument for Metal

In the interior of the spheroid, one can be justified in ignoring the displacement current and assuming quasistatic conditions because the ratio of conduction current to displacement current, $\sigma/\omega\epsilon$, is very large for even a worse case scenario: a relatively high EMI frequency of $\omega = 10^6$ rad/s acting on a moderately conducting object of 10^5 S/m, typical of some poorly conducting metals, with ϵ on the order of 10^{-10} F/m. Given that the objects of interest normally have $\sigma \approx 10^7$ S/m, one can see Equation 1.3, the diffusion equation, is valid.

1.4.3 Quasistatic Argument for Soil

One can demonstrate that the EMI magnetic fields can be considered irrotational even in slightly conducting media like soil. Soil conductivity is very reasonably assumed to be $\sigma < 10^{-2}$ S/m. Poorly conducting dry soil is on the order of 10^{-3} S/m, and a reasonable lower bound would be 10^{-4} S/m [14]. First one can confirm that displacement current does not exceed conduction current through an examination of the ratio between highest possible displacement current and lowest possible conduction current. The permittivity of soil cannot reasonably be expected to exceed a value on the order of 10^{-9} F/m. And the highest frequency ω of interest is of order 10^5 rad/s. Even under these extreme conditions, one can see that displacement current cannot significantly exceed conduction current. At worst these two values are on the same order.

Next, one can further demonstrate that the conduction current is also negligible. Due to boundary conditions, the electric field $\vec{E}$ will be on the same order of magnitude both

inside the conducting target and in the soil immediately surrounding that object. Therefore the ratio of currents in metal and soil will be approximately equal to the ratio of their conductivities. Considering that the metal targets of interest have conductivities on the order of 10^6 S/m or greater, the relative conduction current even in warm seawater with $\sigma \sim 25$ S/m would still be comparably small [47]. Therefore, in soil, both right hand terms of Equation 1.2 can be considered zero, producing an an irrotational field that can be obtained from the gradient of a scalar potential satisfying the Laplace Equation as shown in Equation 1.4.

While a background medium similar to soil will produce no challenge to the validity of the quasistatic assumption, this analysis does not fully describe the EMI response of permeable soil. Even a weakly magnetic soil will create a halfspace response due to the air to soil interface. Furthermore, the soil to air discontinuity of strongly magnetic soil may interact with the target. Part of the research presented in subsequent chapters will address the impact of the soil and any ramifications it may create on distinguishing UXO from clutter.

1.5 The Behavior of UXO Responses to EMI Excitation

A typical EMI response of a metal object to a uniform excitation is shown in Figure 1-2. The object is a permeable sphere with $\sigma = 2 \times 10^6$ S/m, radius $a = 0.05$ m, and $\mu = 100\mu_0$. In the figure, "I" denotes the response that is in phase with the excitation and "Q" denotes

the response that is in phase quadrature with the excitation. I and Q correspond to the real and imaginary parts of the secondary field, respectively. In the geophysics convention, the I term is always plotted so that its sign is reversed.

The trends and characteristics of this plot can be more easily understood by examining the high and low frequency limits. At near static frequencies, the response is mainly due to the magnetic polarizability of the object. The response will align itself with the incident magnetic field and be wholly Inphase. If the object were not permeable, very little response would be seen at the low frequency end of the EMI spectrum. At the highest frequencies, activity will be largely limited to surface currents that generate an opposing response as stated by Lenz's law and again will be entirely Inphase but of opposite sign. At mid-frequencies, the finite conductivity of the target provides resistance as volume currents circulate within the target in their attempt to oppose changes in the primary field. Therefore, the secondary magnetic fields produced by these currents will lag behind the incident magnetic field and produce a significant Quadrature response.

In the mid-frequency range, there is a frequency where peak Quadrature–implying peak volume current–occurs. For permeable objects, this quadrature peak is related to a time constant τ where $f_{peak} = 1/(2\pi\tau)$. Time constant τ is given by $\tau = a^2\sigma\mu/\mu_r^2$ where $\mu_r = \mu/\mu_0$. This time constant relates to the exponential decay rate for the fundamental mode of the sphere when subject to a step down excitation [7,9]. Therefore, the quadrature peak can be associated with the lowest dominate decay mode which creates peak volume current effects. As one can see, much information about the physical characteristics of the target

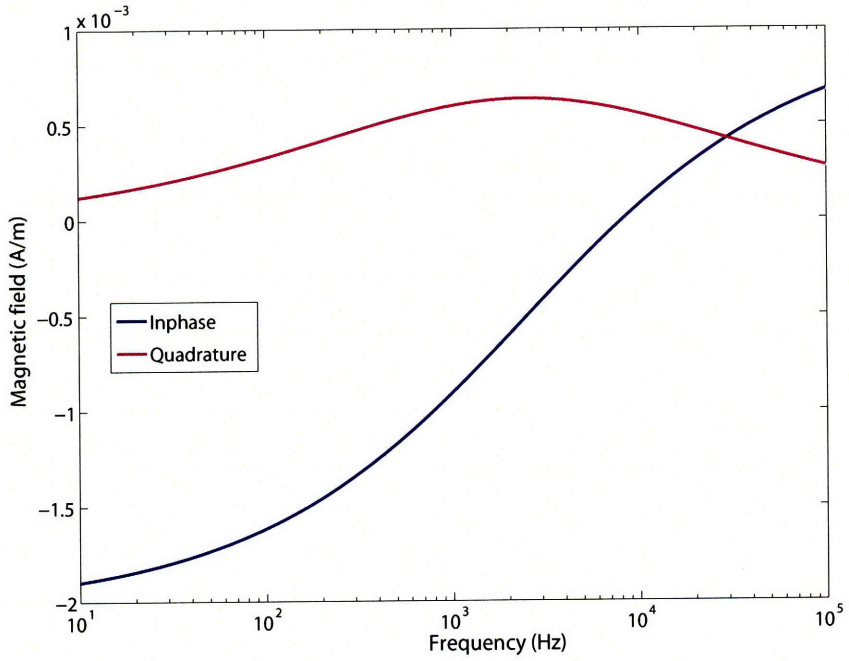

Figure 1-2: This graphic shows a typical EMI response. The response is calculated using a model of a steel sphere. Examining an object's response over frequency provides information about its physical characteristics which may be used to discriminate UXO from clutter.

can be gained by studying the EMI response as a function of frequency.

An object's EMI response with respect to orientation and position can also be studied. Figure 1-3 shows the measured Inphase response at 47,970 Hz of the UXO shown in Figure 1-4. All measurements contained in this thesis were conducted by the US Army Cold Regions Research and Engineering Laboratory (CRREL). All photographs contained in this thesis are courtesy of CRREL as well. The object is located at the origin with the nose pointed in the northeast corner. This thesis identifies UXO types by their Aberdeen Test Center (ATC) number. In Figure 1-4 the UXO is ATC118.

The measurements shown in Figure 1-3 are made by a frequency domain EMI monostatic

sensor on a 7 by 7 square grid with 10 cm spacing. The sensor's receiver coil lies within and in the plane of the transmitter coils. A more detailed discussion of the sensor is provided in Chapter 2.4. When the instrument is near the UXO, a stronger response is naturally generated. When the distance between the target and sensor is greater, the response is much weaker. Despite the object being located at the origin, the peak of the response is slightly shifted towards the northeast corner. This shift agrees with the known orientation of the object: when the incident magnetic fields are most aligned with the axis of the UXO, the strongest response is produced. As this example indicates, studying the response of a UXO for various positions relative to an EMI sensor can provide some insight into the object's orientation and location.

It is this study of an object's EMI response as a function of frequency, orientation, and position which enables one to distinguish between objects or to identify objects. As will be shown in subsequent chapters, the responses of UXO are often obfuscated by the environment, sources of noise, and the complexity of the targets themselves. Therefore, as discussed in the next chapter, modeling of the targets and their surrounding environments are needed before any discriminatory capability can be assessed.

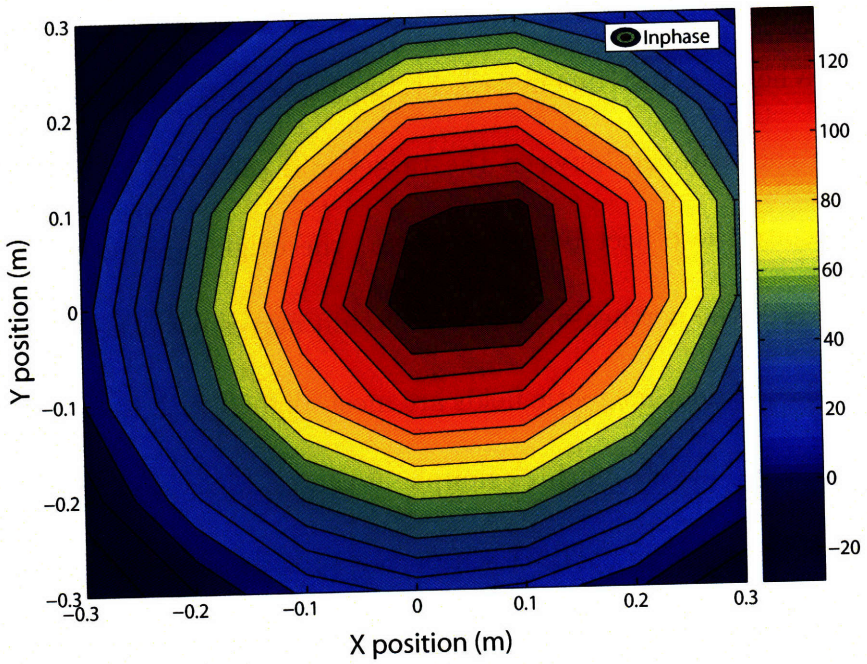

Figure 1-3: This graphic shows the Inphase EMI response measured from UXO ATC118. The measurement was taken with a monostatic EMI sensor. Examining an object's response at many sensor and receiver positions provides much information about the target's orientation and location. All measurement data contained in this thesis were obtained by the US Army Cold Regions Research and Engineering Laboratory (CRREL).

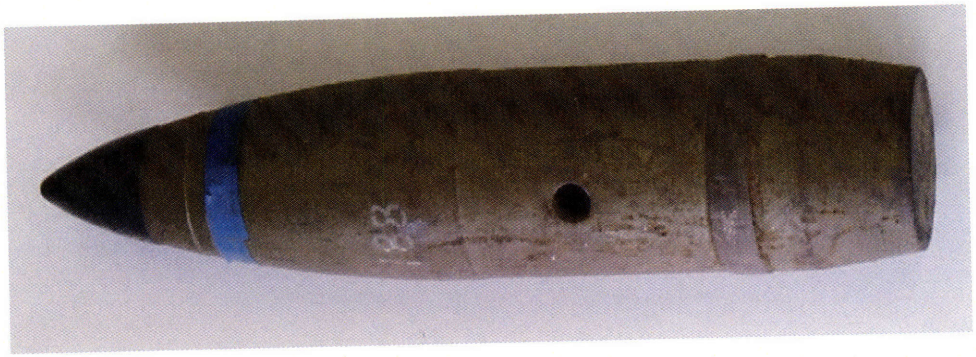

Figure 1-4: This UXO is ATC118. UXO are identified in this thesis by their Aberdeen Test Center (ATC) number. Photograph is courtesy of CRREL.

Chapter 2

UXO, Soil, and Sensor Modeling

2.1 Introduction

The goal of reducing false alarms can be addressed by identifying or classifying buried objects based on their EMI response. However, to perform such discrimination, forward models are needed beforehand to predict the secondary magnetic fields produced by targets under various conditions. Many inversion techniques require some prior knowledge of the target's response under specific conditions. Normally, it is not financially or logistically feasible to take measurements of UXO or related targets for every orientation and position of interest. Therefore, forward models form an integral part of inversion research. Furthermore, accurate forward models of UXO or similarly shaped metal objects form a critical part of the understanding of their response to EMI stimuli.

What largely distinguishes the work discussed in this thesis from all previous forward modeling work is the attention to modeling UXO within realistic environments and using

real instruments. This complete model consolidates the effects of soil and the effect of the relationship between actual secondary EMI fields and the measured fields as reported by the sensor. All previous modeling work was limited to modeling targets in freespace. Accurate modeling of the measured EMI response of buried UXO in realistic environments is comprised of three key components: the UXO itself, the soil, and the sensor in use.

2.2 UXO and Target Modeling

This section will first provide an overview of pre-existing frequency domain models for canonical shapes and for UXO targets. Then, a new modeling method is introduced and validated against measured data. These models predict the responses of UXO or canonical shapes in freespace. The investigation into the effect of permeable soil on a buried object's response will be discussed in the subsequent section.

2.2.1 Previous Work: Existing Models for Target Object

2.2.1.1 Dipole Model

The tri-axial magnetic dipole model is a well studied and popular model for UXO [10, 99]. The target is assumed to respond like an infinitesimal magnetic dipole. This assumption is founded on rigorous known physics: the dipole response is more dominant than any higher order response modes because it decays at a slower rate. This model is widely used mostly due to its simplicity and low computational cost.

Within the framework of the dipole model, targets are characterized by an infinitesimal

dipole with a frequency dependent magnetic polarizability tensor $\overline{\overline{M}}$. The magnetic field response, also known as the secondary field $\vec{H}^{\mathrm{S}}$, can then be calculated by,

$$\vec{H}^{\mathrm{S}}(\vec{r}) = \frac{3\hat{r}\hat{r} - \overline{\overline{I}}}{4\pi r^3} \cdot \vec{m} \tag{2.1}$$

where

$$\vec{m} = \overline{\overline{M}} \cdot \vec{H}^{\mathrm{PR}} \tag{2.2}$$

and where $\vec{H}^{\mathrm{PR}}$ is the primary field at the location of the target. The unit vector $\hat{r}$ and r denote the direction and distance from the target to the observation point, respectively.

Thus, with prior knowledge of the target's location, of the value of $\vec{H}^{\mathrm{PR}}$ at that location, and of the value of $\overline{\overline{M}}$ over frequency, Equation 2.1 can be used to predict the secondary magnetic field response in the frequency domain over all observation points. Obtaining an analytical expression for $\overline{\overline{M}}$ is normally difficult except for simple canonical objects like permeable, conducting spheres. Unlike general objects, a homogeneous sphere will only produce a dipole response to a uniform primary field. In other words, Equation 2.1 is complete and accurate in describing the response for such a sphere excited by a uniform field.

For objects other than a sphere, the corresponding, best fitting $\overline{\overline{M}}$ can be found by noting that Equation 2.1 is a set of linear equations for samplings of $\vec{H}^{\mathrm{S}}$ at multiple receiver positions. Therefore, one can solve for $\overline{\overline{M}}$ given enough data about $\vec{H}^{\mathrm{S}}$, paired with knowledge of the location of the target and the value of $\vec{H}^{\mathrm{PR}}$ at that location.

Figure 2-1: UXO ATC118 has composite geometry and material composition. The heterogeneous nature of many UXO makes the dipole model a very poor representation of their EMI response. Photo courtesy of CRREL.

Solving for the magnetic polarizability tensor of a target in this fashion can be viewed as falling under the inversion portion of UXO research while solving for $\vec{H}^{\mathrm{S}}$ through Equation 2.1 falls under the domain of forward modeling.

Limitations of the Dipole Model

While the dipole model is suitable for many types of buried targets, it can be shown to be ill-suited for heterogeneous objects comprised of dissimilar metals. Many UXO objects are of this nature as shown in Figure 2-1. This UXO is composed of many different metals.

As mentioned, given measurements from non-canonical objects, one can still apply the dipole model by finding the optimal equivalent polarizability matrix that fits the data. However, the fitting may be poor, and there is no guarantee that the equivalent polarizability matrix will be unique for the given target [77]. Arguments have been advanced for model-

ing these heterogeneous objects with two or more independent dipoles [99]. But as shown in [77], this method is prone to over-fitting data and providing non-unique solutions. The issue of non-uniqueness in the recovered dipole parameters also creates difficulty in using these parameters as discriminators in any inversion method. Clearly there is a need for both more powerful models and more unique object discriminators in UXO research.

2.2.1.2 Spheroid Model

To satisfy the need for a more powerful model, a broadband EMI spheroid model was developed at Center for Electromagnetic Theory and Applications (CETA) from 1998 to 2004 [3,5,12]. This model predicts the frequency domain EMI responses from metal spheroids of arbitrary conductivity and permeability values in response to any excitation. Spheroids are a good approximation for UXO because many UXO are elongated bodies of revolution and are similar in shape to spheroids.

This model of the EMI response of spheroids is based on using spheroidal coordinate system equations characterizing the magnetic fields interior and exterior to the object and then matching boundary conditions. It is most natural to use the spheroidal coordinate system, as shown in Figure 2-2, because the surfaces of the spheroids can then be defined with only one coordinate parameter ξ when the spheroidal coordinate system is chosen with the same foci as those which define the spheroid of interest [34]. The spheroidal coordinate system is a 3 dimension orthogonal coordinate system, resulting from rotating the two dimensional elliptic coordinate system about the axis containing the foci.

As previously argued, all magnetic fields exterior to the target can be considered to be

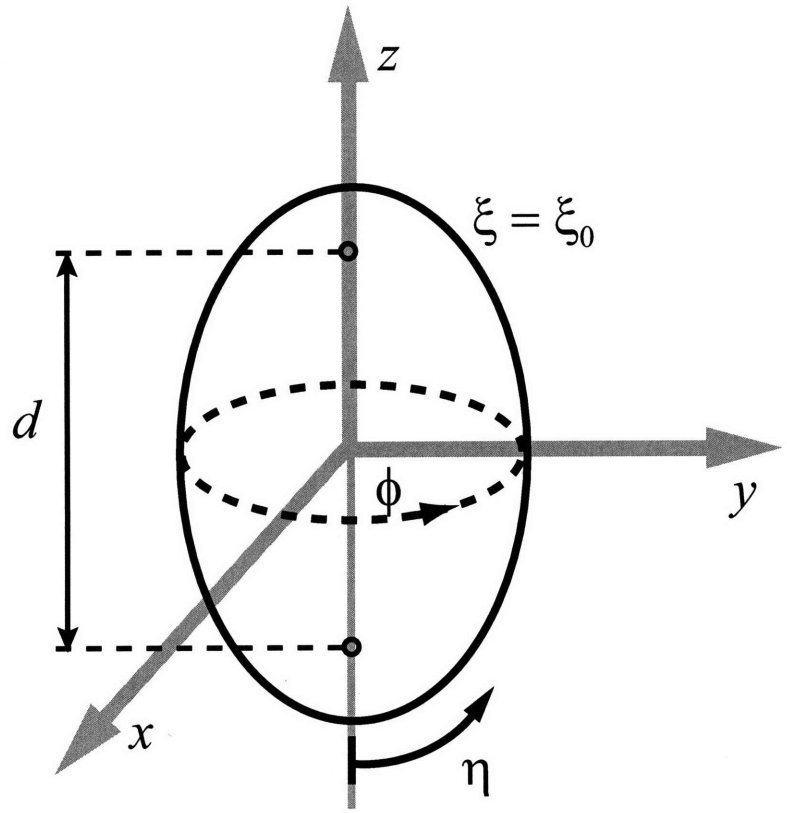

Figure 2-2: The spheroidal coordinate system. d refers to the interfocal distance. ξ indicates the particular spheroidal surface. ϕ is the rotational angle, and η refers to the distance along the surface ξ.

irrotational for the low frequencies and poorly conducting background media of interest. Therefore, the primary and secondary magnetic fields outside of the metal object can be written in terms of the gradient of a scalar potential: $U^{\mathrm{PR}}(\vec{r})$ for the primary potential created by the transmitter and $U^{\mathrm{S}}(\vec{r})$ for the secondary potential created by the object. Furthermore, these two potentials can be expressed as a linear superposition of a finite number of modes, each of which is a solution to Laplace's Equation in the spheroidal coordinate system:

$$U^{PR}(\vec{r}) = \frac{d}{2} \sum_{m=0}^{\infty} \sum_{n=m}^{\infty} \sum_{p=0}^{1} b_{pmn} P_n^m(\eta) P_n^m(\xi) T_{pm}(\phi) \tag{2.3}$$

$$U^{S}(\vec{r}) = \frac{d}{2} \sum_{m=0}^{\infty} \sum_{n=m}^{\infty} \sum_{p=0}^{1} B_{pmn} P_n^m(\eta) Q_n^m(\xi) T_{pm}(\phi), \tag{2.4}$$

where

$$T_{pm}(\phi) = \begin{cases} cos(m\phi) & p = 0 \\ \\ sin(m\phi) & p = 1 \end{cases} \tag{2.5}$$

and where $\vec{r}$ refers to the observation location. Coordinates are defined in terms of ξ which indicates a spheroidal surface and η and ϕ which describe the azimuthal and rotational positions, respectively. In Equations 2.3 and 2.4, $P_n^m()$ and $Q_n^m()$ are the associated Legendre functions of the first and second kind. The parameter d is the interfocal distance of the spheroidal coordinate system. The different permutations of the summation indices (p, m, n) indicate the different modes of the equations. For the sake of compactness, one can write (p, m, n) using one index, each value of which corresponds to one permissible combination

of p, m, and n. Thus, index j is used for the primary potential, and the index k is similarly used for the secondary potential. Furthermore, one can represent the associated Legendre functions and T_{pm} using the symbols Ψ_j^{PR} in Equation 2.3 and Ψ_k^{S} in Equation 2.4. Using this notation, Equations 2.3 and 2.4 become Equations 2.6 and 2.7, respectively:

$$U^{\mathrm{PR}}(\vec{r}) = \frac{d}{2}\sum_j b_j \Psi_j^{\mathrm{PR}}(\vec{r}) \tag{2.6}$$

$$U^{\mathrm{S}}(\vec{r}) = \frac{d}{2}\sum_k B_k \Psi_k^{\mathrm{S}}(\vec{r}). \tag{2.7}$$

The primary and secondary magnetic fields can be obtained by taking the gradient of Equations 2.3 and 2.4:

$$\vec{H}^{\mathrm{PR}}(\vec{r}) = \frac{-d}{2}\sum_j b_j \nabla\Psi_j^{\mathrm{PR}}(\vec{r}) \tag{2.8}$$

$$\vec{H}^{\mathrm{S}}(\vec{r}) = \frac{-d}{2}\sum_k B_k \nabla\Psi_k^{\mathrm{S}}(\vec{r}). \tag{2.9}$$

The total magnetic field external to the spheroid can be written as a sum of the primary and secondary fields, i.e.,

$$\vec{H}_1 = \vec{H}^{\mathrm{PR}} + \vec{H}^{S} = -\nabla U^{\mathrm{PR}} - \nabla U^{\mathrm{S}}. \tag{2.10}$$

In the quasi-magnetostatic regime, the magnetic field inside the spheroid satisfies the vector wave equation,

$$\nabla \times \nabla \times \vec{H}_2 - k_2^2 \vec{H}_2 = 0 \tag{2.11}$$

where $k_2^2 = i\omega\sigma_2\mu_2$ for a metal target of permeability μ_2 and conductivity σ_2. This field can be expanded using the divergence free vector spheroidal wavefunctions, $\vec{M}$ and $\vec{N}$, of the first kind [34] and which are regular at the origin:

$$\vec{H}_2 = \sum_{m=0}^{\infty}\sum_{n=m}^{\infty}\sum_{p=0}^{1}[A^M_{pmn}\vec{M}^{r(1)}_{pmn}(c_2;\eta,\xi,\phi) + A^N_{pmn}\vec{N}^{r(1)}_{pmn}(c_2;\eta,\xi,\phi)] \tag{2.12}$$

where

$$c_2 = k_2 d/2 \tag{2.13}$$

in which d is the interfocal distance of the spheroid.

Low Frequency: Exact Solution

By solving Equation 2.12 and matching the boundary conditions,

$$H_{1\eta} = H_{2\eta} \tag{2.14}$$

$$H_{1\phi} = H_{2\phi} \tag{2.15}$$

$$\mu_1 H_{1\xi} = \mu_2 H_{2\xi}, \tag{2.16}$$

one can solve for B_k of the target once the primary field is specified. Since the primary field is described as modes associated with b_j then B_k can be expanded into B_k^j . Here k indicates the response modes for any particular incident mode j. Further discussion of this expansion

is provided in Section 2.2.2.

There are two limitations to applying this solution [5]. First, the angular and radial spheroidal wave functions are generally not orthogonal to each other. Therefore, infinite sets of equations arise when matching the boundary conditions. To deal with this issue, normally this set of equations is truncated. The truncation point relates to highest order mode of interest [3].

The second, more pressing limitation is that the radial and angular spheroidal wavefunctions are only readily computed for low frequencies due to numerical instability at higher frequencies, Therefore, the exact solution for the spheroidal wavefunctions is only available up to $c_2 = k_2 d/2 \approx 30$. The computational limit occurs at lower frequencies for more elongated spheroids and for highly permeable and conducting spheroids [4]. This limitation is of great concern since UXO tend to be highly conducting, often highly permeable, and elongated. Therefore approximations are used at high and mid frequencies.

High Frequency: Small Penetration Approximation

At very high frequencies, calculating the wavefunctions of Equation 2.12 can be avoided by assuming that all internal fields of the target are only nonzero in a thin layer beneath the surface. Under this assumptions, the equations governing the tangential components of the magnetic field at the surface become decoupled and are in the form of differential equations. The technique was dubbed Small Penetration Approximation (SPA) [3].

Mid Frequency: Asymptotic Expansion of the Spheroidal Wave Function

In the frequency range between the domains where the exact solution and SPA method are applicable, asymptotic approximations of the angular and radial spheroidal wave functions are shown to provide less than 5% error for spheroids with aspect ratio of $(1/6) < e < 6$ when compared to the numerical finite element/boundary integral method [5, 6]. The implementation of this method for the mid-frequency range completed the broadband forward model for the EMI response of metal spheroids [5].

2.2.1.3 Fundamental Mode Model

The previously described forward model provides the solution for the canonical spheroid shape. While it is a good approximation for many targets of interest, real UXO are often materially heterogeneous and have a more complicated geometry. Numerical models may accurately describe more complex targets but are too slow to be utilized in many inversion schemes. In response to the need for accuracy and speed, a model based on the superposition of analytically specified modes of excitation for specific UXO types was implemented [79]. In this method, for each unit magnitude spheroidal excitation mode, corresponding to b_j, the response of the target is represented by a number of rings of magnetic charges located on an auxiliary spheroid surface surrounding the target. The amplitudes of the magnetic charges for any arbitrary target can be recovered from sufficient measurement data.

Once these charge values are known for an object, future modeling of that particular target would entail only decomposition of the excitation into a sum of fundamental modes and

summation of corresponding magnetic fields created by charges associated with each mode. Therefore, this model is very fast. However, this model requires detailed EMI measurements of every object one wishes to model in order to create the corresponding database of magnetic charges. Such extensive measurements may not be possible particularly for clutter objects which encompass a wide range of geometries and materials. Typically the model is limited to selected items of interest. In this regard, despite the potential accuracy of the fundamental model model, the spheroid model is not rendered obsolete since it does not depend on measurements. The spheroid model can produce EMI responses for a wide range of random spheroid shapes from extremely, long pencil-like prolate spheroids to extremely flat disk-like oblate spheroids of any arbitrary permeability and conductivity. As will be discussed, one can also construct assemblages of spheroids to model complex objects. This ability to model a wide range of objects will be shown to be of great use for inversion schemes based on machine learning in a subsequent chapter.

2.2.2 Spheroidal Mode Model for UXO

The spheroidal mode model for UXO is a natural extension of the prior research into retrieving spheroidal mode coefficients from data [18] and is similar in structure to the fundamental mode model. It must be emphasized that the spheroidal mode model is distinct from the spheroid model. The spheroid model is analytical and only models spheroids. The spheroidal mode model–though drawn from the analytical framework of the magnetic response in the spheroidal coordinate system–is similar to the fundamental mode model in

that its parameters are obtained from EMI measurement data and can model metal objects of any shape provided sufficient measurements are available. Whereas the fundamental mode model describes objects using sets of magnetic charges, the spheroidal model model utilizes the coefficients of the spheroidal modes of the target's response.

In preceding sections, it was shown that in the spheroidal coordinate system, the magnetic fields exterior to the target can be represented using analytical modes. Suppose only one unit magnitude excitation mode j is incident on the target. Let $\vec{H}_j^{\mathrm{S}}$ represent the secondary field response to that single unit excitation mode j. Then for any arbitrary excitation, the secondary response is the sum of the response to each unit magnitude mode of the primary excitation, scaled by the corresponding strength of each excitation mode which is given by b_j. This expansion is shown as the first equivalency in Equation 2.17.

$$\vec{H}^{\mathrm{S}}(\vec{r}) = \sum_j b_j \vec{H}_j^S(\vec{r}) = \sum_j b_j \frac{-d}{2} \sum_k B_k^j \nabla \Psi_k^S(\vec{r}). \tag{2.17}$$

Taking the middle part of Equation 2.17 one step further, one can decompose $\vec{H}_j^{\mathrm{S}}$ in the same manner as done for $\vec{H}^{\mathrm{S}}$ in Equation 2.9 to obtain the B_k^j coefficients as given in the second equivalency of Equation 2.17. These coefficients correspond to the kth mode of the spheroidal response to the jth mode of the spheroidal excitation. They are independent of the particular primary excitation used since information about the primary field is in b_j with all position and orientation effects encompassed by $\nabla \Psi_k^{\mathrm{S}}$. As a result, for any specific spheroidal coordinate system defined by the interfocal distance d, axis orientation, and a chosen origin, the B_k^j only depend on the physical properties of the target. In addition, it

can be rigorously, mathematically proven that all objects with unique EMI responses also have unique B_k^j coefficients [3,5]. Obtaining an object's B_k^j coefficients is sufficient to create a model of its frequency domain response to any form of excitation.

2.2.2.1 Retrieval of Spheroidal Coefficients from Data

The successful recovery of B_k^j from secondary magnetic field data was shown by [18]. The reader is directed to that reference for detailed discussion. However, it remains beneficial to understand the general framework by which one can obtain the B_k^j used in this study. The previous discussion on the spheroid model involved matching boundary conditions and finding B_k^j analytically. As shown, this method is difficult even for canonical shapes due to computational issues.

However, one can understand that Equation 2.17, which relates B_k^j to the secondary magnetic field, describes a system of linear equations. Given sufficient measurements of the magnetic field, $\vec{H}^S$ at varying observation positions, it is possible to solve for B_k^j in a least squares manner very similar to how one would recover the diagonal elements of the magnetic polarizability matrix under the dipole model framework. In matrix form, $\nabla\Psi_k^S$ becomes a $M_p \times N_{jk}$ size matrix where M_p is the number of measurements available and N_{jk} is the product of the number of j and k modes required to form an accurate solution. In theory there are infinitely many j and k modes, but recovering the values of B_k^j requires the creation of a finite matrix and also, as consequence, the truncation of these modes. Futhermore, the selection of particular modes one wishes to invert for is also critical. As discussed in greater detail in [18], attempting to recover higher order modes often leads to

an ill-conditioned matrix. That reference gives a listing of the lowest order modes which are j = (0,0,1), (0,0,2), (0,1,1), (1,1,1), (0,0,3), (0,1,2), (1,1,2) and k = (0,0,0), (0,1,1), (1,1,1), (0,0,1), producing a total of 28 B_k^j coefficients. These low order modes dominate the solution and are sufficient to reproduce it [18, 19]. Therefore, all studies presented in this thesis will be limited to to the aforementioned 28 B_k^j coefficients.

2.2.2.2 Formation of Model: Synthetic Composite Object

To demonstrate the viability of using B_k^j recovered from an object's EMI response to make predictions of the object's response to any arbitrary EMI stimuli, one can compare such predictions to the predictions made by independently validated models or with measurements of the target of interest. It is useful to first do this validation with synthetic data before using measured data.

Modeling of Composite Objects Using the Spheroid Model

A composite object which is half steel, half aluminum, and orientated horizontally as shown in Figure 2-3 can be modeled through the superposition of the response of a steel spheroid with an aluminum spheroid. This superposition creates an accurate approximation for the response of a heterogeneous object when only one component is permeable [72].

The permeable portion has $\mu_r = 100$ and $\sigma = 2 \times 10^6$ S/m. The non-permeable portion has $\sigma = 2 \times 10^7$ S/m. Each spheroid is 15 cm long along the major axis and 10 cm long along the minor axis.

For each spheroid, the secondary fields are calculated for 7 by 7 grids with 10 cm spacing

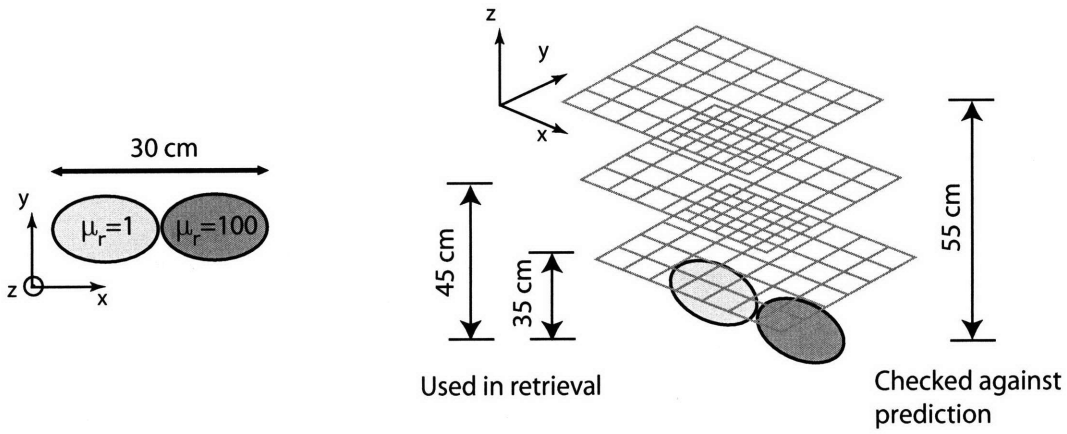

Figure 2-3: Plot depicts the orientation and position of the composite object for the calculated response shown in Figure 2-4. Object position and orientation is fixed for all calculations and predictions.

on observation planes at 0.35 and 0.45 meters above the target. To mirror the behavior of the actual measurement sensor in use [93], the transmitter and receiver are modeled as current carrying coils colocated within the same head. Therefore, all measurements are taken in a monostatic manner. The particulars of instrument modeling are discussed more throughly in Section 2.4.

Resolving B_k^j for each spheroid as given in Equation 2.17 requires calculation of $\nabla\Psi_k^{\mathrm{S}}$ and b_j. Given that the measurement positions relative to the spheroid location are known, $\nabla\Psi_k^{\mathrm{S}}$ can expressed analytically. The b_j coefficients are not analytically known for the excitation created by a current carrying coil. However, these coefficients can be recovered through a point matching scheme on an arbitrary spheroidal surface [18]. Note that independent sets of b_j must be recovered for each measurement position given the monostatic setup. The resulting set of 98 samples of $\vec{H}_z^{\mathrm{S}}$ can then be calculated through Equation 2.17. This process is repeated for each spheroid in Figure 2-3 to obtain 98 synthetic data points for the response

of the target.

Formation of Equivalent Spheroidal Coordinate System

The synthetic data points are then used to form linear equations governed by Equation 2.17. These 98 data points are overly sufficient to retrieve the aforementioned 28 B_k^j coefficients of interest for every calculated frequency.

However, Equation 2.17 describes activity within a single spheroidal coordinate system whereas $\vec{H}^{\mathrm{S}}$ is calculated from two independent coordinate systems, centered on and conforming to each separate spheroid. Therefore, to find the B_k^j describing the entire object, a new spheroidal coordinate system must be chosen to encompass both spheroids. This new spheroidal coordinate system is centered between the spheroids and has an interfocal distance of 0.2828 m which corresponds to a spheroid that is 30 cm along the major axis and 10 cm along the minor axis.

Within this new spheroidal coordinate system, 28 B_k^j coefficients are retrieved through Equation 2.17. These 28 coefficients can then be used to predict the response of the composite target for new observation positions. It should be noted that 28 B_k^j can be solved accurately in this manner. The appropriate sensitivity tests have been conducted to demonstrate the reliability of solving for even more than 28 modes [19]: that study showed that it is possible to retrieve even 63 reasonable B_k^j –reasonable in the sense that they create responses that deviate less than 25% from known "truth" responses–with 10% Gaussian noise added to the EMI signals used to invert for those B_k^j . For all studies described in this paper, no more than 28 B_k^j are ever used.

Also, it is helpful to understand that specific low order B_k coefficients actually correspond to each dipole moment as described earlier. While 28 B_k^j modes may sound like very many modes, for each 7 excitation j modes we are only solving for 4 k modes: the 3 modes which correspond to the dipole moments and one additional mode. Though the response modes are very low order, the improvement over the dipole model comes via the combination of higher order excitation modes with these response modes. This combination enables one to model any non-symmetry in a response. Also of note is that the modes corresponding to the dipole moments found through the spheroid mode framework are the true dipoles one would see at an infinite distance. As will be shown, the dipole moments found under the dipole model framework as described earlier can be shown to be highly distorted by the heterogeneity of object and the limited number of samples of $\vec{H}^S$.

Validation and Comparison

Verification of the accuracy of spheroidal model model can be shown by comparing its prediction to an independent model or measurements. Figure 2-4 (a) shows the superimposed spheroid model prediction for the response of the same horizontally orientated composite target as described in the previous section for a grid with 5.5 cm spacing on a measurement plane at an elevation of 0.55 m. Using the previously retrieved B_k^j , the spheroidal mode model calculates the expected response at 0.55 m and the result is shown in part (b). This figure demonstrates that 28 B_k^j can accurately characterize complex heterogeneous objects.

However, as mentioned previously, for many realistic objects and particularly for composite objects, the dipole model is not sufficient to describe the EMI response. To characterize

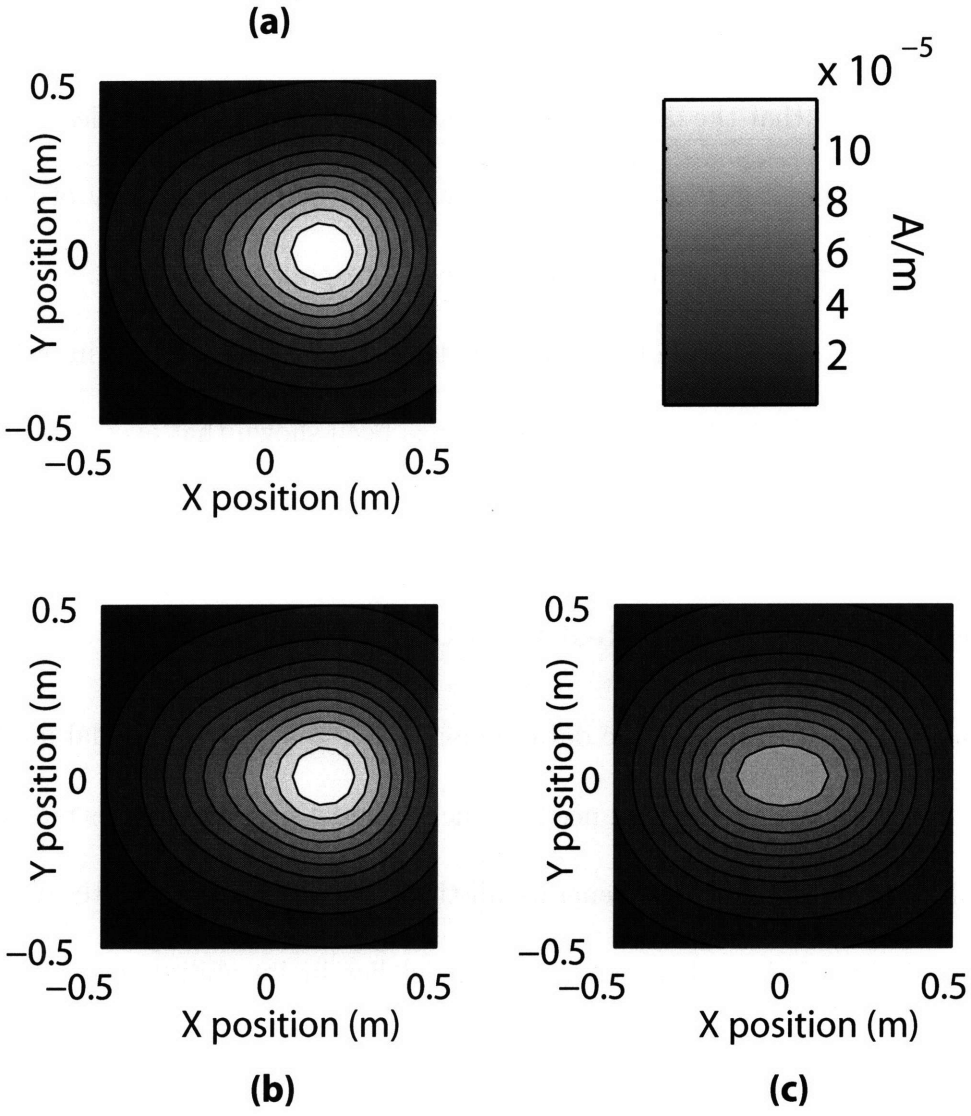

Figure 2-4: Comparison of the H_z response of a composite object using (a) direct calculation from forward model, (b) calculation from the retrieved B_k^j using only the 28 coefficients, (c) calculation from the retrieved dipole moments by assuming the object behaves like a dipole.

the extent of this insufficiency, it is enlightening to also use the same magnetic field data H^S on the 0.35 m and 0.45 m elevation planes to retrieve the diagonal elements of the magnetic polarizability matrix of this target. Then the dipole model is used to calculate the secondary field for the measurement plane at a distance of 0.55 m. In contrast to Figure 2-4 (b), one can easily see that the dipole model's response shown in (c) provides a much poorer characterization of the object and is unable to capture the non-symmetry of the response. In addition, the location of the predicted peak in the response is incorrect.

A previous study suggested not constraining the location of the dipole in order to better characterize responses [99]. However, it recently has been shown that even this more sophisticated dipole model does poorly for composite objects and suffers from non-uniqueness [77].

2.2.2.3 Formation of Model: Real UXO Object

The previous example with synthetic data demonstrates that the spheroidal mode model is valid but does not show any practical need for such a model since it becomes redundant given that the spheroid model is used to generate all the data. Therefore, a better demonstration of the applicability of the spheroidal mode model lies in its ability to predict responses of objects that cannot be directly modeled in such a manner, such as real UXO targets. Characterization by B_k^j coefficients first requires measurements of the target of interest. Measurements are taken using the GEM-3 broadband EMI frequency domain instrument [93]. As noted briefly earlier, the transmitter and receiver are current loops which are concentrically located on the same plane within the instrument head. Therefore, the GEM-3 operates in a monostatic manner. Furthermore, the GEM-3 records magnetic fields, not the

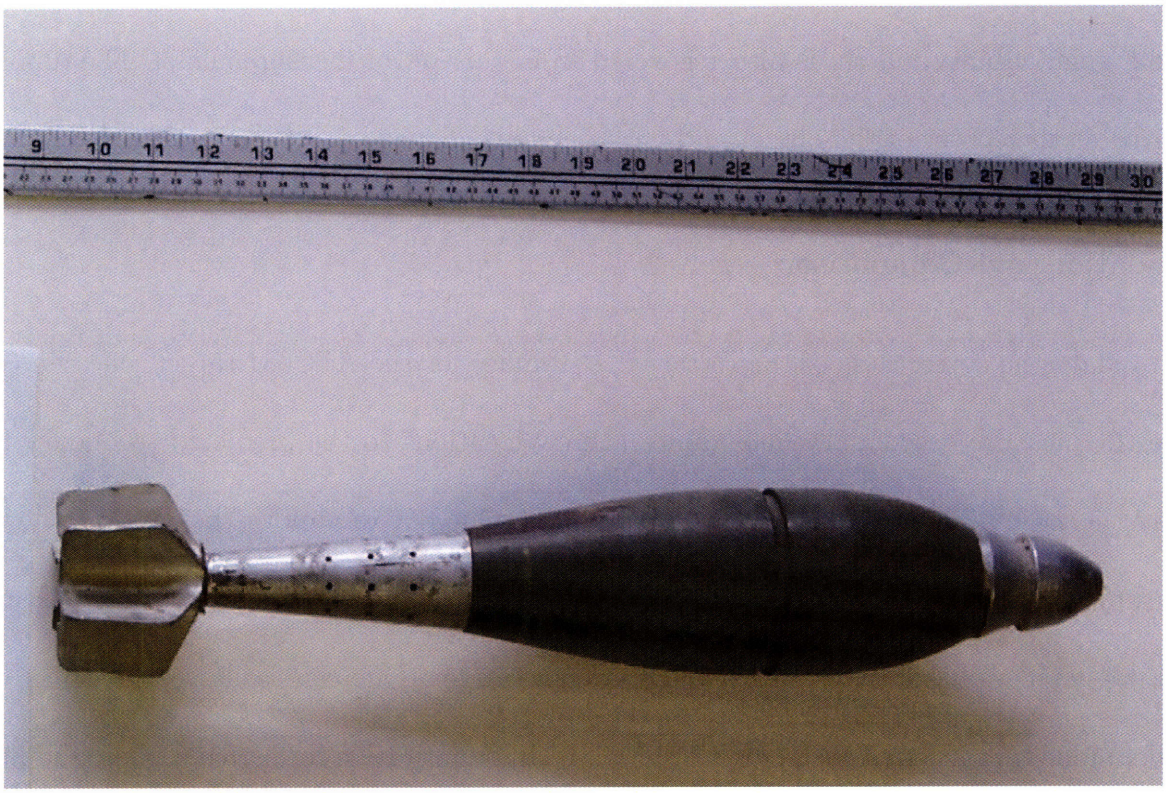

Figure 2-5: UXO ATC081 with a ruler. Measurements of this object are used to validate the spheroidal mode model. Photograph courtesy of CRREL.

time derivative of the magnetic fields as one would expect. A more detailed discussion on the GEM-3 and instrument modeling is given in Section 2.4.

The ATC081 UXO object is selected as the measurement target. As shown by Figure 2-5, it is roughly 51 cm long from nose (right) to tail (left).

ATC081 is tilted so that the nose is 45 degrees from vertical and pointing towards the third quadrant, ie, a ϕ rotation angle of $3\pi/4$. The measurements are on a plane located 26.7 cm above the nose of the target and again are aligned on a 7 by 7 grid with 10 cm spacings. 10 measurements were taken at each point on the grid and then averaged to form a set of 49 measurements over a range of frequencies from 30Hz to 47970Hz. These measurements

are then used to recover the 28 lowest B_k^j values of the target. To serve as comparison, the dipole polarizability matrix is also recovered from this set of measurements. The dipole is located at the center of the object and with one axis aligned with the axis of the UXO.

Validation and Comparison

To validate the correctness of the retrieved B_k^j values for the ATC081 target, one can compare the measured secondary field values at new locations to the predicted secondary field using the B_k^j . The new measurements were taken at 31.7 cm above the target, following the same grid pattern as before. Shown in Figure 2-6 is the comparison between measured and predicted values for this new plane above the target. One can easily see the spheroidal model model produces a much closer prediction. In quantitative terms. the spheroidal mode model produces an error of 0.15 across all frequencies. The dipole model produces an error of 0.33. Error calculation is discussed thoroughly in Section 3.4, but these values can be interpreted as 15% and 33% error difference for the spheroidal mode model and dipole model, respectively.

2.2.3 Time Domain Differential Step Response of a Sphere

The previous models provide frequency domain predictions. Recently, numerical methods were implemented to model the time domain response of spheroids and body of revolution shapes [53–55]. For the canonical sphere, Wait resolved the time domain step response for a permeable and non-permeable conducting spheres [89]. For a non-permeable sphere of radius a and conductivity σ in a uniform magnetic field of $H_o e^{i\omega t}$, the step input time response in

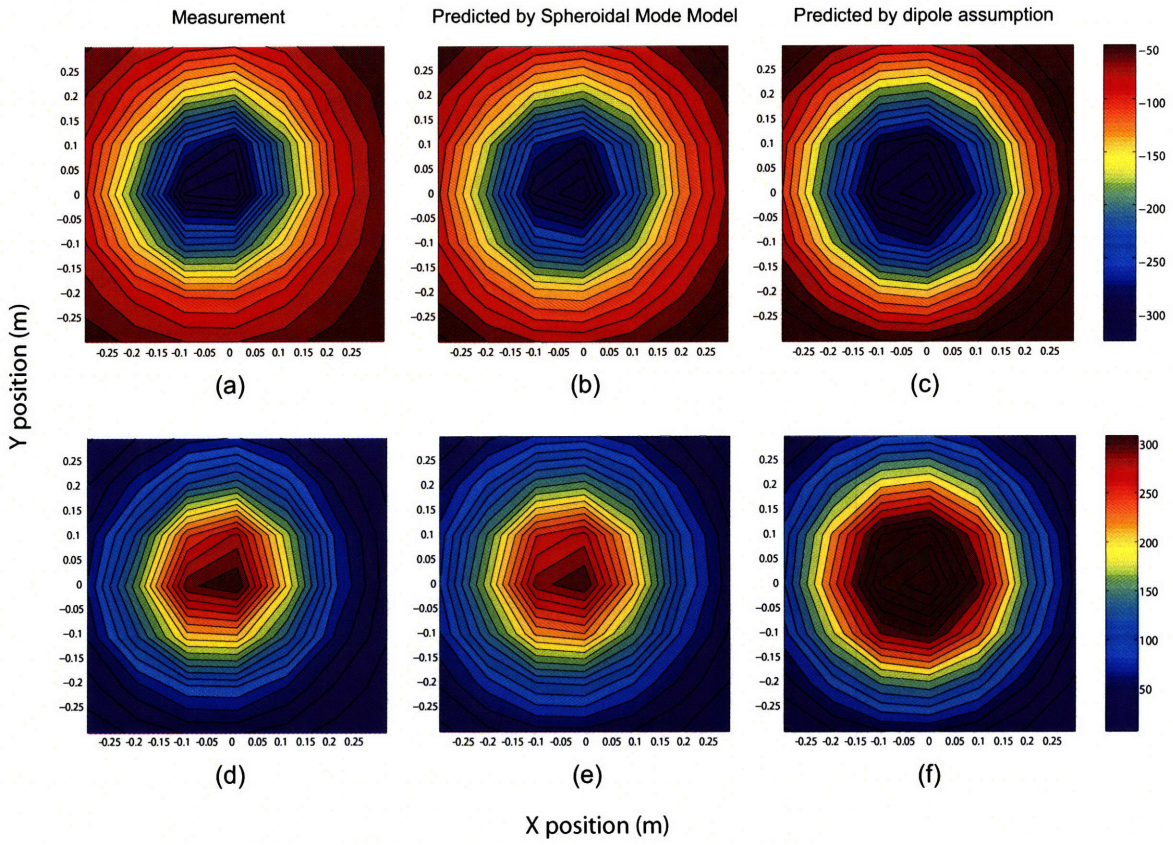

Figure 2-6: Comparison between measured response of ATC081 and the responses predicted by the spheroidal mode model and the dipole model. The first row (a)-(c) shows the Inphase response at 210 Hz. The second row (d)-(e) shows the Quadrature response at 10950 Hz. Measurement data courtesy of CRREL.

polar coordinates is,

$$\vec{H}(r,\theta,t) = -\nabla \frac{a^3 H_o}{2r^{-2}} \cos(\theta) h(t) \tag{2.18}$$

$$h(t) = 3\left[T + \frac{1}{3} - 2\left(\frac{T}{\pi}\right)^{1/2} - 2\sum_{m=1}^{\infty}\left\{T^{1/2}\mathrm{erf}'\left(\frac{m}{T^{1/2}}\right) - 2m\cdot\mathrm{erfc}\left(\frac{m}{T^{1/2}}\right)\right\}\right] u(T), \tag{2.19}$$

where

$$T = \frac{t}{\sigma\mu_o a^2} \tag{2.20}$$

and where erf and erfc are the error function and complementary error function given by

$$\mathrm{erf}(z) = \frac{2}{\sqrt{\pi}}\int_0^z e^{-t^2} dt = 1 - \mathrm{erfc}(z). \tag{2.21}$$

However, most time domain instruments record the time derivative of the step down response. This response can be derived from Wait's expression

$$\vec{H}_{\mathrm{new}}(r,\theta,t) = +\nabla \frac{a^3 H_o}{2r^{-2}} \cos(\theta) \frac{\partial h(t)}{\partial t} \tag{2.22}$$

$$\begin{aligned}\frac{\partial h(t)}{\partial t} &= \frac{3}{\sigma\mu_o a^2}\left[1 - \frac{1}{\sqrt{T\pi}} - 2\sum_{m=1}^{\infty}\left\{\frac{1}{2T^{\frac{1}{2}}}\mathrm{erf}'(\frac{m}{T^{\frac{1}{2}}}) + \frac{2m^2}{\sqrt{\pi}T^2}e^{-\frac{m^2}{T}} - \frac{m^2}{T^{\frac{3}{2}}}\mathrm{erf}'\left(\frac{m}{T^{\frac{1}{2}}}\right)\right\}\right] u(T) + \\ &+3\left[T + \frac{1}{3} - 2\left(\frac{T}{\pi}\right)^{\frac{1}{2}} - 2\sum_{m=1}^{\infty}\left\{T^{\frac{1}{2}}\mathrm{erf}'\left(\frac{m}{T^{\frac{1}{2}}}\right) - 2m\cdot\mathrm{erfc}\left(\frac{m}{T^{\frac{1}{2}}}\right)\right\}\right]\frac{\delta(t)}{\sigma\mu_o a^2}\end{aligned} \tag{2.23}$$

For a permeable sphere of radius a, σ, and permeability μ_1, the analogous expression to Equation 2.19 was given by Wait and others [86] as,

$$h(t) = \left[6K \sum_{n=1,2,3\cdots}^{\infty} \frac{e^{-\delta_n^2 T}}{(K+2)(K-1)+\delta_n^2} - \frac{2(K-1)}{K+2}\right] u(T), \tag{2.24}$$

where

$$T = \frac{t}{\sigma \mu_1 a^2}. \tag{2.25}$$

$$K = \mu_1/\mu_0, \tag{2.26}$$

and where δ_n are the solutions of

$$\tan \delta_n = \frac{(K-1)\delta_n}{K-1+\delta_n}. \tag{2.27}$$

The derivative of the step down response can be found using Equation 2.22 and substituting the following expression for Equation 2.23:

$$\begin{aligned} \frac{\partial h(t)}{\partial t} &= \left[6K \sum_{n=1,2,3\cdots}^{\infty} \frac{\frac{-\delta_n^2}{\sigma\mu_1 a^2} exp[-\delta_n^2 T]}{(K+2)(K-1)+\delta_n^2}\right] u(T) + \\ &+ \left[6K \sum_{n=1,2,3\cdots}^{\infty} \frac{exp[-\delta_n^2 T]}{(K+2)(K-1)+\delta_n^2} - \frac{2(K-1)}{K+2}\right] \frac{\delta(T)}{\sigma\mu_1 a^2}, \end{aligned} \tag{2.28}$$

where $\delta(T)$ is the Dirac delta function, not to be confused with δ_n.

The solution of the permeable conducting sphere requires solving for δ_n which can be

accomplished by moving the left hand expression of Equation 2.27 to the right and finding the zeros of the equation,

$$0 = \frac{(K-1)\delta_n}{K-1+\delta_n} - \tan\delta_n. \tag{2.29}$$

These zeros are then found numerically by expanding and checking the limits of a small interval near an initial guess until a change in sign is found. The interval is then searched for the zero crossing. All zeros within a finite range can be found by utilizing a densely spaced collection of initial guesses and then removing any redundant recovered zero values. Figure 2-7 shows Equation 2.29 with the first twelve zeros successfully recovered through this algorithm.

2.2.3.1 Validation

The time domain solution can be validated by the comparison to measurements of small metal spheres. Measurements were taken of an aluminum sphere with a diameter of 3 inches. The measurements and the corresponding modeled response are shown in Figure 2-8. Given that the man portable vector (MPV) time domain EMI instrument has a transmitter coil with a radius of 37.5 cm and that the measurements were at a distance of 36 cm [33], a uniform field at the vicinity of the sphere is a good approximation. The delta component of the modeled response is not calculated in the solution.

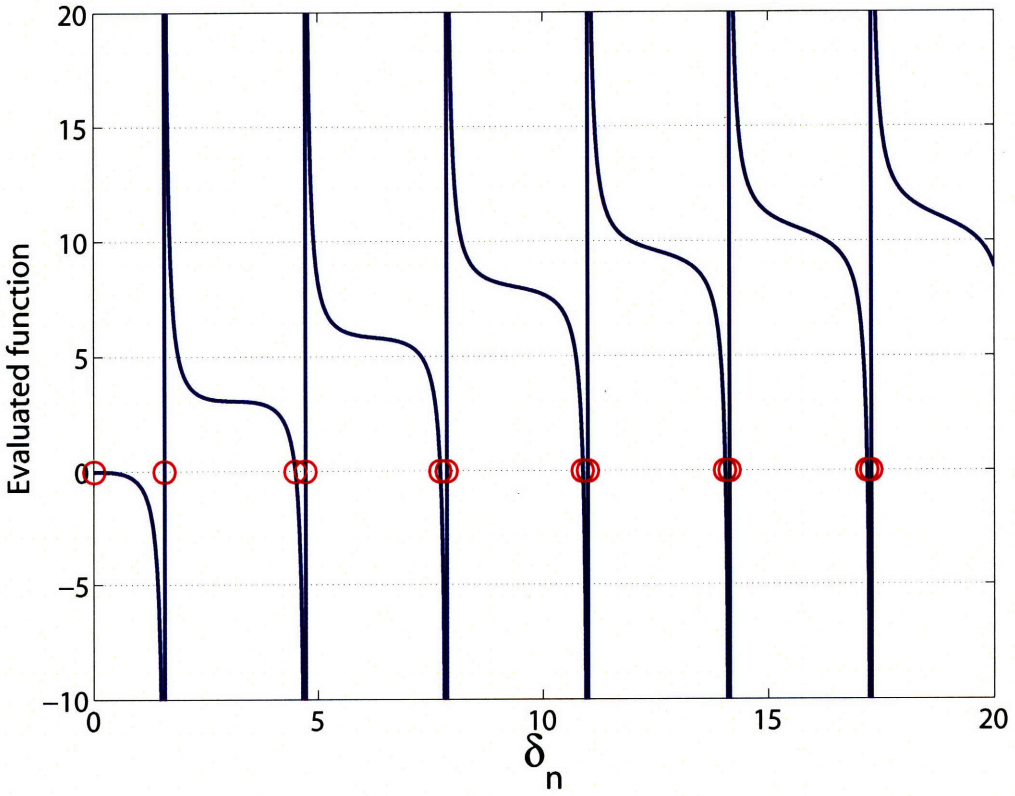

Figure 2-7: Equation 2.29 plotted as a function of δ_n. Recovered zeros are circled.

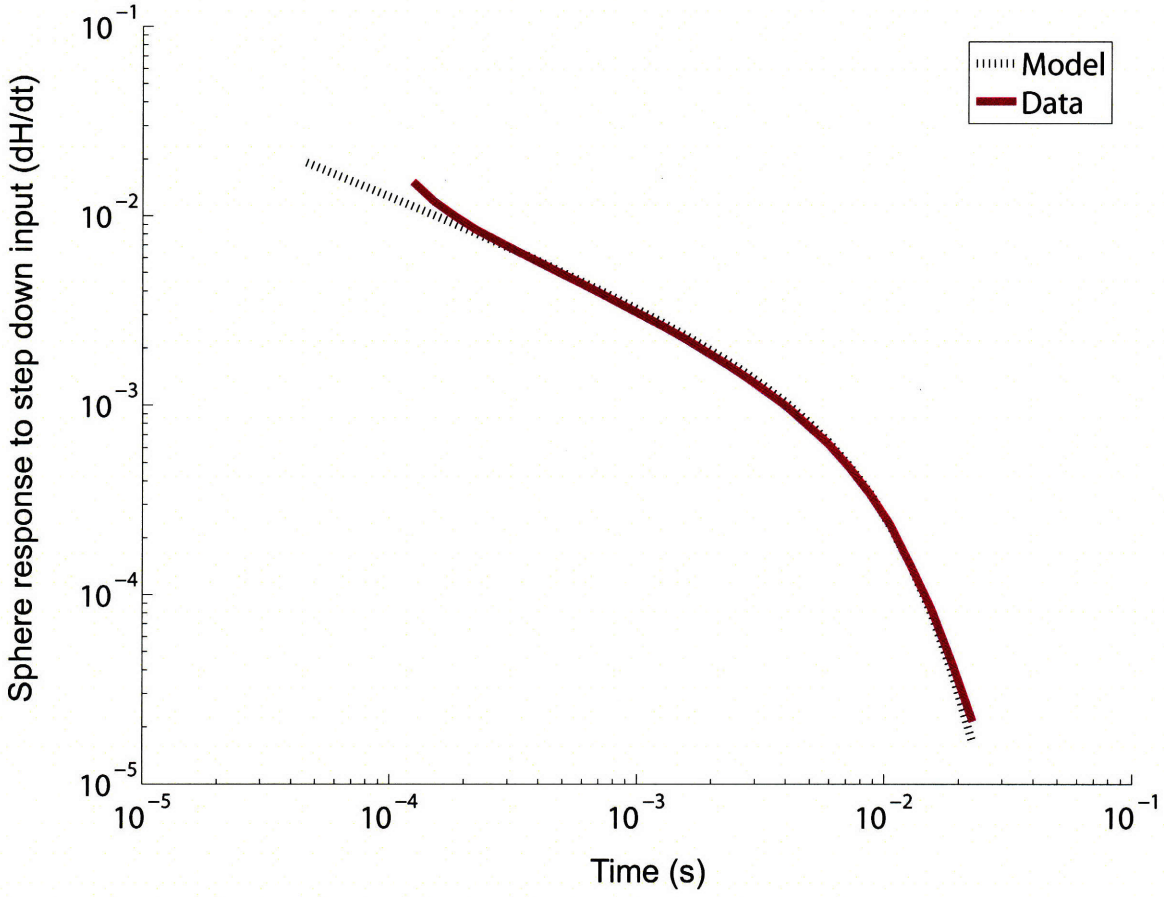

Figure 2-8: Comparison between modeled time derivative of an aluminum sphere's response and measured response. Measurement data courtesy of CRREL.

2.3 Soil and Halfspace Modeling

Soil is considered completely transparent to EMI devices that detect UXO only to the extent that a weakly conducting, weakly permeable homogeneous background medium, typical of most soils can be considered equivalent to free space under quasistatic conditions.

However, due to the discontinuity in μ created by an even slightly permeable ground, the soil halfspace can contribute significantly to the secondary fields measured above ground. Furthermore, this planar interface of the surface of the soil may interact with the response of the buried object. Thus in realizing any complete forward model of a buried UXO, one must account for all possible effects of soil.

Past work in halfspace modeling is first discussed. Then a new approximation for the response of a target embedded in a permeable halfspace is introduced and compared with measurements. Comparison with the response of the same object in freespace shows that the discontinuity of the background medium for the range of realistic soil permeabilities has very limited effect on the EMI response of a buried metal target. Finally, it is shown that soil permeability values can be recovered from EMI measurements of soil by matching modeled permeable halfspace responses with measurements.

2.3.1 Previous Work

There has been very limited previous work in the EMI regime in regards to the possible interaction between the soil-to-air interface and a buried object. While models for a discontinuous background medium with embedded targets for higher frequency regimes have

been suggested [57], the models for the frequency range of interest have largely been for conducting backgrounds and non-permeable targets [51]. The most extensive study of any type for target and halfspace interaction in the EMI regime was conducted by Das [28] who proposed an approximation for a non-permeable conducting sphere buried in non-permeable conductive ground where the response of the sphere can be replaced with two independent but co-located dipoles.

To date, previous treatments of permeable targets in permeable soils largely do not address any possible coupling effects [45]. Models for buried targets are simply the superposition of the targets response in free space with the soil's halfspace response. However, the validity of such models has never been studied. The research described in this chapter addresses this oversight by creating a model for a buried object which accounts for the interaction between the target and a discontinuity in the background medium which represents the soil to air interface.

2.3.2 Research Overview

The research into soil effects on a buried target has three main components, each addressed by a question the researcher must ask:

1. How can one model a permeable half-space's response to an EMI instrument?

2. How does an object embedded in a permeable halfspace respond to an EMI instrument? How does this response differ from the response of the object in free space?

3. Given these models of soil, can useful information about soil properties be obtained from measured soil EMI responses?

2.3.3 Modeling of Soil Response

2.3.3.1 Response of a Homogeneous Half Space

The simplest model for soil assumes it is a non-conducting, homogeneous halfspace of permeable material. As argued in Section 1.4.3, conduction current in the soil is insignificant when compared to the current in the metal targets. Therefore this model is valid.

Wait [88] obtained the solution for the magnetic potentials in the upper and lower regions of a half-space when illuminated by a magnetic dipole in the upper half-space as shown in Figure 2-9. In the upper half-space,

$$\Phi = \Phi^{\mathrm{p}} + \Phi^{\mathrm{s}} \tag{2.30}$$

where Φ^p is the "primary" potential created by the dipole and Φ^s is created by the interaction between the dipole and the boundary of the half-space. The primary potential of a vertical dipole with a moment of m_{zo} located h above the ground plane is,

$$\Phi^{\mathrm{p}} = \frac{m_{zo}(z-h)}{4\pi r_1^3} \tag{2.31}$$

where r_1 is the distance from the observation point to the dipole. Without loss of generality, the origin is chosen to be on the surface of the halfspace, directly beneath the dipole. The

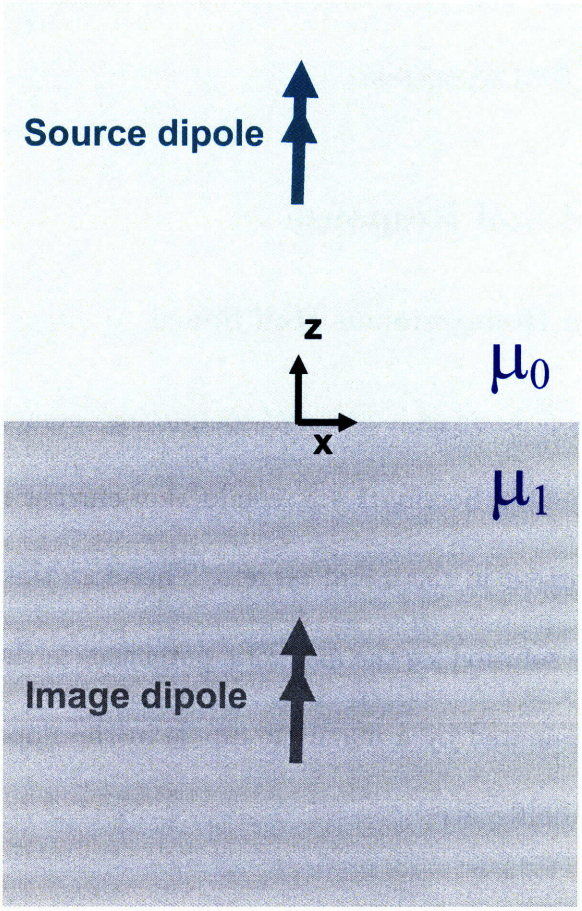

Figure 2-9: Schematic for the calculation of a halfspace response to a dipole excitation.

positive z axis points upwards toward the dipole.

The secondary potential in the upper half space can be calculated through image theory. The region of interest is the upper half space. There is an image dipole situated in the lower half-space. Wait found through matching boundary conditions that an extra coefficient is needed to describe the image dipole. Therefore, the position of the image dipole mirrors the real dipole but their magnitudes, which may be of opposite sign, differ from each other. For example, a vertical transmitting dipole over a halfspace creates a the secondary potential

seen in the upper half space as,

$$\Phi^{\mathrm{s}} = K_{01}\frac{m_{zo}(z+h)}{4\pi r_2^3} \tag{2.32}$$

where

$$K_{01} = \frac{\mu_1 - \mu_0}{\mu_1 + \mu_0} \tag{2.33}$$

and where r_2 is the distance to the image dipole from the observation point. K_{01} is the relative strength factor of the image. This factor can also be thought of as a "reflection" coefficient as the fields attempt to traverse from region "0" to region "1" as denoted by the subscript order.

By matching boundary conditions again, Wait found that Φ^p in the lower half space is attenuated by a factor T_{01}. This attenuation factor may be also thought of as a transmission coefficient as the fields crosses from region "0" into region "1." The potential in the lower half space created by a vertical transmitting dipole in the upper halfspace is then,

$$\Phi^{\mathrm{l}} = T_{01}\frac{m_{zo}(z-h)}{4\pi r_1^3} \tag{2.34}$$

where

$$T_{01} = \frac{2\mu_0}{\mu_1 + \mu_0}. \tag{2.35}$$

$\vec{H}^{\mathrm{l}}$, the magnetic field in the lower halfspace is then easily derived from Equation 2.34.

For simplicity, it may be expressed in the cylindrical coordinate system where ρ and $\hat{\rho}$ refers to the radial distance and direction from the transmitting dipole to the observation location:

$$\vec{H}^{1} = T_{01}\frac{m_{zo}}{4\pi}\left[\frac{3(z-h)\rho}{(\rho^2+(z-h)^2)^{5/2}}\hat{\rho} + \frac{2(z-h)^2-\rho^2}{(\rho^2+(z-h)^2)^{5/2}}\hat{z}\right]. \tag{2.36}$$

Horizontal transmitting dipoles can be analyzed in a similar fashion. Suppose a magnetic dipole of strength m_{xo} is oriented in the $\hat{x}$ direction. The secondary potential in the upper halfspace would be

$$\Phi^{S} = K_{01}\frac{m_{xo}x}{4\pi r_2^3}. \tag{2.37}$$

The potential in the lower halfspace would be

$$\Phi^{1} = T_{01}\frac{m_{xo}x}{4\pi r_1^3}. \tag{2.38}$$

Since time domain EMI instruments always measure transients following a step down excitation, a non-conducting permeable halfspace should produce no measurable activity. The response of the halfspace should always be instantaneous with no relaxation activity [20]. While this is a good approximation of the FD soil responses considered in this study, TD instruments may show some soil relaxation response that is obscured in the FD data [33]. Such transient responses can be represented by the same solution obtained above, at each point in time, scaled by a factor that depends on soil relaxation times. These must be obtained on a case by case basis.

2.3.4 Approximation of the Response of a Sphere Buried in Soil

While a complete model of a metal target embedded in a permeable halfspace is always possible with numerical models such as finite-difference time-domain, or analytical methods as proposed by [30], such accuracy may not be necessary given that soils are typically only weakly magnetic with $\mu_r \ll 1.01$. A more parsimonious use of resources is to first obtain an estimate of the extent to which the soil interface does or does not affect the response of buried objects before determining whether more precise modeling is necessary.

The approximation described in the following sections is a variant of the Foldy-Lax technique which has been used to solve both scattering problems [21] and EMI problems [13].

2.3.4.1 Formulation

Suppose there is sphere of radius a and conductivity σ_2 and permeability μ_2 buried a distance d below a halfspace. The center of the coordinate system is taken to be on the surface of the halfspace directly above the sphere. The excitation source is at some elevation h and radial distance r. One can approximate the response of a halfspace with an embedded sphere as having two main components: the one directly due to a halfspace in absence of the sphere, and one due to the sphere itself which includes the interactions it has with the halfspace interface. Calculation for the first component was shown in the previous section. Calculation of the second component is the focus of the current section.

One simplification utilized in this study is the assumption that all excitation may be considered locally uniform within the vicinity of the sphere. Since a sphere only produces a

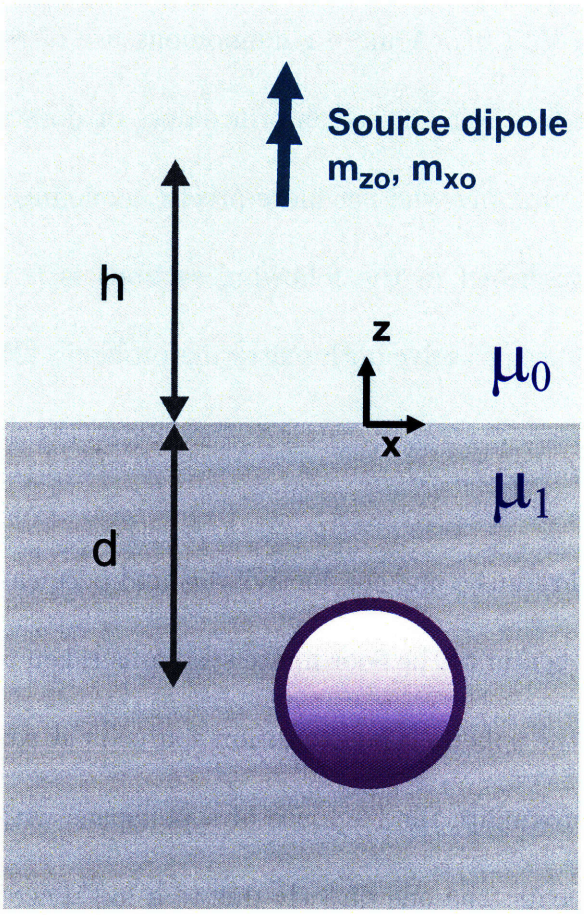

Figure 2-10: Schematic for the calculation of the response for sphere embedded in a halfspace to a dipole excitation.

dipole response under uniform excitation, its response can be characterized as dipole. The induced dipole moment of the sphere, $\vec{m}_{sphere}$, depends on the magnetic polarizability tensor $\overline{\overline{M}}$ and the incident magnetic field.

$$\vec{m}_{\text{sphere}} = \overline{\overline{M}}_{\text{sphere}} \cdot \vec{H}^{\text{i}} \tag{2.39}$$

The magnetic polarizability tensor for a sphere in free space with radius a, permeability μ_2, and conductivity σ_2 is

$$\overline{\overline{M}}_{\text{sphere}} = \beta \cdot \overline{\overline{I}} \tag{2.40}$$

where β is

$$\beta = 2\pi a^3 \frac{(2\mu_2 + \mu_1)(1 - k_2 a \cot k_2 a) - \mu_1 (k_2 a)^2}{(\mu_2 - \mu_1)(1 - k_2 a \cot k_2 a) + \mu_1 (k_2 a)^2} \tag{2.41}$$

and

$$k_2 = \sqrt{i\omega\mu_2\sigma_2} \tag{2.42}$$

as derived by Wait [87] and many others [7, 46].

The dipole response of the sphere, as characterized by its moment $\vec{m}_{\text{sphere}} =< m_z, m_\rho >$, can be computed from the known polarizability matrix and incident magnetic field on the target. Note that the cylindrical coordinate system can be rotated so that ϕ is not a factor

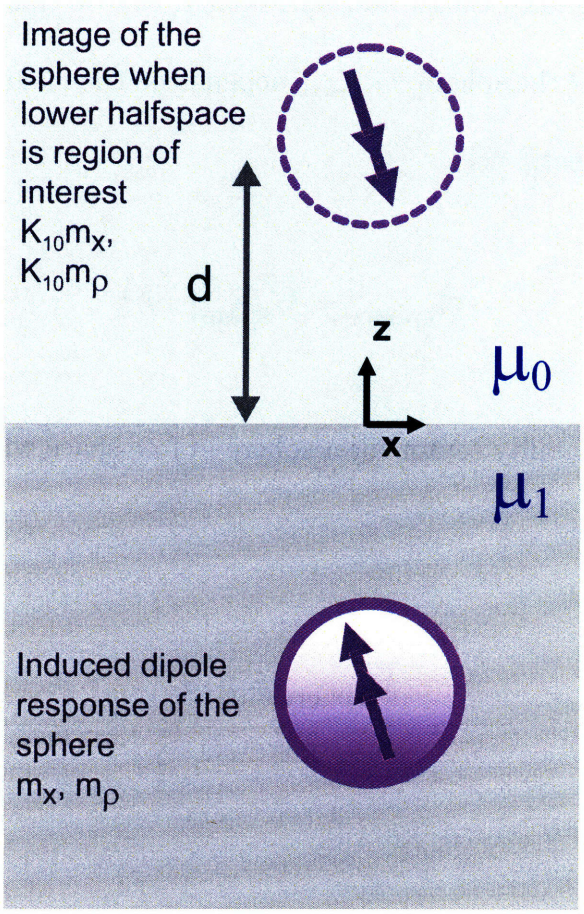

Figure 2-11: Sphere and the image of the sphere when the lower halfspace is the region of interest.

in the calculation.

In Equation 2.39, the total incident magnetic field on the sphere is not simply from the transmitter as calculated by Equation 2.34. Rather, the sphere also sees an image of itself due to the halfspace discontinuity. Consider the lower halfspace the region of interest; the image is located in the upper halfspace. Since the sphere is assumed to only produce a dipole response, then this image must also be a dipole as shown in Figure 2-11.

Therefore, the total incident magnetic field on the sphere has two components: $\vec{H}^1$ directly

from the transmitter and attenuated by T_{01} as discussed previously and $\vec{H}^{\text{si}}$ due to the image of the sphere. Equation 2.43 gives this relationship.

$$\vec{m}_{\text{sphere}} = \overline{\overline{M}}_{\text{sphere}} \cdot [\vec{H}^{\text{i}} + \vec{H}^{\text{si}}] \tag{2.43}$$

The greatest difficulty in Equation 2.43 is that $\vec{H}^{\text{si}}$ is unknown because $\vec{m}_{\text{sphere}}$ is unknown. However, since the sphere and the image of the sphere are both dipoles, the equation describing the field produced by the image of the sphere where the lower halfspace is the region of interest is perfectly analogous to Equation 2.32. The pertinent coefficient is now $K_{10} = \frac{\mu_0 - \mu_1}{\mu_0 + \mu_1}$. The expression for $\vec{H}^{\text{si}}$ contains $\vec{m}_{\text{sphere}}$. However, for the sake of clarity, one can first write the contribution to $\vec{H}^{\text{si}}$ due to the m_z component of $\vec{m}_{\text{sphere}}$:

$$\vec{H}^{\text{si}}_{m_z} = K_{10}\frac{3m_z(z-d)\rho}{4\pi(\rho^2+(z-d)^2)^{5/2}}\hat{\rho} + K_{10}\frac{2m_z(z-d)^2-\rho^2}{4\pi(\rho^2+(z-d)^2)^{5/2}}\hat{z} \tag{2.44}$$

where z and ρ is the observation position in the lower halfspace.

$$K_{10} = \frac{\mu_0 - \mu_1}{\mu_0 + \mu_1} \tag{2.45}$$

Since the image of the sphere is directly above the sphere and thus directly above the origin, $\rho = 0$ and the equation is greatly simplified and produces the $\hat{z}$ component of $\vec{H}^{\text{si}}$ as shown in Equation 2.46:

$$\vec{H}^{\text{si}}_{z} = \frac{K_{10}m_z}{16\pi d^3}. \tag{2.46}$$

Likewise, upon examining the contribution to $\vec{H}^{\text{si}}$ due to the m_ρ component of $\vec{m}_{\text{sphere}}$, one can find the $\hat{\rho}$ component of $\vec{H}^{\text{si}}$

$$\vec{H}_\rho^{\text{si}} = \frac{K_{10} m_\rho}{32\pi d^3}. \tag{2.47}$$

Equations 2.46 and 2.47 can be substituted into Equation 2.43. Gathering and factoring out the terms with $\vec{m}_{\text{sphere}}$ components meets the objective of solving for $\vec{m}_{\text{sphere}}$:

$$m_\rho = \frac{\beta H_\rho^{\text{l}}}{1 - \beta \frac{K_{10}}{32\pi d^3}} \tag{2.48}$$

$$m_z = \frac{\beta H_z^{\text{l}}}{1 - \beta \frac{K_{10}}{16\pi d^3}} \tag{2.49}$$

where H_z^{l} and H_ρ^{l} refer to the $\hat{z}$ and $\hat{\rho}$ components of the magnetic field in the lower halfspace, $\vec{H}^{\text{l}}$, created by the transmitting dipole as given in Section 2.3.3.1. Note that since the cylindrical coordinate system was originally chosen so that the $\hat{\phi}$ component of $\vec{m}_{sphere}$ is irrelevant, H_ϕ^{l} does not enter into the calculation either. Using Equations 2.48 and 2.49, the dipole moment of a buried sphere can be found for any specified $\vec{H}^{\text{l}}$ at the location of the sphere.

As an illustrative example, a vertical transmitting dipole of moment m_{zo} is considered. Section 2.3.3.1 provided the corresponding expression for $\vec{H}^{\text{l}}$. Both H_z^{l} and H_ρ^{l} created by this dipole can be calculated at the location of the sphere. Therefore, the dipole moments of the sphere are

$$m_\rho = \frac{\beta T_{01} \frac{m_{zo} 3(-d-h)r}{4\pi(r^2+(-d-h)^2)^{5/2}}}{1-\beta\frac{K_{10}}{32\pi d^3}} \tag{2.50}$$

$$m_z = \frac{\beta T_{01} \frac{m_{zo}(2(-d-h)^2-r^2)}{4\pi(r^2+(-d-h)^2)^{5/2}}}{1-\beta\frac{K_{10}}{16\pi d^3}}. \tag{2.51}$$

The most interesting components in the above equations are T_{01} factor in the numerator and the βK_{10} term in the denominator. If $\mu_1 = \mu_0$, these equations reduce to the dipole response of a sphere in free space for the specified excitation. However, due to the difference in permeability between the upper and lower halfspaces, the dipole response of the sphere is altered. The extent of this alteration will be analyzed in Section 2.3.5. Note that some care must be taken in the construction of Equations 2.50 and 2.51 since the original Equation 2.36 for $\vec{H}^l$ is written with the origin located below the transmitting dipole while these equations are written with the origin located above the sphere.

A similar treatment for an excitation by a horizontal transmitting dipole m_{xo} aligned in the $+\hat{x}$ direction can also be carried out:

$$m_\rho = \frac{-\beta T_{01} \frac{m_{xo}}{4\pi}\left(\frac{\cos\phi}{(\rho^2+(z-h)^2)^{3/2}} - \frac{3\rho^2}{(\rho^2+(z-h)^2)^{5/2}}\right)}{1-\beta\frac{K_{10}}{32\pi d^3}} \tag{2.52}$$

$$m_\phi = \frac{-\beta T_{01} \frac{m_{xo}\sin\phi}{4\pi(\rho^2+(z-h)^2)^{3/2}}}{1-\beta\frac{K_{10}}{32\pi d^3}} \tag{2.53}$$

$$m_z = \frac{\beta T_{01} \frac{m_{zo}(3\rho\cos\phi(z-h))}{4\pi(\rho^2+(z-h)^2)^{5/2}}}{1-\beta\frac{K_{10}}{16\pi d^3}}. \tag{2.54}$$

2.3.5 Analysis of the Half Space Interaction Model

The aforementioned model for the response of a sphere embedded in a half space is implemented in Matlab. Using this model one can determine if the presence of the halfspace interface significantly alters the response of the sphere. This goal can be achieved through the comparison of the response of a sphere with the $\vec{m}_{sphere}$ as in described the previous equations and the predicted response of the same sphere in free space. The results for various values of soil μ_1 are examined.

Figure 2-12 shows the comparison for a 2.5 cm radius steel-like sphere of $\sigma_2 = 4 \times 10^6$ S/m and $\mu_2 = 150\mu_0$. The two sets of curves show the modeled response of the sphere in free space versus one embedded in a halfspace of relative permeability 1.01 at a depth of 15 cm. The dipole transmitter is 15 cm above the halfspace. At this point, the curves are indistinguishable. The difference, when regarded as noise, is equivalent to more than 40dB SNR. If μ_r of the soil is increased to 1.1, the two sets of curves become distinct as seen in Figure 2-13. However, we are not aware of any naturally occurring soil that has such a high relative permeability. For example, some of the most magnetic soils in the world are in Hawaii due to the high concentration of volcanic ash. However, even there the relative permeability is well below 1.01 [61, 74, 84].

Given the very small impact of the halfspace interface on the sphere's response for the

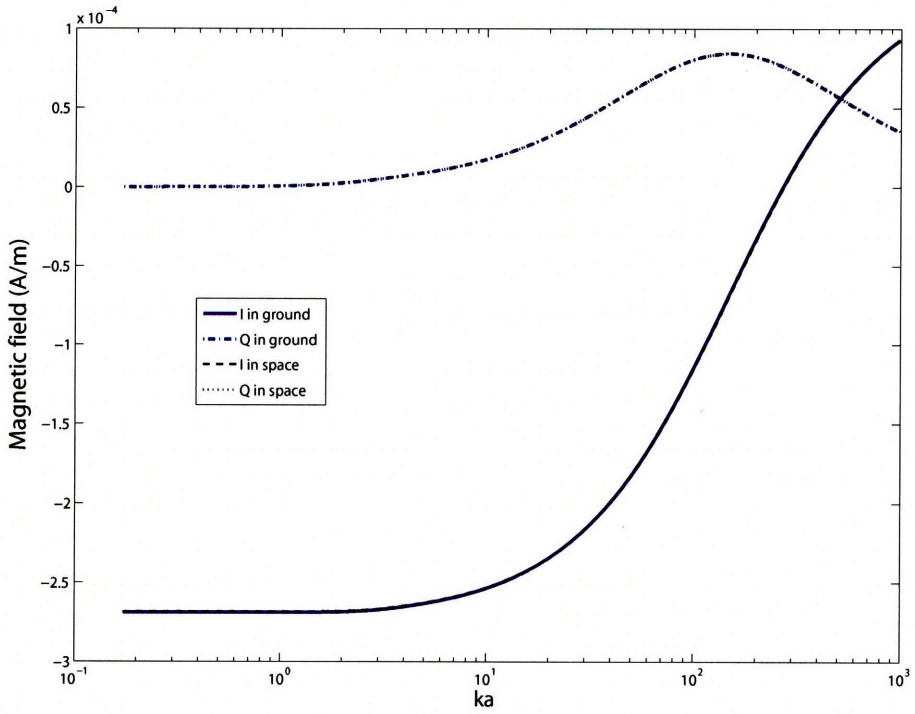

Figure 2-12: Modeled response of 2.5 cm radius sphere with $\mu_r = 150$, $\sigma_2 = 4 \times 10^6$ S/m, and buried 15 cm below a $\mu_r = 1.01$ halfspace. Excitation source is 15 cm above halfspace. Response is calculated at the same location as the transmitter. The blue curves do not contain the direct halfspace response of the soil, created by the image of the transmitting dipole. Therefore, the blue curves can be compared to the response of the same object in freespace, represented by the black curves. For this halfspace permeability value, the two sets of curves are indistinguishable. For a higher permeability value as shown in Figure 2-13, the curves are more distinct. However, no naturally occurring soil has a relative permeability greater than 1.01. Therefore the response of a buried object can be accurately modeled by superimposing the direct halfspace response of the soil onto the response of the target in freespace.

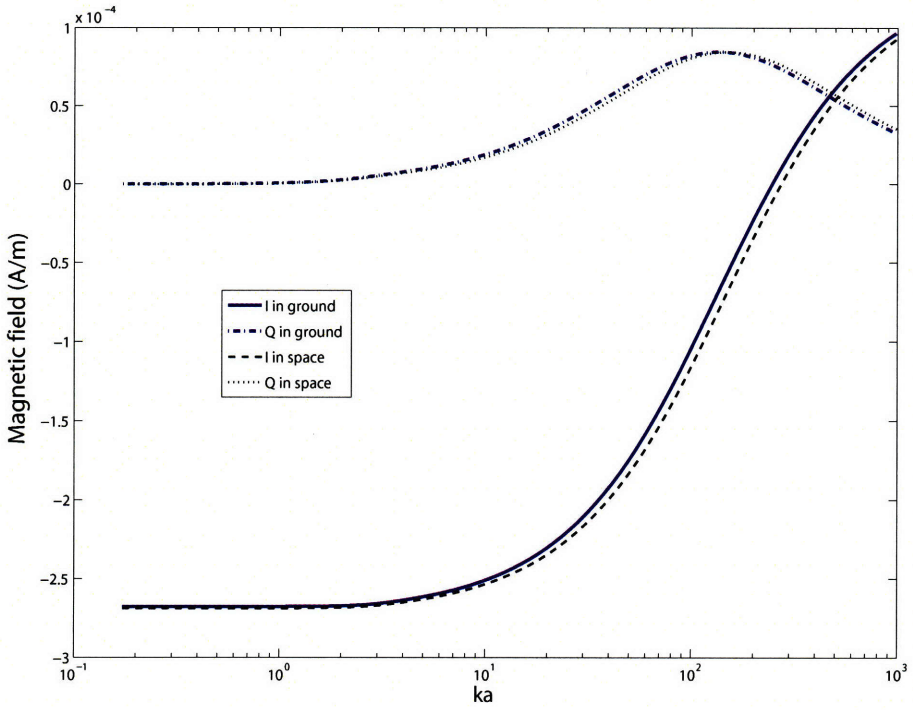

Figure 2-13: Modeled response of 2.5 cm radius sphere with $\mu_r = 150$, $\sigma_2 = 4 \times 10^6$ S/m, and buried 15 cm below a $\mu_r = 1.1$ halfspace. Excitation is 15 cm above halfspace. Response is calculated at the same location as transmitter. The blue curves do not contain the direct halfspace response of the soil, created by the image of the transmitting dipole. Therefore, the blue curves can be compared to the response of the same object in freespace, represented by the black curves. For this halfspace permeability value, the two sets of curves are distinguishable. However, no natural soil has permeability above 1.01 so the modeled scenario of this figure is unrealistic.

range of realistic soil permeability values, one can confirm the original assumption of the soil being effectively transparent to EMI instruments and insignificance of any sphere to halfspace interaction. However, the previous analysis do not included the direct response of the halfspace interface. The expression for $\vec{m}_{\text{sphere}}$ only encompasses the response of the sphere and not the entire $\vec{H}^{\text{S}}$ stemming from Φ^{S} of Equation 2.32 as noted earlier.

In this simple, non-conducting soil, Equation 2.32 has no frequency dependent component. Therefore, the direct response should be Inphase and constant over frequency. The overall effect on the received signal will be reduced to a magnitude shift of the Inphase response. Though the permeability of soil is low, this offset may be significant when compared to responses of objects buried in typical soil as will be shown in the following sections.

2.3.6 Comparison to Measured Response of Buried Spheres

The conclusions of the modeling study described in the previous sections can be validated by comparing measurements of buried objects to measurements of those same objects in free space. Shown in Figure 2-14 are measurements of a steel sphere buried in ground and in free space. These measurements were conducting by CRREL using typical "backyard" soil not known to be particularly magnetic. The difference between the response of the sphere in free space and in soil is limited to a constant, frequency independent magnitude shift of the Inphase signal, confirming the earlier hypothesis. This observation is more clearly shown in Figure 2-15 where the Inphase portion of the buried sphere's response can be shifted back to provide an excellent match to the response of the sphere in free space. Differences at the

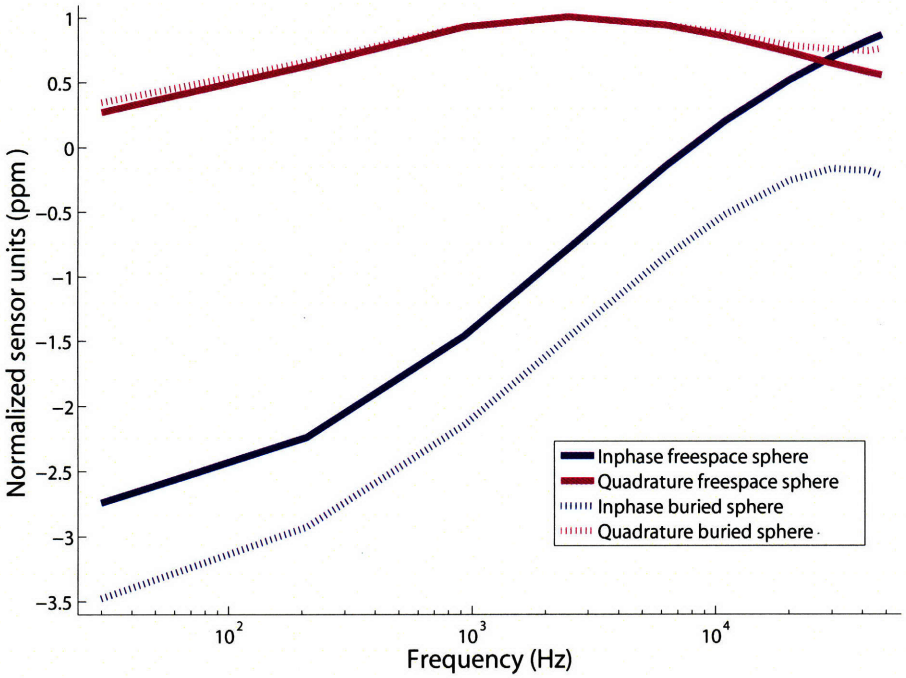

Figure 2-14: Comparison of EMI measurement of a steel sphere in free space and buried under soil. Responses have been normalized relative to the quadrature signals to account for any differences in sensor to target distances. Measurement data courtesy of CRREL.

highest frequencies are most likely distortions, as the instrument is prone to some amount of drift in that domain.

2.3.7 Retrieving Soil Information from the Measured Ground Response

Given EMI measurements of the ground response, one can ascertain the relative permeability values of the soil in question by utilizing the previously mentioned half space soil model and a sufficiently accurate model of the sensor in use. Shown in Figure 2-16 is the comparison

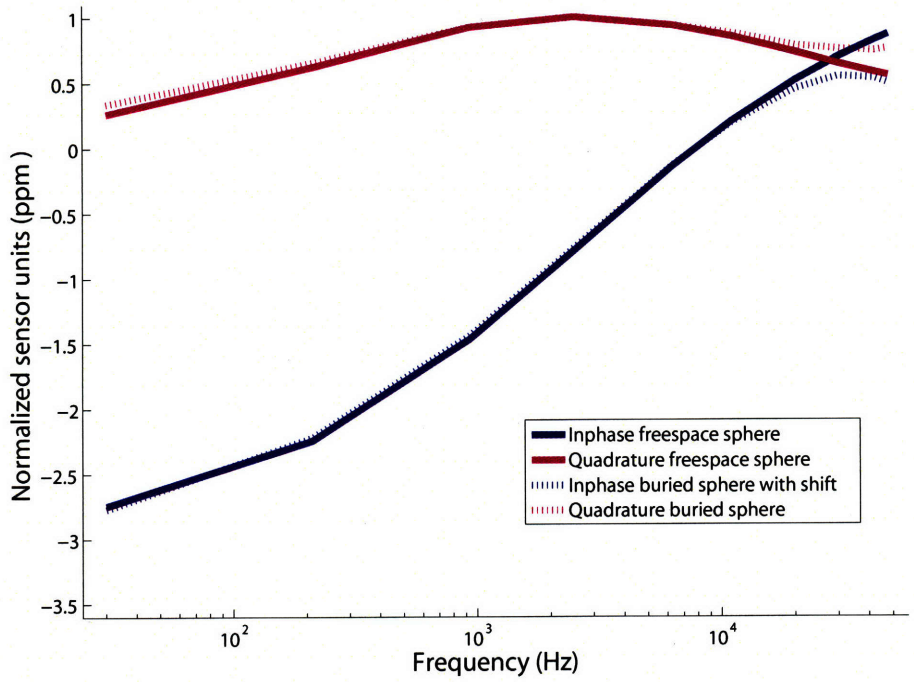

Figure 2-15: Comparison of EMI measurement of a steel sphere in free space and buried under soil. The depicted data is the same as the data for the previous figure but now the Inphase response of the buried sphere has been shifted by 0.71 (normalized ppm). The agreement between the two sets of curves demonstrate the effect of the presence of soil to air interface is limited to only a superposition of a Inphase response that is constant over frequency.

between the measurement of a soil test bed located at CRREL and the fitted model. Again, this soil is considered "common" backyard soil and is not known to be particularly magnetic or conductive. This view is corroborated by the measurement data: the response is dominated by the Inphase signal which can be attributed to a relative permeability of less than 1.0008.

The recovered soil μ value is well within the range typical of most soil [74]. This value is found by utilizing the forward model of a halfspace response as described by Equation 2.32. Various values for the soil μ parameter are tested until the best match to data is obtained. Though the Inphase signal is not perfectly constant, the deviation is small enough that it can be attributed to sensor drift or general noise. The non-zero value of the Quadrature signal can also be attributed to these same factors. At most, one can say the soil may be very weakly conducting. More complex soil models have been proposed which account for frequency dependent susceptibility [23–27]. But given the minimal evidence of relaxation or frequency dependent susceptibility in these measurements, the inversion analysis presented in subsequent chapters will consider the simple non-conducting homogeneous halfspace as a sufficient soil model.

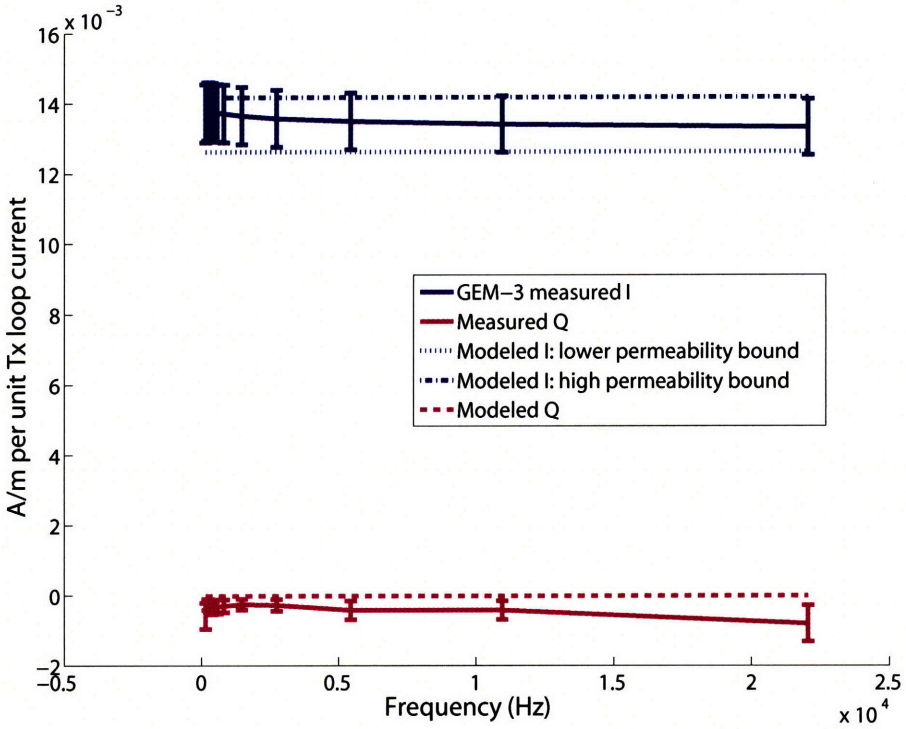

Figure 2-16: Comparison of EMI measurement of soil and fitted permeable halfspace model. This fitting enables one to ascertain the soil permeability from in-situ measurements. For this sample, the relative permeability is about 1.0007, with a range of roughly 1.00066 to 1.00075 found by fitting the modeled curves to the upper and lower bounds indicated by the error bars. Measurement data is courtesy of CRREL.

2.4 Modeling of the Interactions between Sensor and Target for Physical Interpretation of Measurement Data

Given that secondary fields are always dependent on primary fields, a complete forward model of UXO in realistic environments as measured by real instruments also requires an accurate model of the sensor in use. Much of the research in inversion relies on using third-party, proprietary instruments. Therefore, knowledge of the inner workings of these instruments may be limited. While, for example, the geometry of the transmitter coils may be divulged by the manufacturer, often the measurements of induced secondary magnetic fields are reported in some units that are effectively arbitrary relative to standard EM units such as A/m or Teslas. This situation is the case with the frequency domain EMI sensor, GEM-3, used by this investigation.

The lack of understanding of the target to receiver interaction can have a significant impact on inversion studies. A very clear example of this impact can be shown in the procedure to recover soil permeability as described in the previous section. One must match the measured secondary response with the analytical model of a half-space response. The susceptibility of the soil corresponds to the value of the model's susceptibility parameter that produces the best match to calculated response. However, in order to do such comparison, one first needs to convert all sensor readings into units consistent with the model of the soil, e.g. standard EM units used in the calculations of the soil response. The work described in

this section details obtaining such a conversion to permit meaningful comparison between modeled and measured data. The retrieval of soil permeability and the ability to classify objects based on their measured EMI responses, described in a following chapter, is possible due to the success of this research in converting the measurements obtained by the GEM-3 instrument into units consistent with forward models.

2.4.1 Previous Work

In many prior studies of this nature, the secondary fields are reported in units of parts per million (ppm) of the primary field intensity [8, 15, 22, 35, 36, 42, 44, 59, 64, 69, 100, 101]. Examining the past work reveals one key aspects which differentiates the work presented in this thesis. The prior studies assumed that the results reported by their instruments were truly ppm relative to a specific primary field sample. When such an assumption is made and knowledge is available of how the primary field is sampled, this type of normalized secondary fields as reported by the instruments can be modeled analytically. Therefore, there is no question of how to compare a model's output to measurements. Given that many of the authors of those studies participated in the manufacture of the instruments in the references cited, this may be a fair position for them to take. However, many researchers involved in UXO inversion studies often purchase instruments from third parties and may not be privy to the detailed inner mechanisms of such devices. Therefore, a complete analytical or even numerical model to calculate the ppm secondary fields may not be possible.

While it may be possible to directly measure the primary fields created by the instru-

ment's transmitter, such measurements cannot characterize any post-processing of an object's response as received by the instrument to create the measured data. Many modern EMI detectors include filters, amplifiers, etc, attached to particular components, the details of which a general user has no way of knowing. Therefore the user is without knowledge of the relationship between actual transmitted and received fields in A/m or Teslas and the units of the reported measurement.

This argues for a simple, fast, non-invasive method of both assessing the performance of instruments and converting the measurements into known, universal units. The latter goal is required to compare secondary fields produced by a model with measured data and produce scientific inferences, such as estimates of ground magnetic susceptibility.

2.4.2 Research Overview

The GEM-3 instrument as shown in Figure 2-17 used throughout this study is a very typical EMI instrument in that it reports secondary fields in terms of ppm but the instrument is not known to have any adaptive processing properties. Therefore one can assume that the instrument always obtains signals from received fields in the same way. The instrument's transmitter consists of current carrying fixed loops. The size and physical properties of these loops are known. But the specific current carried on these loops is unknown and not particularly important given that all received fields are normalized by some sample of the primary field. Therefore, the relationship between the measured secondary field reported by the GEM-3 and any modeled response given the same loop geometries and an arbitrary

assumed constant transmitter current would amount to a scaling factor, a constant K:

$$H_{\text{GEM-3}} = K \cdot H_{\text{model}}. \tag{2.55}$$

To recover this scaling factor, this study utilizes three metallic spheres to calibrate the modeled response to the GEM-3 measurements. This comparison between modeled response and measurements will determine the correct scaling factor. The full characterization of the GEM-3 sensor consists of three parts:

1. Create model of GEM-3 transmitter loops
2. Create model of receiver loop
3. Recover translation factor that converts instrument readings into the units consistent with the modeled received field.
   (a) Measure canonical objects using the GEM-3 instrument.
   (b) Model the response of the canonical object using the model of the GEM-3 transmitter to generate the primary field.
   (c) Scale the modeled response to match the measurement.
   (d) Repeat for many different sensor positions and targets types to ensure accuracy.
   (e) Note the scaling factor from (c)-(d) and retain for use in converting signals from other cases into standard EM units.

Figure 2-17: Photograph of the GEM-3 instrument. Courtesy of CRREL.

2.4.3 Modeling of the GEM-3 Sensor

The GEM-3 sensor is manufactured by Geophex [93]. The transmitting sensor head consists of two current carrying loops with radii of 20 cm and about 11 cm. The smaller loop is placed concentrically inside the larger loop and serves as a bucking coil, approximately nulling the primary field at the center of the sensor head, where the receiver coil resides. There are 8 windings in the outer and 4 windings in the inner transmitter coil. This study assumes the wires in the transmitter coils carry 10 Amps, reflecting the actual current for the device's lower operating frequencies. As mentioned earlier, this is not necessarily the true amount of current in use by the GEM-3 at all frequencies. However, the instrument is designed to report measurements as if some fixed level of current is in use at all frequencies. Therefore, the assumption of any amount of constant current within the model is valid: the recovered

conversion factor is not designed to convert GEM-3 measurements into the actual A/m units of the secondary field that was created during the measurement process. Rather, the factor will convert the measurements into the framework of the model with the assumed 10 Amp current. As long as one remains consistent in using the same model for the transmitter coils in all inversion studies, the recovered conversion factor will always be valid.

2.4.3.1 Modeling of Transmitter Current Loops

A set of idealized wire loops can be used to analytically model the GEM-3 instrument. The complete elliptical integral functions of the first and second kind can characterize the magnetic vector potential and vector field from a circular current loop in a cylindrical coordinate system. This calculation method is well established [67, 75, 83]. For a current loop of radius a and the plane of the loop normal to the z axis in the $z = z_o$ plane and with I_o current flowing in the ϕ direction, the transverse and axial fields are,

$$B_r(r,\phi,z) = \frac{\mu_0 I_o}{2\pi} \frac{(z-z_0)}{r[(r+a)^2+(z-z_o)^2]^{1/2}} \cdot \left[-K(k_c) + \frac{r^2+a^2+(z-z_o)^2}{(r-a)^2+(z-z_o)^2} E(k_c)\right] \quad (2.56)$$

$$B_z(r,\phi,z) = \frac{\mu_0 I_o}{2\pi[(r+a)^2+(z-z_o)^2]^{1/2}} \cdot \left[K(k_c) - \frac{r^2-a^2+(z-z_o)^2}{(r-a)^2+(z-z_o)^2} E(k_c)\right], \quad (2.57)$$

where

$$k_c = \sqrt{\frac{4ar}{(r+a)^2 + (z-z_o)^2}}. \tag{2.58}$$

K and E are the complete elliptical integral functions of the first and second kind, respectively. These equations will produce the primary magnetic fields at any position. The variables (r, ϕ, z) are coordinates in the standard cylindrical coordinate system.

The total primary field of the GEM-3 is created from the superposition of two current loops that correspond to the two actual transmitting loops in the sensor head. The model agrees with the alternative method of using numerical brute force integration and application of Biot-Savart's Law as shown in Figure 2-18. The elliptic integral model has the added benefit of being computationally more efficient and is therefore used in all simulations.

2.4.3.2 Modeling of Receiver Coils

The secondary magnetic field is captured by the current generated on a pickup coil in the center of the GEM-3 by the time varying magnetic field. The pickup coil may either lie on the plane of the instrument allowing the GEM-3 to record the field in the z direction or additional coils may be mounted perpendicular to the the plane of the instrument, allowing measurements of the activity in the x and y directions to be possible. In all cases, the instrument reports the response in units that are proportional to the integral of magnetic flux over the receiver coil or coils, normalized by the transmitted field as sampled by an additional coil within the sensor head to produce ppm. It is of some importance to point out that the GEM-3 reports measurements that are proportional to B_z, not $\partial B_z/\partial t$ as one

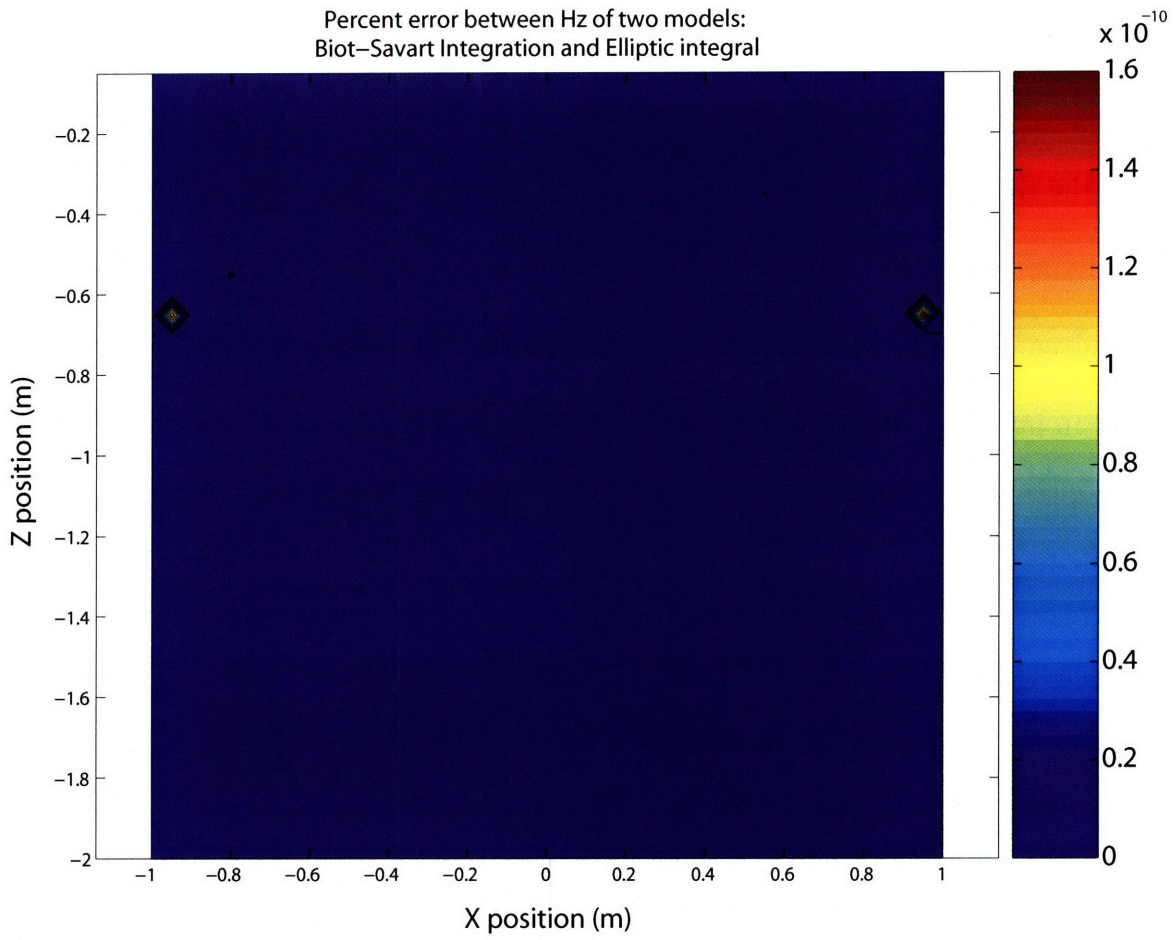

Figure 2-18: Percent error between the elliptic model of a current carrying loop and the Biot-Savart brute force integral model of the same loop. The loop is located at the origin. The difference is given a percent error and plotted over space.

might expect. But since the instrument is proprietary, the exact mechanism behind this measurement and other post processing effects are not known.

Furthermore, in the past, the receiver coil was always taken to be of negligible size so that the modeled response of any target is only calculated at a single point per measurement position, usually coinciding with the center of the receiver loop. The sampling at this single point was considered adequate to characterize the average of the magnetic fields passing through the finite sized receiver loop. Therefore, no specific model of the receiver loop was previously implemented.

But given that the receiver loop is 6 cm in radius and that accuracy is of utmost importance in inversion, the impact of a finite receiver loop size was deemed worthy of further investigation. If the sensor is close to the target, the field at the center of the loop can be much higher than the average of all the fields passing through the receiver as shown in Figure 2-19. This figure shows the sampling of the magnetic fields within the receiver loop area. The fields are produced by a modeled steel sphere 13 cm below the sensor. This sphere is 3 cm in radius with $\mu_r = 100$ and $\sigma = 1 \times 10^6$ S/m. The sample at the center of the loop differs from the overall average by more than 14%. When the target is relatively far away, as shown in Figure 2-20, the error reduces to about 2%.

The previous examples show that one must integrate to produce an accurate model of the actual received fields. Since this integration must be numerical, the question of fineness of the discretization must be answered. Shown in Figure 2-21 is the value of the integral of the fields over the loop area as a function of the number of discretization divisions. Good

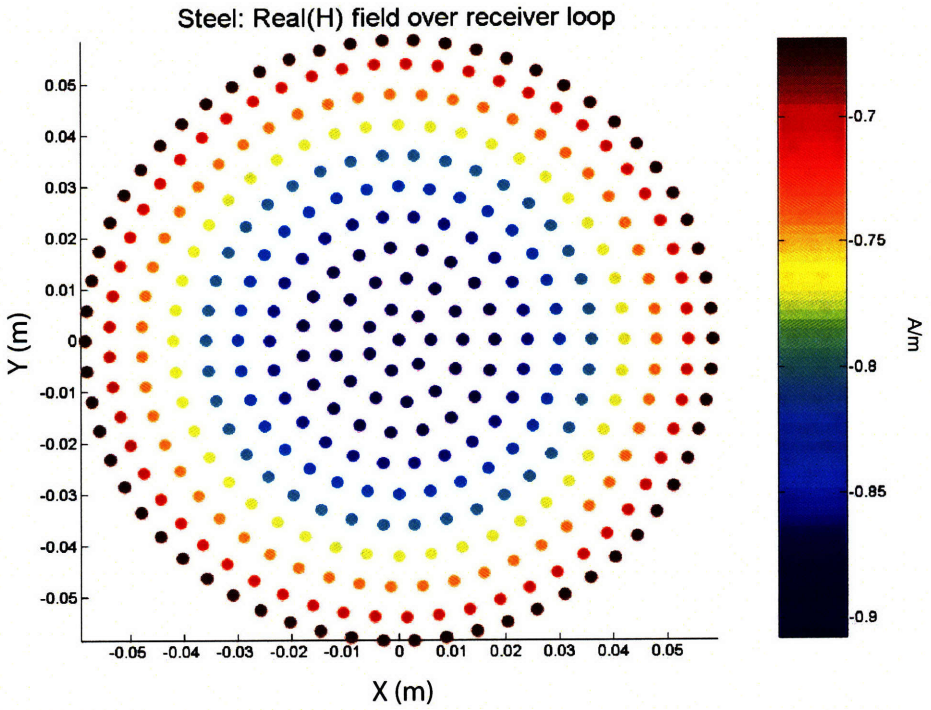

Figure 2-19: Sampling of the modeled magnetic fields within the receiver loop produced by a 6 cm radius steel sphere at 13 cm directly beneath the sensor. The sample at the center of the loop differs more than 14% from the true average of the magnetic fields across the loop area.

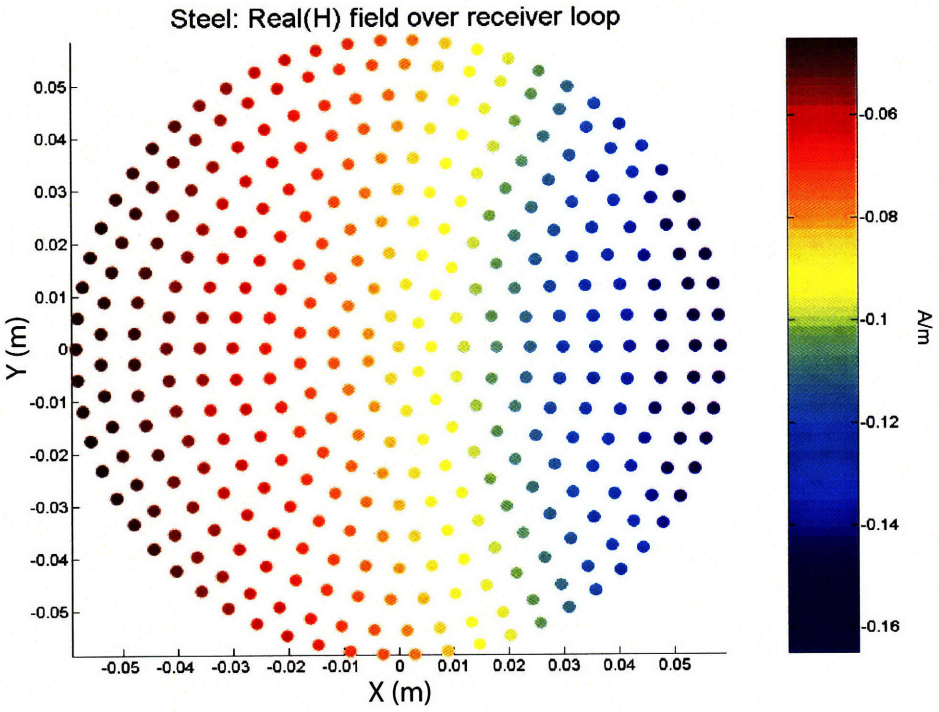

Figure 2-20: Sampling of the modeled magnetic fields within the receiver loop with produced by a 6 cm radius steel sphere at 13 cm beneath and 30 cm laterally displaced from the sensor head. The sample at the center of the loop differs only about 2% from the true average of the magnetic fields across the loop area.

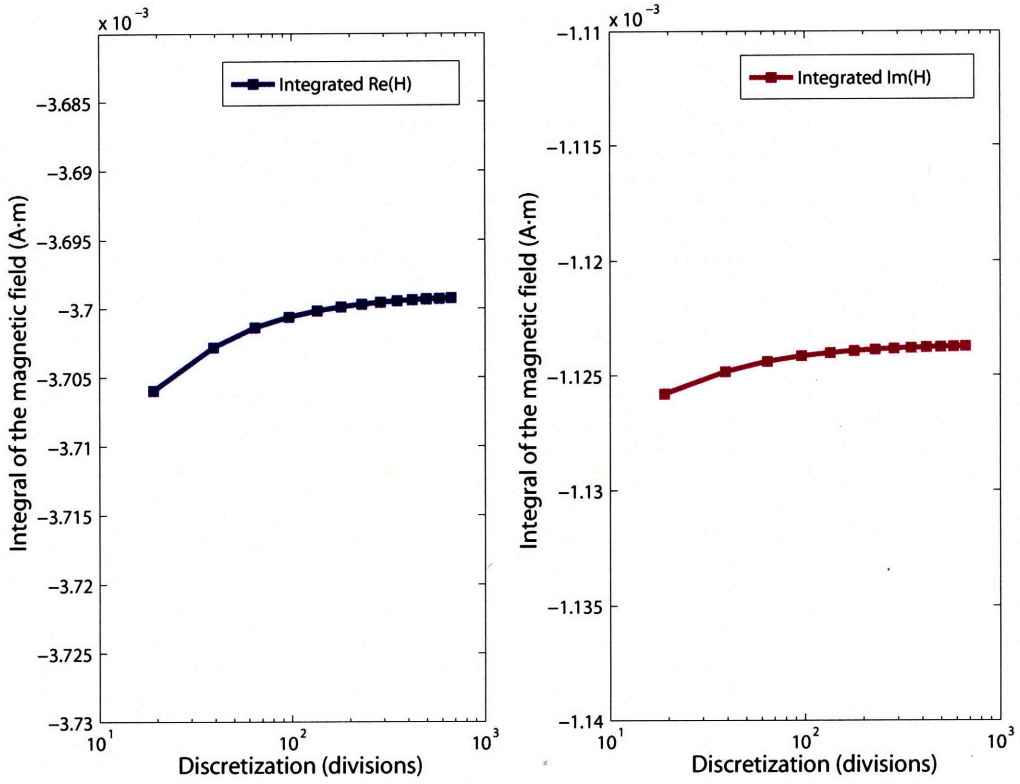

Figure 2-21: The value of the integral of the fields over the loop area as a function of the number of discretization divisions. Good convergence is seen for over 300 divisions.

convergence is seen for over 300 divisions.

2.4.4 Modeling of Metallic Spheres

We model metallic spheres as a special case of the spheroid model. This model is well validated and produces EMI secondary field predictions for spheroidal objects with any conductivity and permeability values and in response to arbitrary excitation [3,5,12]. Furthermore, the model produces secondary field predictions in terms of A/m. The three specific objects that were modeled correspond to the measured metal spheres: steel, brass, and aluminum, all 3 inches in diameter as shown in Figure 2-22. The exact material parameters were not

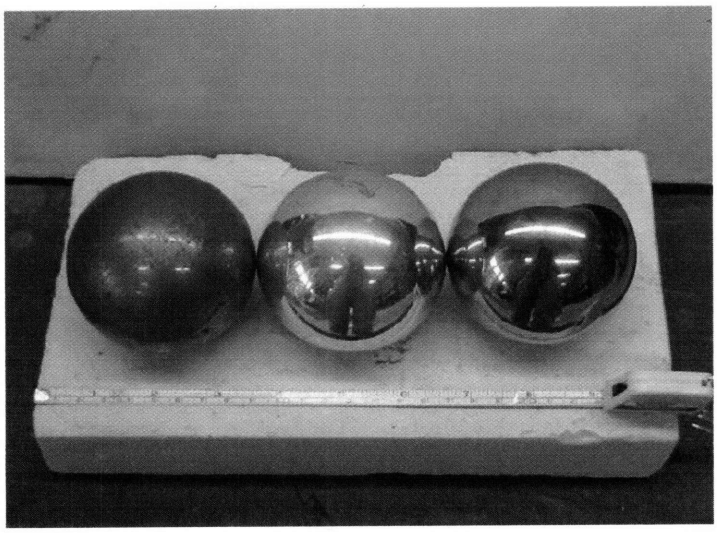

Figure 2-22: Three metal spheres used in GEM-3 calibration. From left to right: brass, aluminum, and steel. Photograph courtesy of CRREL.

provided. Therefore, recovery of those parameters was also a part of the process to obtain the scaling factor which will be described in later sections.

2.4.5 Calibration of Sensor Measurement Data to Modeled Response

2.4.5.1 Measurements

Measurements were taken of each metal sphere shown in Figure 2-22 by placing the GEM-3 instrument above at points in a 2-D vertical grid. Horizontal spacing was in 2 cm increments from -30 cm to +30 cm across the sphere. Vertical spacing was in 5 cm increments from 13 cm to 28 cm above the surface of the sphere. The frequency range was from 30 Hz to 47 kHz. This wide range of measurement points both in space and frequency was taken to

ensure that the recovered scaling factor is consistent: given that the GEM-3 is not adaptive, there must not be any variation due to object distance, frequency, or choice of target object. In other words, all the data must point to a scaling factor of the same value.

2.4.5.2 Matching Algorithm Utilizing a Fibonacci Search

The main impedance to the recovery of the scaling factor is the uncertainty of the metallic spheres' exact permeability and conductivity values. Therefore, to match the model's EMI prediction with measurements, both the scaling factor and μ and σ must be simultaneously recovered. As a simplification, the aluminum and brass spheres can be assumed to be non-permeable, and thus only their σ values and the scaling factor need to be recovered. Approximate values of σ for these materials are available from standard textbooks, furnishing a reasonableness check. For the highly permeable steel sphere, only the ratio between σ and μ affects the secondary response [79]. Therefore, relative μ is assumed to be 100 and σ/μ ratio is recovered along with the scaling factor.

A Fibonacci search is applied on the range of possible values for each of these variables [32]. To perform a Fibonacci search, one must first determine the range of possible values for the parameter that one is searching. One must specify the upper and lower bounds the underlying conversion factor and σ or σ/μ should fall within. The range of values forms the search domain. This search domain is divided into two parts. A candidate value for the unknown parameter is drawn from the middle of the first domain and a second candidate value is drawn from the middle of the second domain. Whichever part produces a better match will become the new search space and the process repeats until a sufficient number of

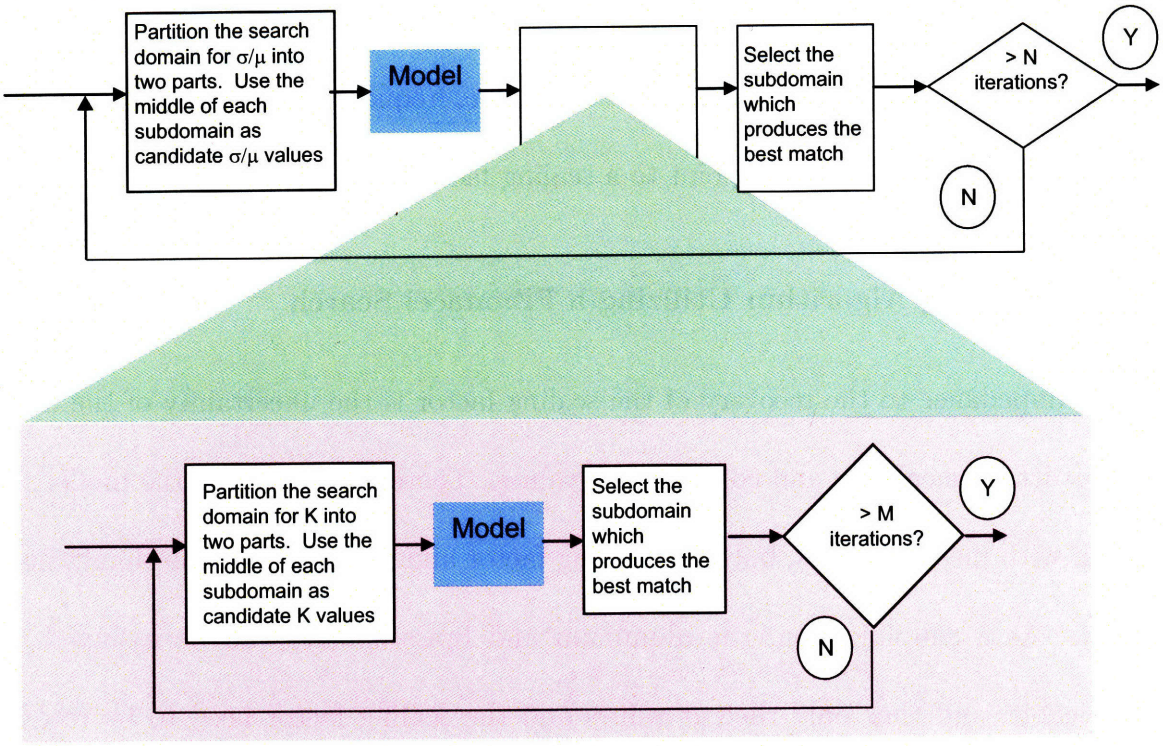

Figure 2-23: Flowchart depicting a nested Fibonacci search.

iterations have passed or the solution has met some quantitative measure.

Since the problem at hand requires solving for two parameters, the scaling factor K and σ/μ, two Fibonacci searches may be nested as shown in the flowchart of Figure 2-23.

This search method converges very quickly by eliminating half the search space in each iteration. To prevent convergence on incorrect solutions, a reasonable initial search space for K and σ/μ must be chosen. In this study, the bounds on σ for brass are from 0.7×10^7 to 4×10^7 S/m. For aluminum, the bounds were from 1.5×10^7 to 3.4×10^7 S/m. For steel, the bounds on σ/μ are from 6×10^4 to 9×10^4. In all cases, the bounds on the search space for the scaling factor K are from 4×10^3 to 6×10^3.

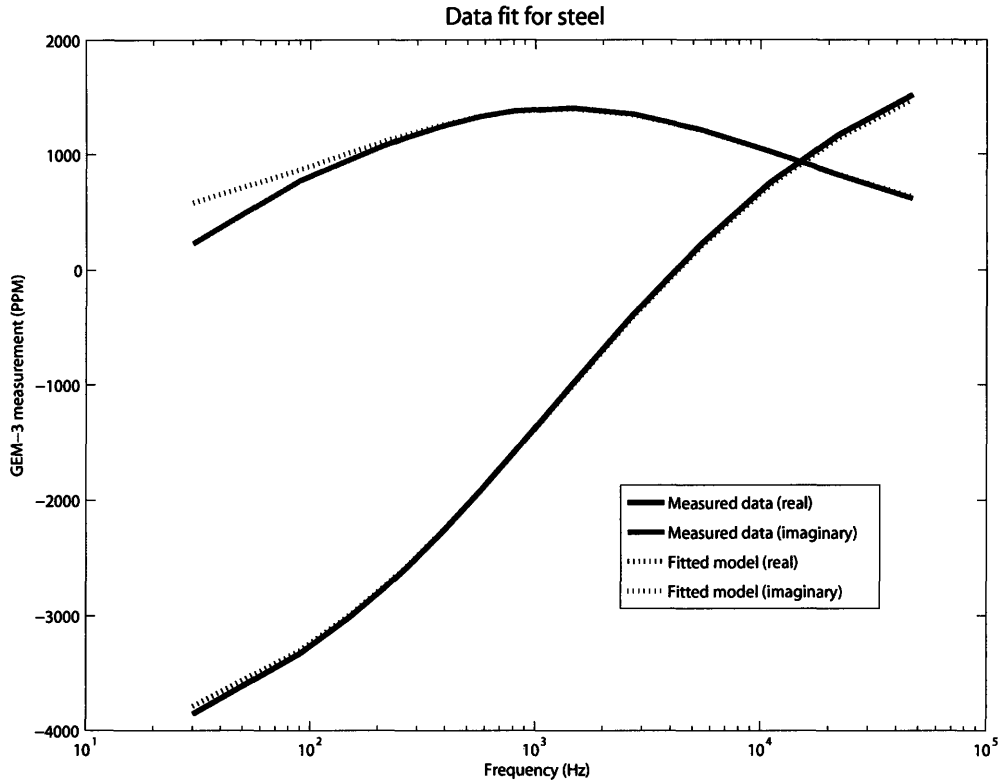

Figure 2-24: Figure showing the matching between model and measurement of a steel sphere at a single grid point.

2.4.5.3 Matching Results

Figure 2-24 shows the match between the modeled response and the measurement of the steel sphere. The match is extremely well save for the lowest and highest frequency points. We have observed that the GEM-3 can have difficulties capturing consistent responses at very low and very high EMI frequencies. Therefore, the lowest and highest frequency data are ignored during the matching process. After repeating this search for every measurement of the steel sphere, one can examine the scaling factor recovered at every sensor position.

Figure 2-25 plots the recovered conversion factors for the steel sphere as a function of

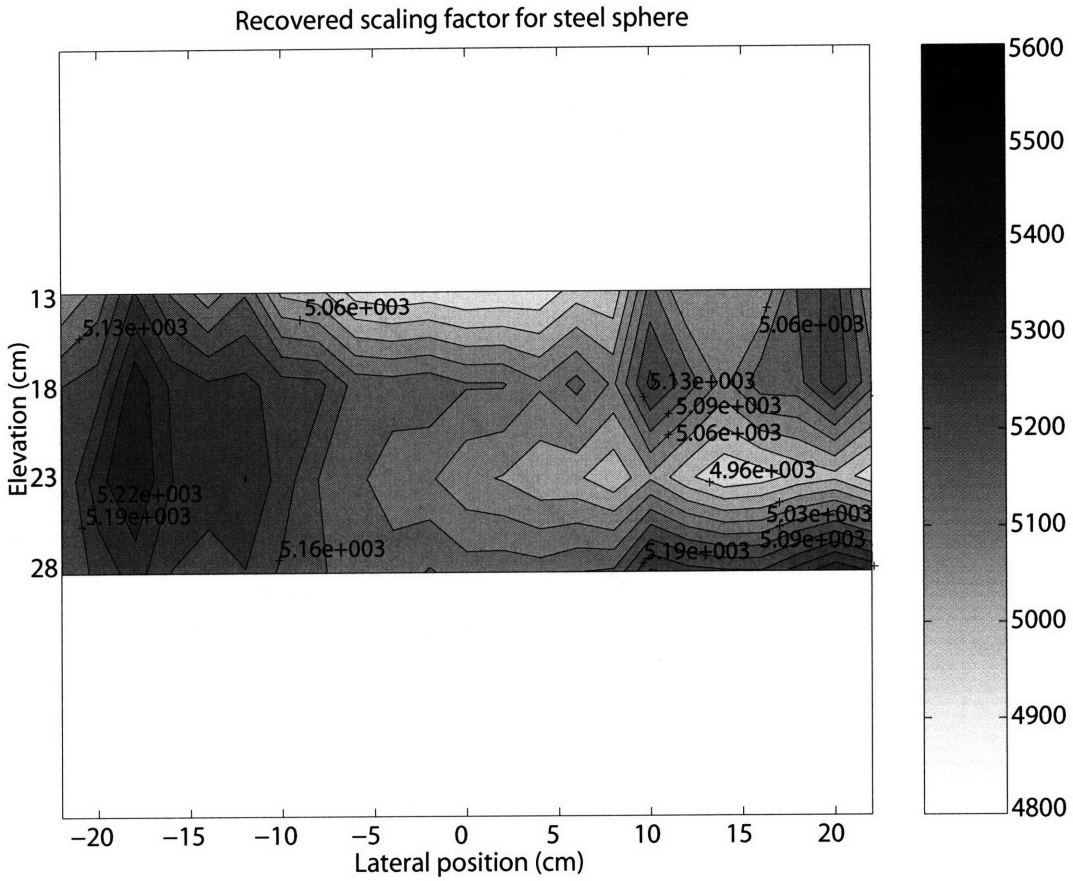

Figure 2-25: Plot of the retrieved conversion factor for the steel sphere as a function of position.

position, assuming the GEM-3 is positioned at (0, 0) on the axes. This analysis is useful because the scaling factor must be constant over space given that the instrument is non-adaptive. Any radical departure from this phenomenology would signify that either the matching algorithm and the recovered scaling factor are incorrect or that the instrument does not behave as advertised.

Figure 2-25 as shown is not particularly illuminating, but all the data can be converted into a percent error from the averaged conversion factor of 4.93×10^3. This variation of the scaling factor can likewise be plotted over space, shown in Figure 2-26. As the figure

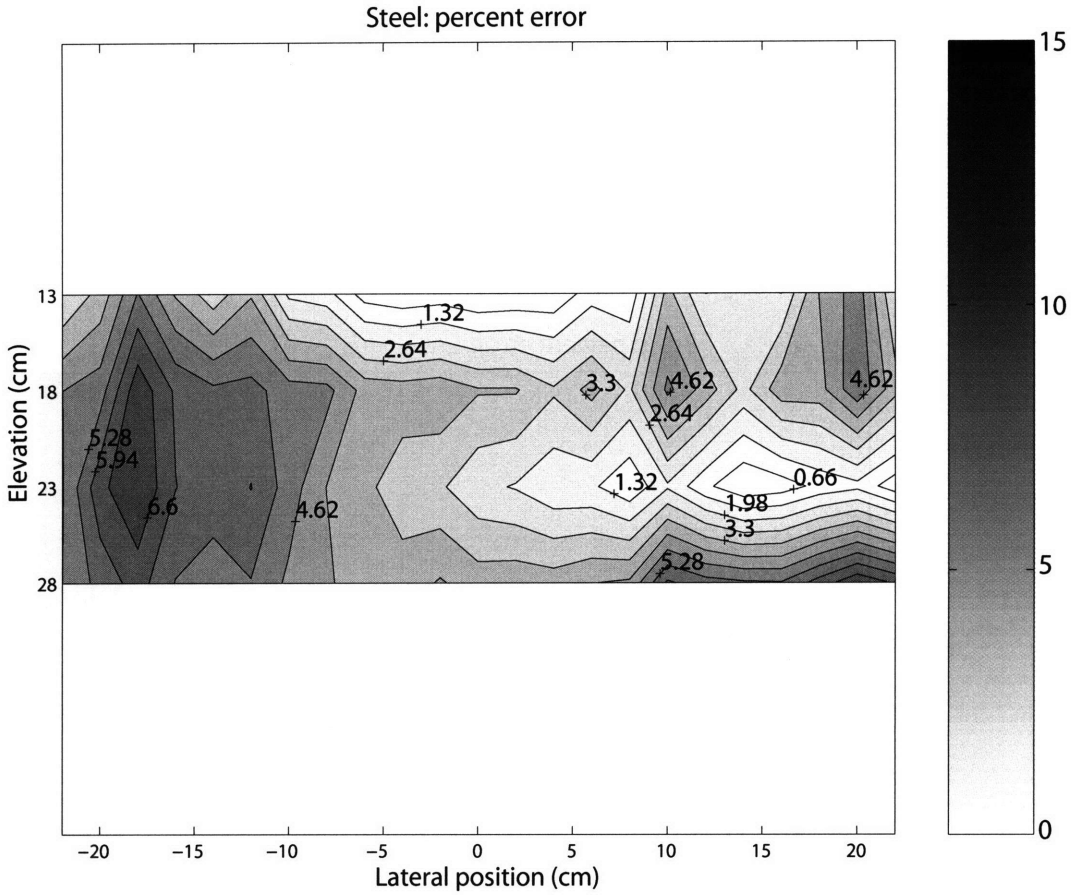

Figure 2-26: Plot of the variation of the retrieved conversion factor, as a percent error from 4.93×10^3, for the steel sphere as a function of position.

demonstrates, the variation is minimal with under 5% error. One can see similarly good results for the brass and aluminum spheres shown in Figures 2-27 and 2-28, respectively.

2.4.6 Effect of Finite Receiver Loop Size

If we can assume the secondary field is constant over the receiver loop, then it would be unnecessary to numerically integrate the fields within the loop area. This shortcut would save considerable computational time since the forward model would need to calculate only once per grid point as opposed to over 300 times per grid point. Shown in Figure 2-29 is

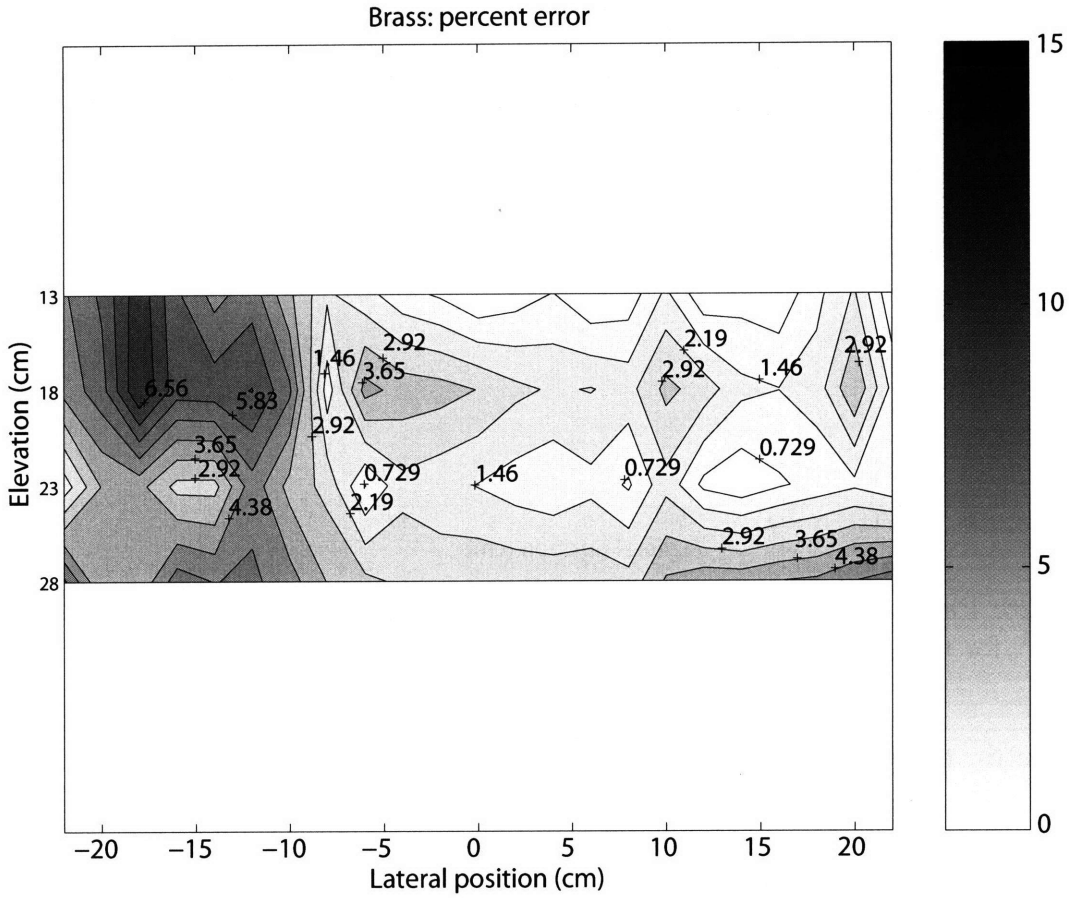

Figure 2-27: Plot of the variation of the retrieved conversion factor, as a percent error from 4.93×10^3, for the brass sphere as a function of position.

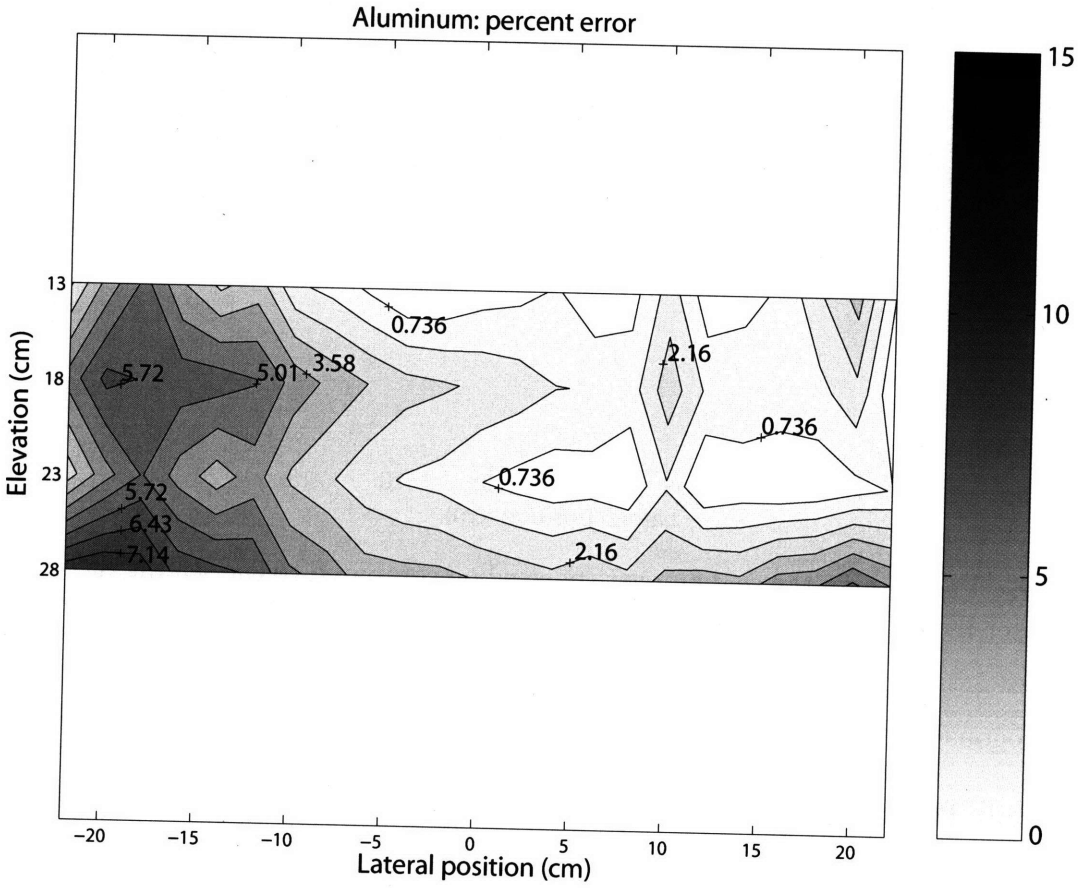

Figure 2-28: Plot of the variation of the retrieved conversion factor, as a percent error from 4.93×10^3, for the aluminum sphere as a function of position.

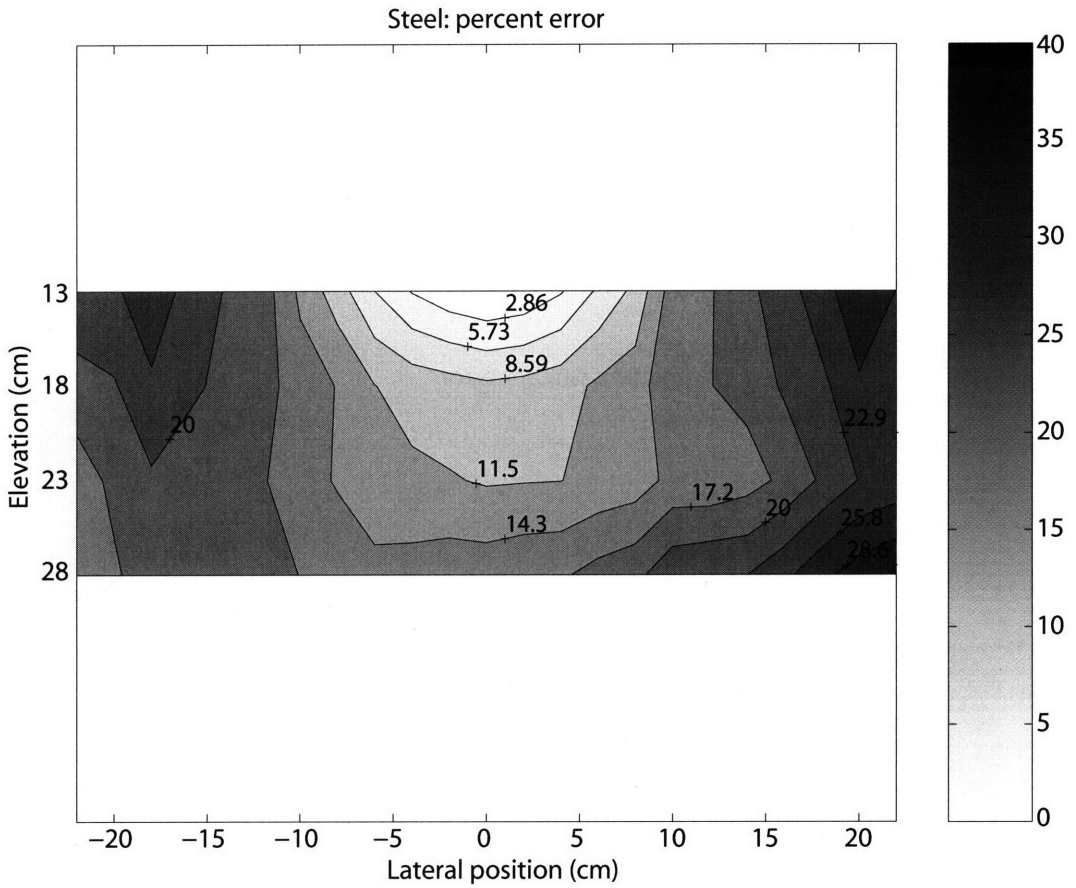

Figure 2-29: Variation of the scaling over space when compared to the scaling factor recovered at the closet measurement point. This high amount of variation is undesirable.

data analogous to Figure 2-26 except that no numerical integration was performed over the receiver coil. The average magnetic field over the receiver loop was assumed to be the same as the field in the very center of the loop. Using this method, a new scaling factor, averaged from the closest 9 measurement points, was obtained: 4.24×10^3. Since the figure shows spatial variation of over 20% for the scaling factor from the averaged value, we conclude that numerically integrating the fields within the receiver loop is necessary.

This variation of error is very systematic as would be expected given the pattern of deviation as seen in Figures 2-19 and 2-20.

The current section has shown that integrating over the receiver loop area has considerable effect in one's ability to match a modeled response to measurement. However, in future work, the significance of this mismatch should be cast in terms of one's ability to do correct and meaningful inversion.

In all prior studies using the GEM-3 instrument or similar instruments with receiver loops, no such integration over the receiver loop has ever been used in conjunction with inversion studies. This omission is due to the increased computational demand: integration will create the need to calculate the response of the object at many points per measurement position and thus may create difficulties if one seeks to model many objects within a timely manner. If omitting the integration can still produce acceptably good discrimination results, then the mismatch may be disregarded.

2.5 Conclusion

This chapter discusses modeling of buried UXO. It is shown that several forward models of UXO and spheroids are available. Furthermore, the limitations of the dipole model are evident when one attempts to model heterogeneous objects. Previous work has shown that the coefficients of the spheroidal response modes, B_k^j , can be retrieved from data and that these coefficients can uniquely characterize an object and its response. Therefore, as a natural extension, B_k^j is retrieved from measurements of a UXO and shown to be accurate in predicting that object's response at new sample points. This work, in effect, produces a new forward model.

These models, however, only produce the objects' response in freespace. Therefore, research is done into the effects of a discontinuous background medium, created by the permeable soil to free space interface, on the response of buried targets. Through the implementation of an approximate model for a buried sphere, the effects are shown to be limited to a superposition of a halfspace response for realistic soil permeability values. This superposition effect enables one to model buried all metal objects in the EMI regime.

It is also shown through comparison between permeable halfspace models and measurements of soil that soil permeability values can be retrieved. However, to do this direct comparison between model and measurements, characterization of the sensor is required. Since the sensor used by this study reports the measured magnetic fields in unknown units, this investigation obtained a conversion factor to transform instrument readings into known units consistent with models.

This realization of a complete model of the measurable response of buried UXO enables one to proceed with inversion studies which produce methods that identify or classify unknown objects based on their EMI responses.

Chapter 3

Inversion Through Application of Differential Evolution: Identification

3.1 Introduction

Predicting the output of a system given specific input values requires a model that follows some basic underlying laws governing the system. This prediction constitutes the "forward problem." Conversely, the "inverse problem" attempts to recover the input values when given the response of a system.

The forward problem in regards to UXO research can be resolved with accurate modeling of UXO objects and the environment. As shown in the previous chapters, several reliable forward models have been developed and are readily available. That aspect of UXO research is relatively mature.

However, the inverse problem of identifying UXO objects through their EMI responses is a

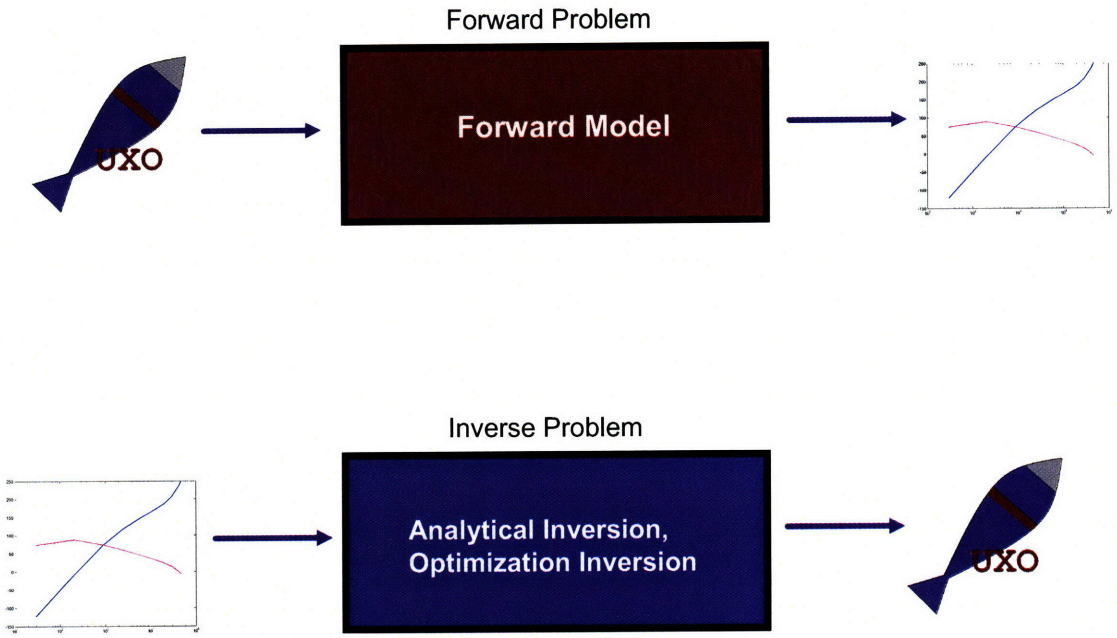

Figure 3-1: Inversion problem and forward problem as they pertain to UXO. The previous chapter concentrated on solving the forward problem for UXO in realistic settings. The current and next chapters focus on the inverse problem of identifying or classifying UXO based on their EMI response.

topic currently of great interest. As illustrated in Figure 3-1, this work directly addresses the motivation behind UXO research: to lower false alarm rate, one must be able to discriminate the response signals produced by UXO from those produced by clutter items. Discrimination entails utilizing the response signal to identify the specific target object or simply make a binary decision whether target is a UXO or not. However, since the inverse problem for UXO is still plagued with many difficulties, it is still an area of active research.

There are several approaches to general inverse problems. If the system can be described by a set of linear equations, the input parameters can be solved when given sufficient output data. If the system is non-linear but characterized by a closed form expression, the inverse problem can often be solved through various calculation techniques such as the Gauss-

Newton algorithm. However, given the complexity of the UXO problem where the target is often buried at an unknown location, depth, and orientation, no closed form expression can completely describe the entirety of the system.

3.1.1 Previous Work

The previous studies on the inverse UXO problem encompass a broad spectrum of methods to represent the target and algorithms to compute the inverse solution. These studies propose various ways of uniquely characterizing UXO: dipoles model parameters [41], response decay constants [81], or by a Gaussian function fitted to the response measured over a plane [91]. The authors of those studies suggest that such characteristics can form the features by which objects can be identified or classified.

Given the EMI response characteristics, the authors go on to suggest various classification or identification algorithms which span everything from supervised machine learning such as neural networks or statistical comparisons [17,52,81,94], or Bayesian measures [80], simulated annealing [95], or other form of pattern recognition [31]

3.2 Research Overview

The inverse problem for UXO encompasses two general forms. The first form, addressed in the current chapter, uses the EMI response signal to resolve the identity of the target from a library of standard, representative UXO types. Items whose identities cannot be resolved are then considered clutter items. The second form of inversion, addressed in the

next chapter does not identify particular UXO but makes a general discrimination between all UXO targets and clutter.

One can view the object identification problem as a type of optimization problem. Optimization describes a process where one searches for the optimal values of a model's input so that the model's output will correctly match given data. Cast in terms of the UXO problem, optimization requires measuring the EMI response of the unknown target in question and comparing this signature to the predicted responses from a library of models for possible UXO targets. The input parameters of the models are adjusted until the "best" match, as evaluated by an objective function, is achieved. The member of the library which produces the closest match with an acceptable level of accordance will correspond to the identity of the unknown object. The general procedure is shown in Figure 3-2.

There are three basic components of the optimization inversion scheme: the model, the search algorithm, and the objective function. Each component has the potential of rendering the optimization unsuccessful and must be thoroughly evaluated and tested [97].

1. The Model: To make the calculation tractable, the model must be computationally fast because the optimization process will require many evaluations over the course of the search process to find the most optimal input parameters. The fundamental mode model and the spheroidal mode model are both analytical models which only involve the summation of a finite number of response components, represented as magnetic charges or B_k^j modes respectively, and do not involve inverting large matrices. Therefore, both are comparably fast and suitable for use in an optimization scheme. However, as will

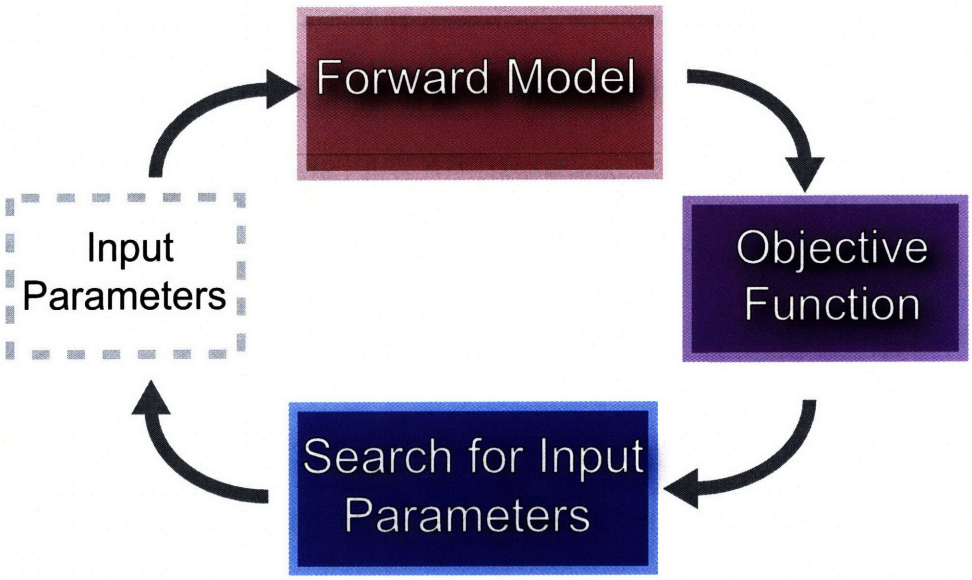

Figure 3-2: Graphic depicting an overview of optimization. Optimization, as it relates to UXO inversion research, is essentially a search to find the most optimal input parameters for a UXO forward model such that its prediction best matches the measured response of an unknown object. By finding the optimal input parameters, one can identify if the unknown object corresponds to any particular UXO and obtain its location and orientation.

be discussed, due to the differences in the specific implementation structure of each model, the fundamental mode model is favored because it can accomodate a faster search method.

2. The Search Algorithm: The process of searching and adjusting the input parameters until a good match between modeled response and data is found requires multiple evaluations by the model. Any actual buried UXO will be at an unknown position and orientation underneath the soil. Therefore the search process involves checking combinations of position and orientation–which are the only inputs of the fundamental mode model–for each library member until the best match is obtained. An exhaustive brute force search would not be feasible even for a relatively fast model such as the fun-

damental mode model. As will be discussed, this study employs differential evolution (DE), a type of genetic algorithm, as an effective search strategy. However, despite the improvement over a brute force method, DE still requires considerable computational time. To counter this deficiency, the DE computation is parallelized using Message Passing Protocol (MPI).

3. The Objective Function: Since the optimization procedure searches for the best match between model output and measurement data, some quantitative measure of "goodness of fit" is required. Normally this measure is a analytical expression for the difference between the model output and data. This expression is called the "objective function." Section 3.4 gives the description of the weighted, normalized difference used to calculate error in this study.

The first topic, the fundamental mode model, has previously been discussed [79]. The second and third topics, the search algorithm and objective function, will be described in detail as follows.

3.3 Background on Differential Evolution

In response to the need for a search algorithm in the optimization scheme, this study implemented a Differential Evolution (DE), a type of genetic algorithm. Genetic algorithms describe a family of algorithms which employ evolution strategy optimization. This form of optimization is based on the genetic mechanisms and evolution in biology. Many possible

solutions to the problem of interest are evaluated by how well they solve the problem. Good solutions are allowed to remain while poor solutions are discarded. This selective process parallels the idea of evolution which mandate the "survival of the fittest" for individuals within a population inhabiting a hostile environment. Very fit individuals are also likely to have fit offspring in the next generation due to passing on favorable genes. The genes of the offspring are similar to but slightly modified from the genes of the parents as governed by the known genetic mechanisms of crossover and mutation. This slight change has the potential of improving the genes which may be passed on to the next generation and so on. This process is mirrored in genetic algorithms. An individual is now a solution to the problem of interest. The population therefore is a finite collection of possible solutions. Instead of a hostile environment determining the likelihood of survival, a solution's "fitness" is measured by how well it solves the problem at hand. Solutions are culled when they under perform. "Generation" in computational terms refers to a complete cycle of evaluation for all the solutions by the objective function. Instead of reproduction, new solutions are generated to be slightly altered versions of the good solutions belonging the previous generation. In subsequent generations, these slight changes should allow the solutions to converge upon the best possible solution. Genetic algorithms have been used to facilitate searches and provide optimal solutions to non-linear problems.

Differential Evolution is largely distinguished by its use of vector differences of randomly selected population members to perturb the current population and produce the subsequent generation. As shown in Figure 3-3, a member of the population is simply a set of input vari-

ables for the model and thus represent one possible solution. These variables have assigned values and are arranged as vectors where each vector represents possible. In Figure 3-3 (a), to determine if member C_1 of the population at generation g should remain in the next generation, it is compared to a new candidate C_1' calculated by altering a random member of the population by the scaled difference of two other random members of the population in part (b). If this new candidate is determined to be more fit, it will replace C_1. For this specific UXO problem, fitness is determined by the closeness of match between the data and the model prediction corresponding to the candidate solution as shown in (c). Quantitative measure of likeness is calculated by an objective function. If the new candidate C_1' is not more fit, then C_1 remains and is carried over into the next generation. The algorithm tests the remaining members of the population in the same manner. Once all members of the population have been evaluated thusly, the population is then at generation $g + 1$ and the process repeats. DE, although relatively slow to converge, has been demonstrated to be resistant to converging on local minima [62]. What this robustness provides is the ability to find the best possible solution instead of converging on a less optimal solution.

Another aspect of DE is that it is very well suited for parallelization since each member of a population can be evaluated independently with regards to whether it should be replaced or be allowed to remain in the subsequent generation. This flexibility allows for decreased calculation time without the loss of the ability to converge on the most optimal solution. Like all genetic algorithms, DE is very computationally expensive. Given the current state of computing power, inversion is very time consuming unless the DE algorithm

is parallelized, using such methods as the Message Passing Interface (MPI) protocol, and run on a supercomputer. For this investigation, the US Army Research Laboratory's High Performance computing center's Cray supercomputers with MPI-compatible software was used to perform the DE optimization.

3.3.1 Background on Message Passing Interface

Message Passing Interface (MPI) was developed by a consortium of computer scientists in industry and academia in 1993 to 1994 to address the need for a portable and consistent protocol for parallelizing programs [1, 2]. MPI has since become the *de facto* standard for parallelizing programs written in many programming languages such as C and FORTRAN and on many platforms. The MPI capabilities are integrated as bindings into the respective compilers.

The MPI protocol is also adaptable for users both unfamiliar and familiar with parallel programming. In its most basic form, a program can be parallelized with only six basic MPI commands. However, MPI also offers up 128 commands if the user wishes to create more complex communication such as distributing calculation work across tree-like topologies. At the heart of MPI are explicit "send" and "receive" commands which allow the user to specify the results that must be reported back by each processor after completing computation. These results are received and aggregated by a root process.

For this inversion study of UXO using DE, each processor is assigned to determine if one member of the current population should be allowed in remain in the next generation. First,

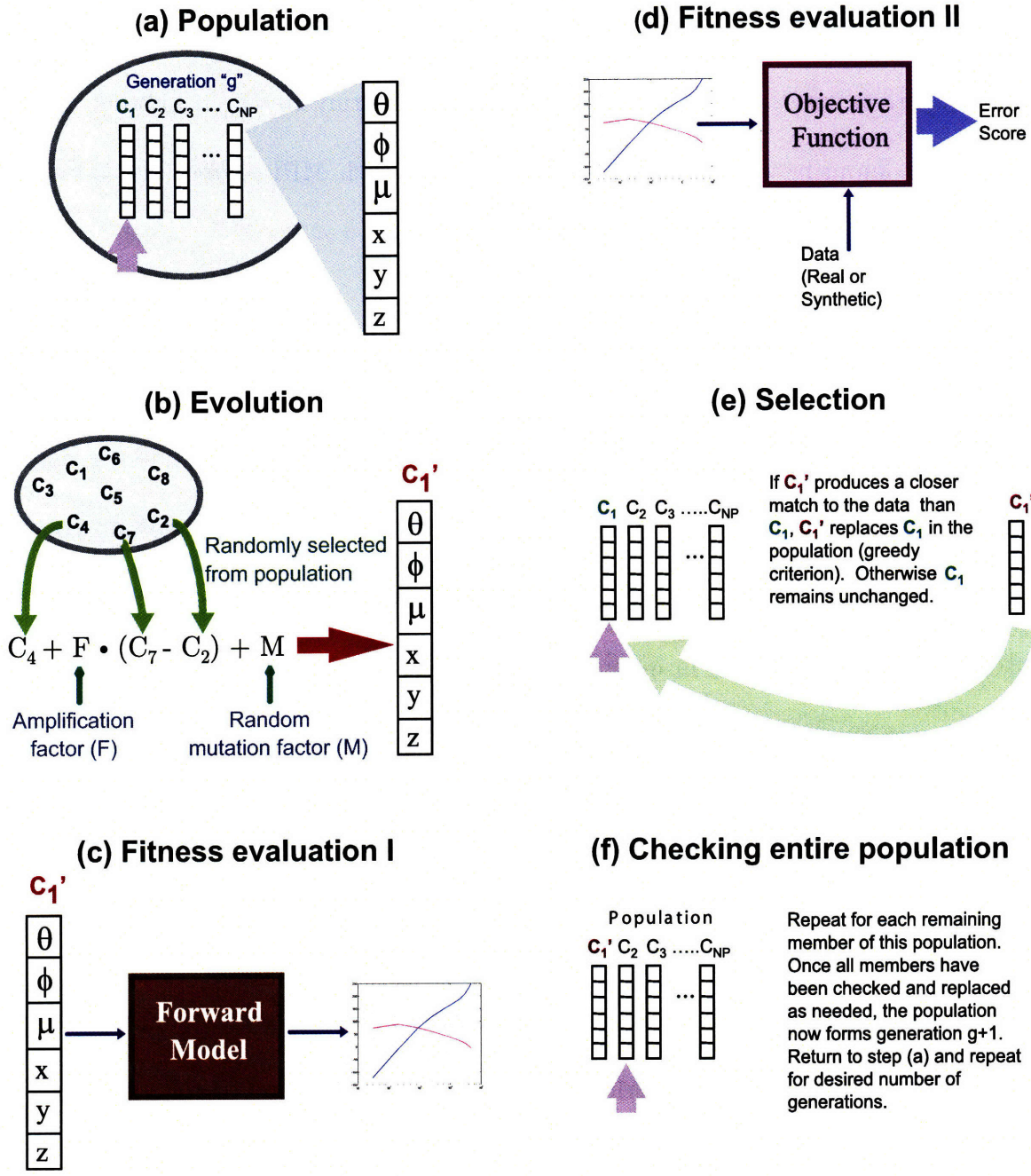

Figure 3-3: Differential evolution optimizes outputs of the forward model to measurements. In step (a), a population is shown at generation "g." To test whether the first member should be replaced, one random member of the population is altered by the differential of two other random members of the population. This new candidate is then used as input into a forward model. The output of the forward model, a predicted UXO response, is checked against the measured data. If the new candidate provides a closer match than the first member of the population, then that member will be replaced by the new candidate. DE then proceeds to check and test the second, third, and subsequent members of the population in the same manner. Once all members have been examined, the generation is then at "g+1" and the process repeats.

the processor creates a potential replacement for one current member as shown in Figure 3-3 (b). Then it calculate the fitness level of the potential replacement. This calculation involves utilizing the forward model to produce the corresponding predicted response for the new candidate population member C_1'. Then the objective function is evaluated to yield the level of fitness. The fitness level of the candidate is compared to the existing population member. Whichever solution is more fit is returned to the root processor which aggregates the solutions from all the processor, increments the generation count, and parcels out the solutions to each processor once again. For this study, the use of MPI is integrated into the FORTRAN implementation of DE and the fundamental mode model.

3.4 Selection of Objective Function

The objective function is a measure of how well a proposed solution satisfies the problem of interest. Various objective functions have been proposed and used in inversion research [43]. For the UXO inversion problem, the objective function must compare simulated EMI responses $H_m^{x,f}$ created by a model to measured "data" EMI signals $H_d^{x,f}$ where each signal provides a sampling of the secondary magnetic field at N_x observation positions indexed by x and N_f frequencies indexed by f. Given the variability of the signal's amplitude across space and frequency, a simple difference, normalized by the number of samples, between the two signals offers an incomplete picture of how well these two signals correspond:

$$E = \frac{1}{N_x \cdot N_f} \sum_{x=1}^{N_x} \sum_{f=1}^{N_f} \left| H_m^{x,f} - H_d^{x,f} \right|. \tag{3.1}$$

In these equations it is assumed that H denotes the magnetic field in the $\hat{z}$ direction, corresponding to what is measured by the GEM-3 instrument. To demonstrate the inaccuracy of the preceeding objective function, one can imagine obtaining measurements of a UXO at two elevation planes. The upper elevation plane would measure weaker signals. Differences between weaker signals would be smaller than differences between stronger signals. Signals differences arising from the stronger signal samplings will dominate the calculated error. Therefore, the final calculated error would be incorrectly biased towards values from the lower plane [96]. To prevent this bias, the difference must be point-wise normalized by the magnitude of the data such that the difference at any sample point becomes a percentage of the signal at the same sample point as shown in Equation 3.2:

$$E = \frac{1}{N_x \cdot N_f} \sum_{x=1}^{N_x} \sum_{f=1}^{N_f} \frac{\left| H_m^{x,f} - H_d^{x,f} \right|}{|H_d^{x,f}|}. \tag{3.2}$$

This objective function would prevent biasing when determining the overall error. But this measure also produces some undesirable results by permitting very small outlying, noisy data points to contribute equally to the error. Therefore, one must specify a lower bound on the normalizing value such that the effect of very small differences arising from signals weaker than δ will be negated as shown in Equation 3.3:

$$E = \frac{1}{N_x \cdot N_f} \sum_{x=1}^{N_x} \sum_{f=1}^{N_f} \frac{\left| H_m^{x,f} - H_d^{x,f} \right|}{max(\delta, |H_d^{x,f}|)}. \tag{3.3}$$

This measure can be used as universal benchmark for all signals which may vary in strength and sample size, producing an appropriately weighted percentage error. A form of

this error function has also been previously used [18]. For the results shown in this thesis, δ is equal to 0.08 times the maximum value of $|H_d^{x,f}|$.

3.5 Methodology

3.5.1 Selection of Forward Model

As stated earlier, DE requires multiple, successive evaluations of the forward model. Therefore, it is advantageous to select the fastest model of acceptable accuracy. The fundamental mode model and the spheroidal mode model are both comparably fast given that both compute responses as a sum of a finite number of modes derived from stored values. However, the fundamental mode model is implemented in FORTRAN while the spheroidal mode model is written in Matlab. This difference is critical due to the lack of Matlab-based MPI capabilities at the Army Research Laboratory High Performance Computing facility which provided the parallelized processors. Therefore, the fundamental mode model is used as the forward model in this portion of the inversion study.

It should be noted that the fundamental mode model was derived from GEM-3 measurements of actual UXO. The values of the magnetic charges which characterize the response of an object in this model reflect the units by which the GEM-3 reports all measurement data. Any prediction made by the fundamental mode model has the same units as all measurements outputted by the GEM-3. Therefore, the application of the scaling factor derived in the previous chapter to ensure consistency between forward model and measurements is not

needed. The scaling factor, however, must be applied whenever a wholly analytical forward model, such as the spheroid model, is in use. This scenario corresponds to the research into UXO classification described in the next chapter.

3.5.2 Implementation of Differential Evolution

Because the FORTRAN source code for the fundamental mode model is available, DE is written into this code to provide full integration and therefore eliminate any associated communication latency which would contribute to a slower performance. The appropriate MPI commands are then added into the code to provide the parallelization effect as described in Section 3.3.1

3.5.3 Model Setup

The fundamental mode model [79] was previously shown to provide to provides predictions for specific UXO types. Therefore, it may be more accurate to refer to the fundamental model as a library of specific UXO models. Of the available UXO types within the model, four are selected to form this library and to be used as part of the optimization scheme. These four UXO are shown in Figure 3-4. In each test case, described in the subsequent sections, either only one or none of the library members correctly corresponds to the unknown target. For each UXO type within the fundamental mode model, only the orientation and position of the object is needed as input. Therefore, for each object in the library, DE will recover the (x, y, z) position and (θ, ϕ) orientation that will create the best match to the signal from

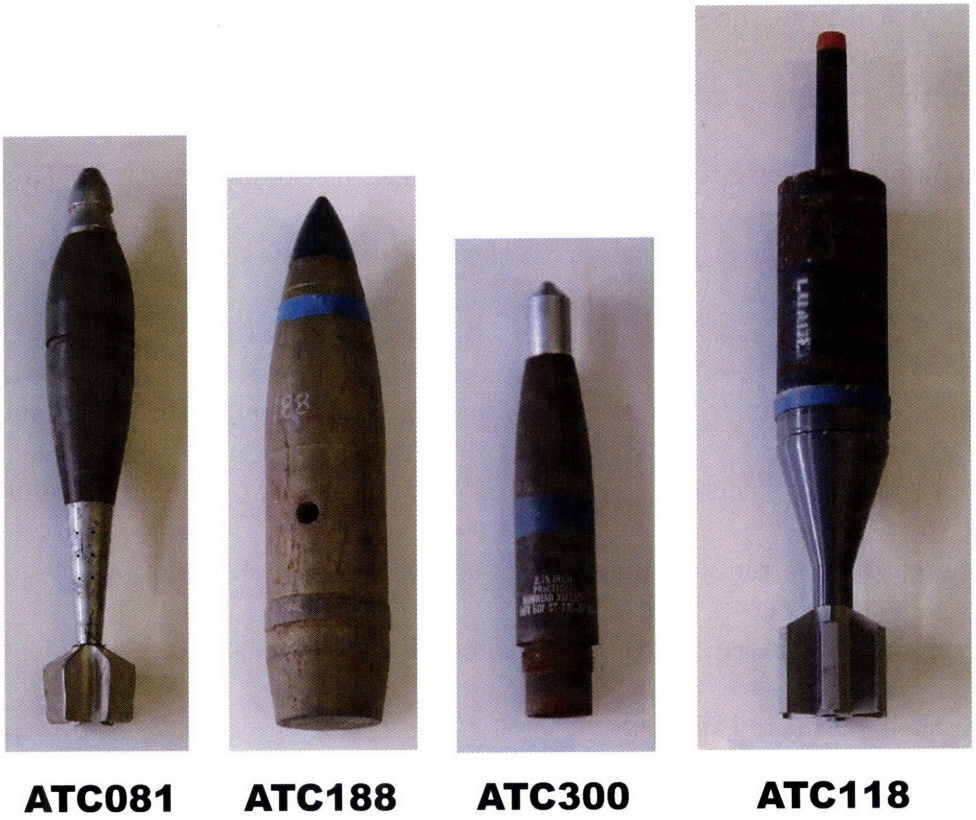

Figure 3-4: A four member library of UXO models is used to test the DE optimization algorithm. The relative sizes of the pictures are to scale. From left to right, these items are ATC081, ATC188. ATC300, and ATC118. Their lengths, from left to right are roughly 51 cm, 48 cm, 41 cm, and 64 cm. Photographs are courtesy of CRREL.

an unknown target. The library object which has the closest match is then taken to be the identity of the unknown object.

3.5.4 Differential Evolution Setup

Given that the search parameters are (x, y, z) and (θ, ϕ) for each library member, each candidate in the population is a vector of length 5. References state a population size should be roughly 10 or more times the number of search parameters [62]. In the later part of this chapter, the forward model will be extended to include soil half space effects. Soil

permeability μ will form the sixth input parameter into the model. Therefore, for all work presented in this chapter, a population size of 60 is used.

DE also requires the user to specify the bounds of each search parameters. The inclination parameter θ which specifies the angle from the positive z axis to the $x-y$ plane is allowed to vary from 0 to π rad. The rotation angle, ϕ, varies from 0 to 2π rad. In the simulation, x and y span from -0.3 m to 0.3 m. The sensor is located on the $z = 0$ plane or above. The depth of the target's center, z, spans from -0.1 m to -0.7 m. Candidate solutions whose parameters create a non-physical possibility, such as the UXO intersecting the measurement plane, are explicitly rejected. These parameters are first initialized randomly with values drawn from their permitted ranges.

The value of the "F" parameter shown in Figure 3-3 is the amplification factor. A larger F indicates a more aggressive change and produces a faster but less robust solver. A smaller F indicates a more gradual change producing a slower but more robust solver [62]. Through trial and error, it was found that the use of $F = 0.4$ provides the most consistent, correct convergence. Some literature suggest using crossover and mutation,"M" as shown in Figure 3-3, to complement the differential change [62]. While this study implemented these additions, no appreciable difference was observed when these features were added to DE. Therefore, all results shown in this thesis were created without the use of crossover and mutation.

3.5.5 MPI Setup

The population size in use determines the number of processors MPI divides the work across. Each processor is assigned to one population member so 60 processors are used in parallel. In addition, one more processor must be used for the controlling and aggregating process.

Since DE is implemented in FORTRAN and integrated into the source code of the fundamental mode model, the MPI FORTRAN commands are likewise inserted into this code.

3.6 Inversion Results

The following inversion results present four basic cases, each progressively more difficult:

1. Inversion for a target in freespace
2. Inversion for a buried target
3. Inversion for a target underneath clutter in freespace
4. Inversion for a buried target underneath clutter

In each case, models are first used to produce synthetic data. This synthetic data is then used by the inversion algorithm to determine the identity of the target and ascertain any limitations on accuracy of the inversion. After the synthetic data study, corresponding measurements of the target are taken and processed by the inversion algorithm in a likewise manner.

Table 3.1: Differential evolution optimizes outputs of the forward model to measurements. In doing so, it recovers the position and the orientation with a high degree of accuracy.

	x (m)	y (m)	z (m)	θ (rad)	ϕ (rad)
Real Value	0.100	0.100	-0.350	$3\pi/4$	$\pi/2$
Optimized Value	0.107	0.0991	-0.351	2.37	1.94

3.6.1 Inversion of Objects in Freespace

As the first test for a target in freespace, only synthetic data is used. The model's output is matched with outputs previously generated. This test allows the verification of the capability of the DE algorithm and the selected objective function. In all tests, the measurements and calculated responses were on a 7 by 7 grid of 10 cm spacing. For synthetic data, the plane was 0.35 m above the center of the object. The synthetic data are generated by the fundamental mode model with input parameters $x = 0.1$ m, $y = 0.1$ m, $z = 0.35$ m, $\theta = 3\pi/4$ rad, and $\phi = \pi/2$ rad.

3.6.1.1 Inversion of Synthetic Data for a Single Object

For this test, the DE algorithm uses 50 members in the population and runs for 100 generations. Shown in Table 3.1 are the true and recovered position and orientation values for object ATC188. The recovered position deviates roughly 1 cm away from the true position. Given that this object is more than half a meter in length, this deviation is comparatively small.

One can also examine the convergence of the DE algorithm through successive generations. Shown in Figure 3-5 is the lowest objective function value within each generation.

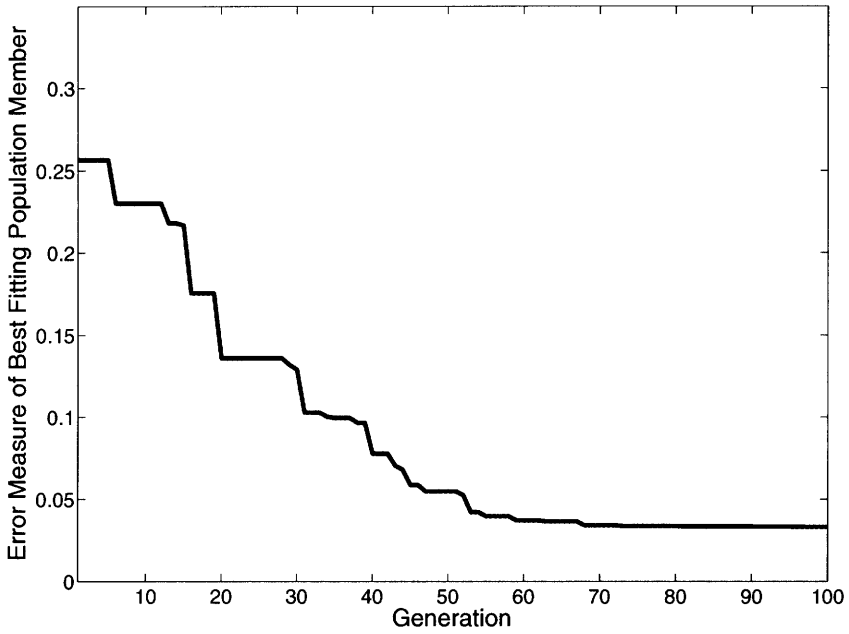

Figure 3-5: Convergence of the DE algorithm is shown by the fitness measure of the best fitting population member. Here F equals 0.4 and produces very low error.

Past 60 or so generations, this value shows convergence.

3.6.1.2 Comparison of F values within DE

The F value of 0.4 used in the previous example provides the most suitable balance between correct convergence and speed. A faster convergence would mean fewer generations and thus faster running times. However, increasing the F value can lead to improper convergence where the optimized (x, y, z, θ, ϕ) values are much less accurate. This inaccuracy and improper convergence can be shown by examining objective function as shown in Figure 3-6. Here, $F = 0.7$. While DE converges rapidly, it converges on a solution which has a much higher error than that created when $F = 0.4$ as shown in Figure 3-5.

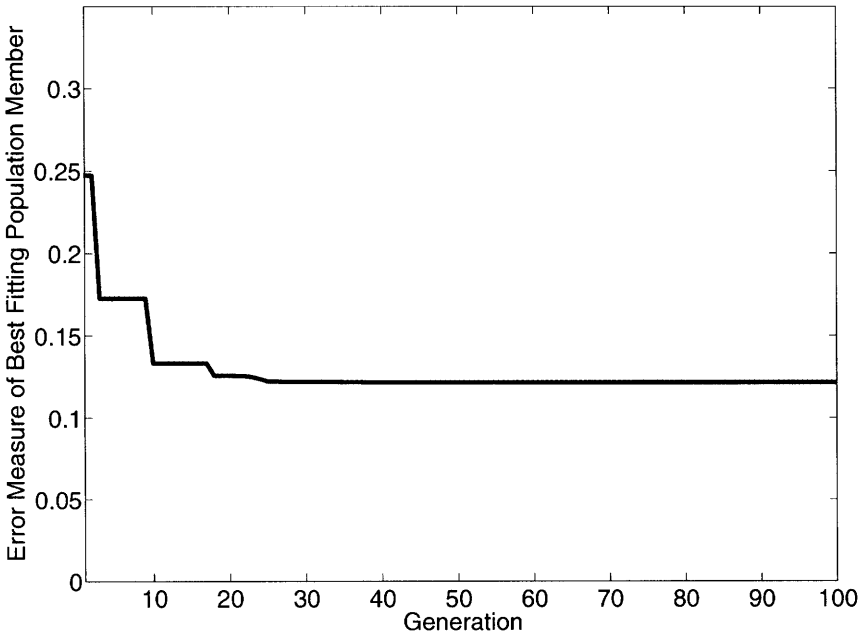

Figure 3-6: Convergence of the DE algorithm is shown by the fitness measure of the best fitting population member. Here F equals 0.7 and produces higher error although the process converges more quickly. This analysis demonstrates that lower values of F are needed for correct optimization.

Library object

Data from synthetic target	ATC081	ATC188	ATC300	ATC118
ATC081	**0.07**	0.22	0.20	0.22
ATC188	0.19	**0.03**	0.21	0.23
ATC300	0.21	0.21	**0.09**	0.24
ATC118	0.23	0.21	0.25	**0.03**

Figure 3-7: The normalized root mean square measure error when testing the DE optimization algorithm with synthetic data. The low error values on the diagonal correspond to good matches.

3.6.1.3 Optimization for Library Members

The above analysis can be extended to a large range of targets. First, the fundamental mode forward model generates responses for the four members of the library. Using these modeled responses, DE recovers the orientation and location of each member of the library that will produce the best match to the data. In addition to confirming the applicability of DE and the selected objective function, this test will also specify the lower bound on error. Any error will be inherent to the DE method and will not be due to any inaccuracy of the forward model or measurement noise. Shown in Table 3-7 are objective function measure of error. As stated earlier, this error can be thought of as a percentage of the mean of the overall response. The rows correspond to data generated from the model for each particular UXO. The columns correspond to the candidates in the library. The diagonal values correspond to the correct match between object producing the synthetic data and the library member. Therefore, the low error values on the diagonal are the lowest in their respective row and demonstrate that identification of UXO is achievable with DE.

3.6.1.4 Inversion Using Measured Data

As a first step in using real data, DE is used to match measurements of a known object with its corresponding model. Measurements are taken of object ATC188 in freespace on a 7 by 7 grid with 10 cm spacing. The measurement plane is 15 cm above the nearest point in the object. The object is roughly at the center of the grid and has a θ value of about $\pi/2$ rad. Given the impreciseness of measuring the UXO position, The object's exact position and orientation are unknown and must be retrieved as part of the inversion process. Therefore, producing a table analogous to Table 3.1 would be misleading. One can show, however, the goodness of fit between the output of the optimized forward model for ATC188 and measured data as shown in Figure 3-8. This match produces an error of 0.08 as measured by the objective function.

The next logical step is to extend the inversion to a wider range of objects and optimize using the four member library. Measurements were taken of various objects, some corresponding to the four library members and others which were artificially constructed large clutter objects as shown in Figure 3-9.

The relative error shown in Figure 3-10 are the result of a "blind" optimization test. The researcher was unaware of the true identity of any of the test objects until after these errors scores were obtained.

The red colored entries in the table of Figure 3-10 represent the error between measured object and optimized library member. Since each red entry is the lowest in their respective rows, the DE algorithm has correctly determined the identity of each measured UXO. For the

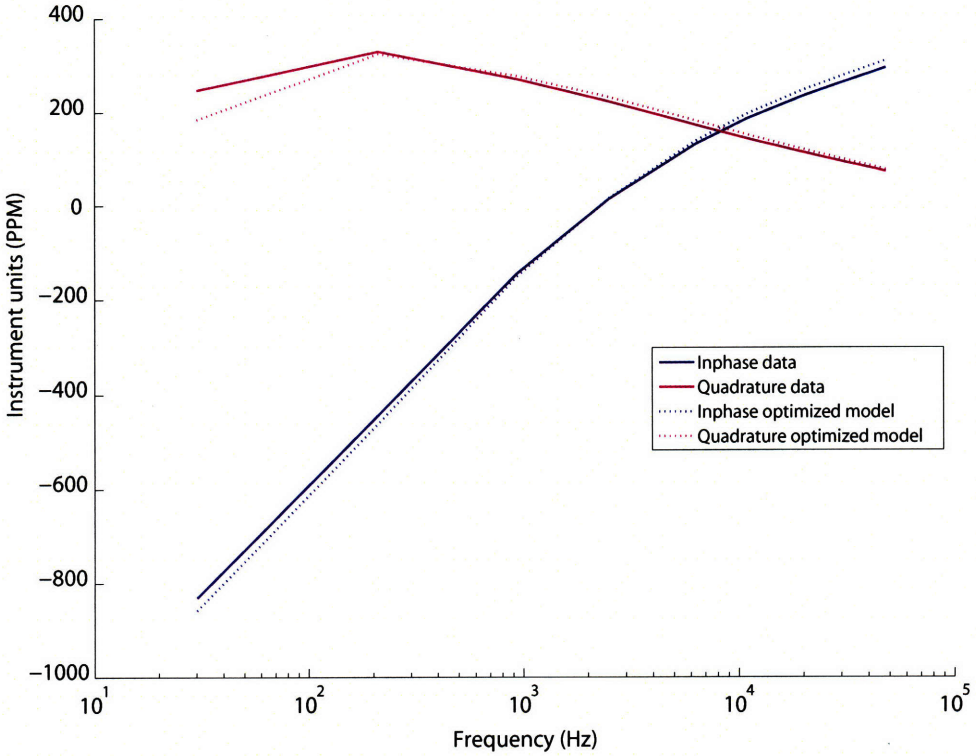

Figure 3-8: Differential evolution optimizes outputs of the forward model to measurements. In doing so, it can match the EMI signal with good accuracy.

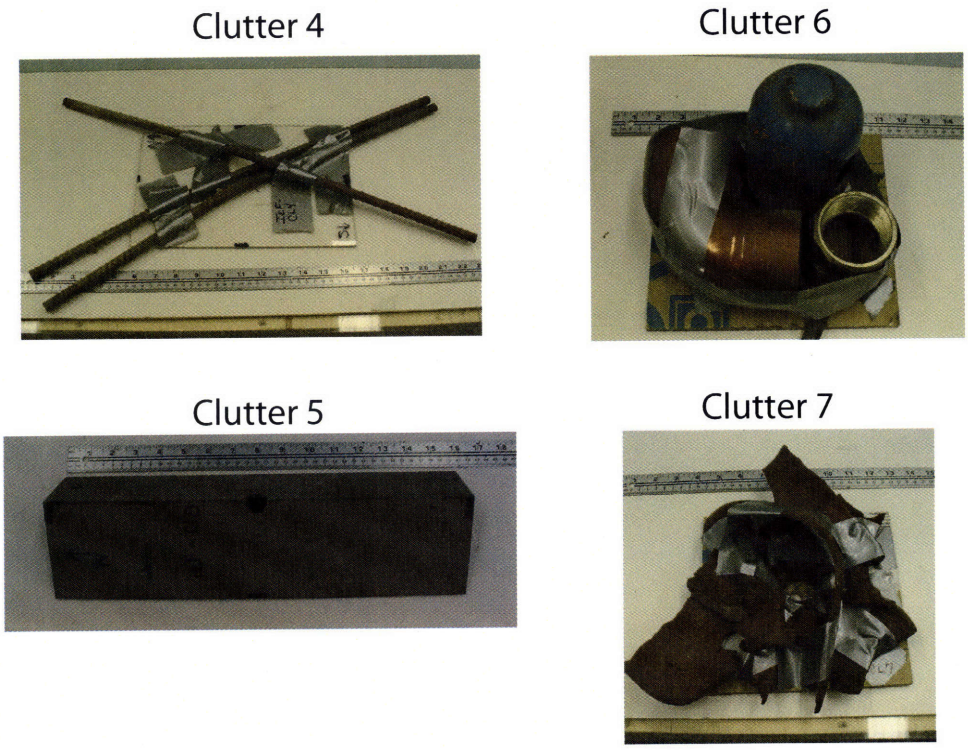

Figure 3-9: Measurements were taken of these four discrete clutter items and used to test the DE optimization algorithm. Photographs courtesy of CRREL.

Library object

Measured object	ATC081	ATC188	ATC300	ATC118
ATC118	0.23	0.27	0.29	**0.11**
Clutter object 4	0.29	0.26	0.23	0.25
Clutter object 5	0.21	0.20	0.23	0.20
ATC188	0.18	**0.08**	0.22	0.21
ATC300	0.21	0.20	**0.10**	0.23
Clutter object 6	0.18	0.18	0.24	0.21
Clutter object 7	0.27	0.27	0.21	0.25
ATC081	**0.12**	0.21	0.24	0.19
ATC118	0.21	0.23	0.25	**0.13**

Figure 3-10: Relative error of the best matches for a four member library. The lowest error is created by the correct object.

clutter items, the errors for all library members are relatively high. The lack of a significantly low error in each row can be used to determine that the unknown object is not a member of the library. If the library encompasses all UXO types that are likely to be present, the lack of a good match for an unknown object can be used to determine that the object is likely a piece of clutter.

3.6.2 Effect of Soil in Differential Evolution Inversion

The previous DE inversion results are for objects measured in a laboratory environment where free space is a good approximation for the background medium. Inversion of a UXO buried in soil is considerably more difficult due to the environmental noise. And as shown previously, a halfspace will create an offset in the Inphase portion of the EMI response which must be taken into account during the inversion process.

3.6.2.1 Accounting for Soil Offset

Accounting for soil offset within the inversion process may be done in two ways. The first method involves removing the effect of the soil offset from the data prior to inversion. This may be done by taking measurements of nearby soil that do not contain UXO targets and then subtracting that data from the measurements of the buried UXO. This technique, however, requires access to "uncontaminated" soil that has the same material properties as the soil containing UXO. Furthermore, the unevenness of the surface of the soil will create varying distances between sensor and the surface. In measurements this variation will manifest itself as noise. Therefore, a smooth soil surface is desired in all measurement.

While these conditions can be reproduced in controlled environments, the same cannot be said of all real UXO recovery scenarios.

The second method to account for the present of soil is to invert for the soil properties within the overall UXO inversion scheme. Much like how DE recovers an object's position and orientation in the optimization process, DE can also recover a soil's permeability value. A halfspace response can be added to the fundamental mode forward model. Given known transmitter characteristics and elevation, this halfspace response can be determined by a single μ parameter as shown in Chapter 2.3. Therefore, as part of the optimization process, μ must be explicitly recovered along with (x, y, z) and (θ, ϕ).

For the analysis of synthetic data created by modeling UXO in permeable backgrounds, the second method to account for soil is applied. The analysis of measurements of real buried UXO utilizes the first technique of subtracting the background response from the UXO measurements as discussed in Section 3.6.2.3.

3.6.2.2 Inverting Synthetic Data with Modeled Permeable Soil Response

A buried UXO's EMI response is modeled as a superposition of a permeable halfspace response on the response of the UXO in freespace as calculated by the fundamental mode model. This approximation was shown to be valid for realistic soil permeability values in Chapter 2.3. Therefore a forward model can be constructed for the response of a buried UXO in this manner.

This same model is also then used within the DE inversion algorithm by extending the search to include an unknown soil permeability value μ. For DE, this can be done by having

Data from synthetic target with permeable soil

	Library object: ATC081	ATC188	ATC300	ATC118
ATC081	**0.12**	0.26	0.23	0.27
ATC188	0.22	**0.08**	0.24	0.26
ATC300	0.23	0.24	**0.11**	0.26
ATC118	0.24	0.24	0.27	**0.07**

Figure 3-11: Table of error for synthetic data with permeable halfspace offset.

each population member include one more variable to specify the soil permeability.

Given a known sensor elevation, only the value of soil μ governs the contribution of the soil to the modeled response. Therefore, 6 parameters must be recovered by DE: (x, y, z), (θ, ϕ), and soil μ. Following the guidelines stated earlier, a population size of 60 is used. Furthermore, the algorithm is now allowed to run for 120 generations. To test the performance, a simulation analogous to the one specified in Section 3.6.1 is conducted. First the synthetic UXO response data is overlaid with the response of a halfspace with some unknown but reasonable permeability value. Then this synthetic data is used by DE to retrieve (x, y, z), (θ, ϕ), and soil μ for all library members as shown in Figure 3-11. As earlier, the corresponding library member in each row is correctly identified because it produces the lowest error. Errors for the incorrect library members are at least roughly double the error corresponding to the correct target.

3.6.2.3 Inverting Measurements Taken from Objects Buried in Soil

Shown in Figure 3-12 are the optimization results for measurements taken of an ATC081 buried at three different depths: 5, 10, and 15 cm. The target is roughly oriented and positioned at $\theta = \pi/4$ rad, $\phi = 0$ rad, and $x = y = 0$ m in all measurements. Depth

Library object

Measured object	ATC081	ATC188	ATC300	ATC118
ATC081 buried under 15cm soil	**0.24**	0.25	0.27	0.28
ATC081 buried under 10cm soil	**0.19**	0.25	0.27	0.29
ATC081 buried under 5cm soil	**0.14**	0.24	0.28	0.26

Figure 3-12: Relative error of the best matches for a four member library. The measurements were taken of a buried UXO target. The lowest error is created by the correct library member for measurements of the object at depths of 10 and 5 cm. Depth is measured from the surface of the soil to the nearest point on the target. When the object is buried at a depth of 15 cm, however, the error values are roughly equal amongst all the library members, indicating that DE has difficulty identifying more deeply buried objects.

is measured from the surface of the halfspace to the nearest point on the target. The measurement grid is 7 by 7 with 10 cm spacing and at a 11.25 cm elevation above the soil surface.

The data clearly shows that DE is able to find better matches for objects buried at more shallow depths. The trend can also be graphically depicted as shown in Figure 3-13. This phenomenon can be explained by the lower SNR for deeply buried objects: as shown in a previous chapter, the soil response is an image of the sensor. Therefore, the magnitude of the soil response will remain relatively constant for all measurements at the same sensor elevation. However, if the target is buried more deeply, its measurable secondary response becomes much weaker due to the increased distance to the sensor. The response from the target decays roughly in proportion to $\frac{1}{r^6}$ where r is the distance between target and sensor. This loss represents the $\frac{1}{r^3}$ loss between transmitter and target and another $\frac{1}{r^3}$ loss between target and receiver.

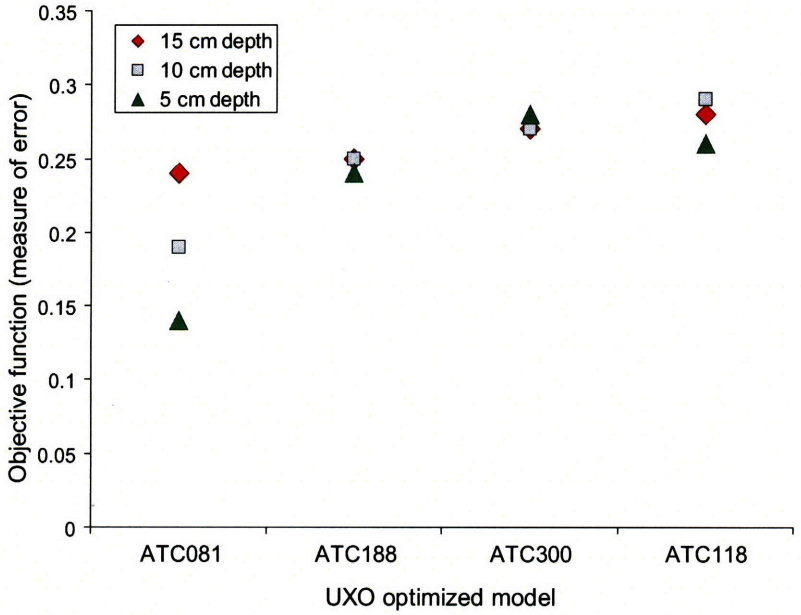

Figure 3-13: Graphical interpretation for the relative error of the best matches for a four member library. The measurements were taken of a buried UXO target. The lowest error is created by the correct library member for measurements of the object at depths of 10 and 5 cm. Depth is measured from the surface of the soil to the nearest point on the target. When the object is buried at a depth of 15 cm, however, the error values are roughly equal amongst all the library members, indicating that DE has difficulty identifying more deeply buried objects.

3.6.3 Effect of Clutter on Differential Evolution Inversion

Another large contributor to noise is the presence of very small diffuse metal clutter objects, often very near the surface of the soil. While these clutter items are much smaller than the large discrete clutter depicted in Figure 3-9, small diffuse clutter may still create a very strong EMI responses when the sensor passes above. Therefore, the impact of diffuse clutter pieces on the overall EMI response of buried UXO must be taken into account. This study first examines the effect of modeled small clutter in the inversion of synthetic data before proceeding to measurements of UXO overlaid with clutter.

3.6.3.1 Synthetic Clutter Estimates

Small pieces of clutter can be modeled as dipoles and their combined response can be superimposed onto a UXO forward model prediction of the secondary field. This superposition creates a model for a UXO obscured by clutter. The modeled clutter is comprised of 20 dipoles, characterized by a magnetic polarizability matrix of a metal sphere in a uniform field. These dipoles are randomly dispersed over an area of 0.6 by 0.6 m and a depth of up to 0.5 m, corresponding to the allowable range for the position of the modeled UXO target. The distribution of the locations for the spheres is uniform random over this volume. The spheres range in size from 0.5 cm to 2 cm in diameter. Their diameter is randomly selected from this range with a uniform distribution. These spheres have material properties equal to either typical steel ($\mu_r = 100$ with $\sigma = 2 \times 10^6$ S/m) or typical aluminum ($\mu_r = 1$ with $\sigma = 2 \times 10^7$ S/m), randomly selected with equal probability. Monte Carlo simulations with

Data from synthetic target with modeled clutter	Library object			
	ATC081	**ATC188**	**ATC300**	**ATC118**
ATC081	**0.15**	0.26	0.26	0.29
ATC188	0.24	**0.12**	0.25	0.28
ATC300	0.26	0.25	**0.13**	0.28
ATC118	0.25	0.24	0.27	**0.12**

Figure 3-14: The objective function computer error when testing the DE optimization algorithm with synthetic data. The low error values on the diagonal correspond to good matches.

10 trials suggest the presence of these spheres creates a level of noise that is comparable to about 19dB SNR. For the modeled volume of 0.18 m^3, a total of about 35 cm^3 is comprised of metal from these small spheres.

Using this model of a UXO obscured by clutter, synthetic data can be created and used to test the DE optimization in the same manner as described in Section 3.6.1.3. It should be noted that while the synthetic data is generated by the model that includes clutter, within the DE algorithm the forward model does not include any clutter or soil modeling.

The 5 parameter DE optimization is used to recover (x, y, z, θ, ϕ) for each library member. DE matches the forward models to the noise corrupted signatures of the targets, identifying the best matching object amongst the candidates in the library as described in Section 3.6.1. This inversion uses a 50 member population, running for 100 generations. As shown in Figure 3-14, the correct library member still produces the lowest error in each row. However, as one might expect, the errors are larger than in previous examples where no clutter was present in the synthetic data.

3.6.3.2 Real Clutter Measurements

EMI measurements are taken of UXO in freespace overlaid by a surface of small disperse metallic clutter pieces as shown in Figure 3-15. This mat shows the "full clutter" scenario with about 50 cm^3 in volume of clutter. Measurements were also obtained where half this volume of clutter obscured the target UXO. Information about the total mass of these clutter items is unavailable to the author.

DE optimizes the fundamental mode model of the four candidates in the library to match these noisy measurements. This optimization is repeated for varying amounts of clutter. The inversion is successful for cluttered measurements which had signal-to-noise ratios up to 17.5 dB. This result is shown in the second row of Figure 3-16 where the correct library member produces the smallest error. However, when a denser collection of clutter is overlaid above the target, an SNR of 11.2 dB results and DE is unable to distinguish the correct UXO from the other members of the library. This is shown in the third row of the same figure where the error produced by the correct library member is indistinguishable from the others. The relative differences can be interpreted more easily when seen in a graphical form as shown in Figure 3-17.

3.6.4 Combined Effect of Clutter and Soil on UXO Identification

The ultimate test of any UXO inversion system is to identify a target buried in magnetically responsive soil that is also obscured by clutter. To this end, one must investigate the effect of both soil and clutter. Once again, a synthetic test precedes the analysis of measured data.

Figure 3-15: A mat of diffuse clutter pieces at a concentration deemed very significant for UXO contaminated land. This mat corresponds to the "full clutter" scenario. Photograph courtesy of CRREL.

Measured object	Library object: ATC081	ATC188	ATC300	ATC118
ATC118 alone	0.25	0.26	0.28	**0.12**
ATC118 + half clutter	0.25	0.27	0.31	**0.15**
ATC118 + full clutter	0.27	0.29	0.30	**0.27**

Figure 3-16: Relative error of the best matches for a four member library. The measurements were taken of a UXO target obscured by a layer of clutter. The lowest error is created by the correct library member in the "no clutter" and the "half clutter" scenarios.

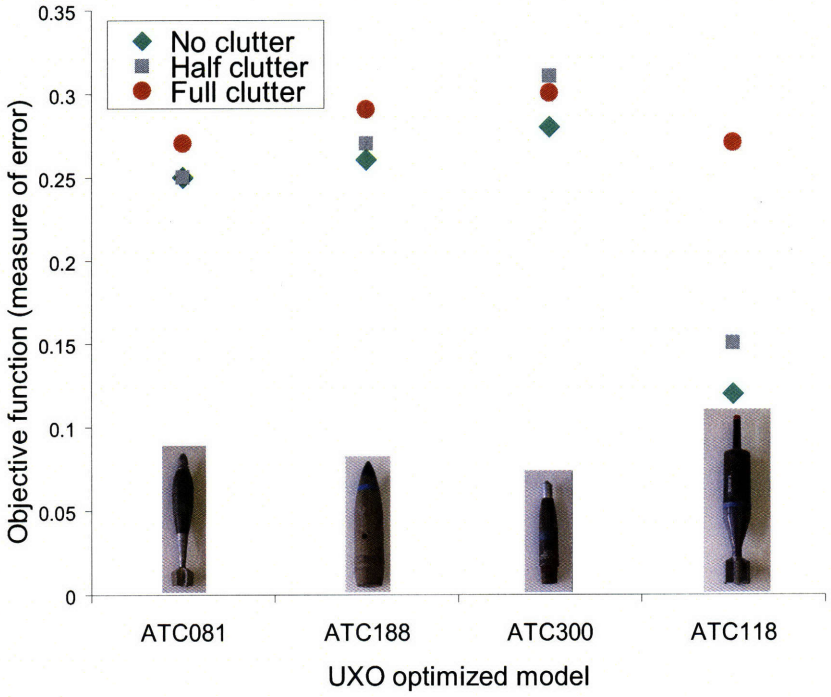

Figure 3-17: Graphical interpretation for the relative error of the best matches for a four member library. The measurements were taken of a UXO target obscured by a layer of clutter. The lowest error is created by the correct library member in the "no clutter" and the "half clutter" scenarios.

Data from synthetic target with permeable Soil and modeled clutter

	Library object			
	ATC081	**ATC188**	**ATC300**	**ATC118**
ATC081	**0.18**	0.27	0.27	0.27
ATC188	0.28	**0.19**	0.25	0.28
ATC300	0.27	0.25	**0.22**	0.26
ATC118	0.29	0.26	0.30	**0.18**

Figure 3-18: Table of error for synthetic data generated from model of buried UXO with clutter.

3.6.4.1 Modeled Response of Buried UXO with Clutter

A model of buried UXO obscured by clutter can be created by superimposing both a permeable halfspace response and the response of a collection of small metal spheres onto the fundamental mode model for the response of the target of interest. These small spheres are as described in Section 3.6.3.1.

There are now two distinct sources of noise in the synthetic data: soil and clutter. The DE inversion then attempts to match this noisy signal by optimizing the sensor-target configurations of each of the four candidates in the UXO library.

While the synthetic data is generated by a UXO model which includes the effect of permeable soil and diffuse clutter, the forward model used within the DE optimization algorithm includes the effect of the permeable soil but not any diffuse clutter. In other words, the inversion scheme is the same as that described in Section 3.6.2.2.

Given the effect of soil permeability, the subsequent need to optimize 6 parameters instead of only 5, and the noise due to the clutter, the match now is less successful than the prior tests as shown in Figure 3-18. While the correct library member provides the lowest error in each row, the margin of difference is much narrower particularly for ATC300.

Figure 3-19: A mat of diffuse clutter pieces at a concentration seen at heavily contaminated UXO sites. Photograph courtesy of CRREL.

3.6.4.2 Measurements of Buried UXO with Clutter

To test DE with real data, measurements were taken of buried UXO overlaid with a sheet of clutter. The sheet of clutter is shown in Figure 3-19. The mass and volume of this clutter sheet is unknown, but it was created by researchers familiar with UXO contaminated sites and is representative of typical clutter concentrations seen there. The buried test objects are ATC118, ATC188, and ATC300. As shown in Figure 3-20, the match is considerably worse. Unlike the previous cases, one cannot always distinguish the correct identity among the members of the library. This suggests the level of noise due to both the clutter and soil is far too strong when compared to the UXO response.

Measured buried target with clutter overlay

Library object

	ATC081	ATC188	ATC300	ATC118
ATC188	0.29	**0.27**	0.27	0.31
ATC300	0.32	0.28	**0.28**	0.30
ATC118	0.29	0.30	0.33	**0.23**

Figure 3-20: Table of error for inversion of buried targets overlaid with a clutter sheet. The higher error values for the correct library members, shown in bold, indicate that DE optimization is unable to identify targets reliably under these conditions.

3.7 Conclusion

While DE is shown to be able to identify an unknown target, it is significantly hampered by two large problems. First, sources of noise due to the soil and clutter significantly reduces the ability of DE to correctly identify objects. The sheets of clutter used in this study are representative of what may typically be found in UXO sites. Therefore, methods of filtering or suppressing the clutter response are needed before DE matching algorithm, as implemented here, can be used as a practical method of inversion.

The second issue is that DE is very slow. The calculations shown here require more than a week on a desktop computer and at least several hours when the algorithm is parallelized and run on multiple processors. Given the current computer power, real time inversion is not possible. However, one may recall that the UXO problem posed earlier was to identify UXO from clutter and thus reduce false alarm rate. This identification process may be reduced to a simple discrimination between general UXO and clutter. Therefore, a development of a much faster inversion method which does this type of binary discrimination is the subject of the next chapter.

Chapter 4

Inversion Through Application of Machine Learning: Classification

4.1 Introduction

While DE inversion in the previous chapter is shown to be capable of recovering the identity of buried targets when given a library of candidates, that technique is hampered by the computational requirements. Despite use of parallelization and access to supercomputers, processing requires at least a few hours. Given current computing limitations, DE is therefore not a suitable method for real time, on-site inversion. While computational power is steadily increasing with time, there is always motivation to obtain a faster solution that may be obtained within the confines of the present computing capability. Furthermore, the DE method requires compiling a library of specific possible objects and has difficulty generalizing for UXO objects not included in the library because the optimization procedure produces

similar levels for goodness of fit between disparate objects. A UXO not in the library would go unrecognized. Therefore, an alternative method to pursue is to discriminate all UXO from clutter generically, as opposed to identifying particular UXO or UXO types. The inversion problem can be considered as a classification problem: given the EMI response of an unknown object, one must classify the object as either a UXO or a piece of clutter.

4.1.1 Previous Work

While general UXO inversion work by other researchers was mentioned in the previous chapter, the work in this chapter is most similar to statistically based classification [17, 52, 81, 94] and pattern recognition [31]. However, the previous work implement discrimination based on features of the EMI response which cannot be proven to be unique properties of the associated target. For example, parameters of an axial dipole response can be used [41], but as shown earlier, the dipole model does a poor job of characterizing heterogeneous objects. The work described in this thesis is unique in that it makes use of B_k^j , the coefficients of the spheroidal response modes. Since B_k^j have been proven to be unique properties of the target [3], they readily lend themselves as inputs into any discrimination algorithm.

4.2 Research Overview

To form such a discriminator, several topics must investigated:

1. **What characteristics distinguish UXO from clutter objects?** The most basic question one can ask is how UXO can be physically distinguished from clutter objects.

To that end, the following section will discuss four basic physical characteristics of UXO not found in typical clutter.

2. **How are these physical characteristics represented in the UXO's EMI responses?** The physical properties of objects dictate their corresponding EMI response. Therefore, it may be possible to find distinguishable traits or features within these EMI responses that relate to the physical nature of the target. Section 4.4 discusses utilizing the B_k^j coefficients as such features.

3. **What is the relationship between these features and the physical characteristics of the object?** If it is possible to derive distinguishable features of EMI responses which relate to the physical nature of the object, then the next objective would be to decipher such a relationship. Section 4.5 discusses how to recover this relationship through example data with the application of machine learning techniques. One particular machine learning method, support vector machines, will be introduced and discussed.

Once the relationship between B_k^j values, characteristics of the target which may be found through the corresponding EMI response, and the physical nature of the targets is known, classification would only require examining the B_k^j values of any new target to determine if the object physically is more similar to UXO or to clutter. As discussed in earlier chapters, B_k^j values may be recovered from any target given enough EMI measurements. Therefore, this method has the potential to classify objects in a real time, on-site process when enough measurement data of the buried target are taken. Therefore, this method has several distinct

advantages over DE inversion and warrants investigation.

4.3 Determining Clutter and UXO Characteristics

To perform discrimination between UXO and clutter, it is necessary to ask what physical characteristics distinguish clutter objects from UXO targets. The earlier discussion on DE inversion included examples with larger clutter objects and sheets of very small diffuse clutter pieces. Large clutter pieces can possibly be mistaken for UXO while small diffuse clutter largely contribute noise to the measured EMI response. Figure 4-1 shows clutter pieces of various sizes that were recovered from UXO sites. Note both the shape and size of these clutter objects. The largest is around 10 cm. The UXO shown in Figure 4-2 is around 80 cm. It is elongated and has a general body of revolution shape. From such inspections, one can decided upon several basic key physical features to distinguish UXO from clutter [98]:

1. Body of Revolution (BOR): UXO are almost always a BOR. Even the presence of fins or other small deviations on a UXO does not affect the response of the object to the extent that one is able to distinguish it from true BOR objects [71]. In contrast, clutter can have any random shape.

2. Size: Field workers involved in UXO cleanup are particularly interested in distinguishing larger objects from relatively smaller clutter items. These clutter items can have a strong EMI response if they are buried at shallow depths which is a common scenario. Since the strength of the object's response is a poor indication of the object's size,

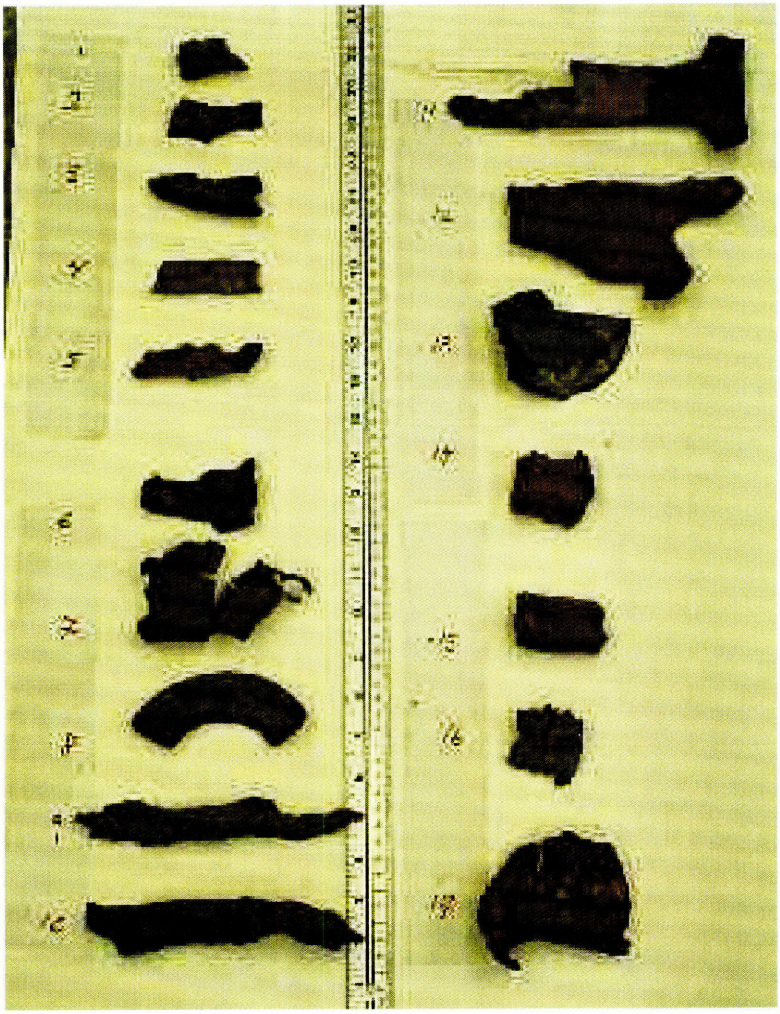

Figure 4-1: Large discrete clutter objects recovered from UXO sites. Photograph courtesy of CRREL.

more sophisticated discrimination processing is necessary to avoid the costly task of digging up these clutter objects.

3. Homogeneity: UXO are usually composed of a number of different materials while clutter, often fragments and casings from exploded ordnances, are often homogeneous.

Realistic obstacles to successful discrimination must be considered when developing any practical classification method. The classification must be general enough to be applied to

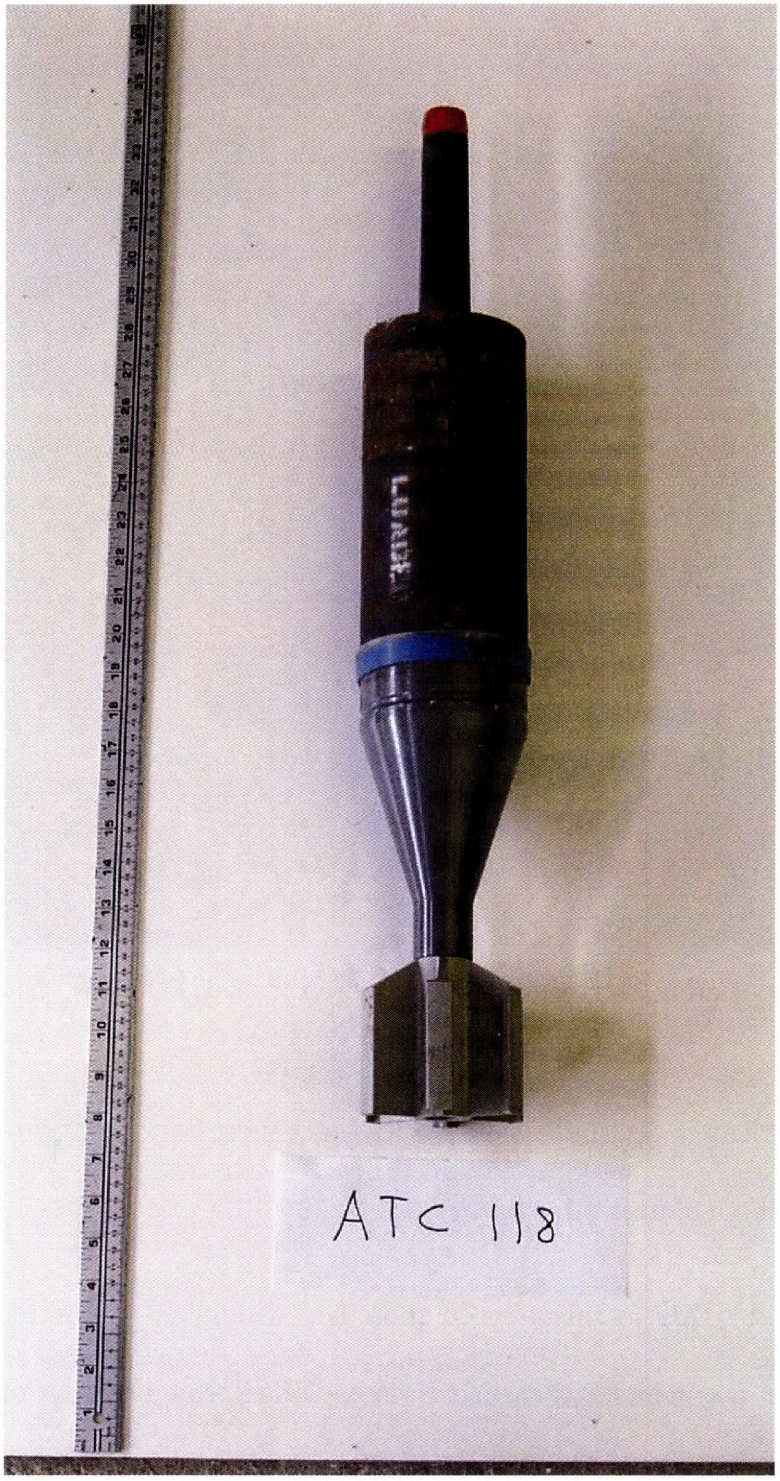

Figure 4-2: Typical UXO object. Photograph courtesy of CRREL.

a wide range of possible objects since there is a substantial range of possible clutter items and UXO. The classification must be robust enough to be minimally affected by sensor and environmental noise. Furthermore, for real time application, the classification must be fast. All of these points are addressed in this research.

4.4 Selection of Feature Vector: Distinguishable Parameters of EMI Responses

While the DE inversion study discussed in previous chapter uses the EMI response of objects directly, these responses are highly dependent on target's orientation, location, and sensor in use. One would like to find features of the EMI response which only relate to the physical nature of the object. These features may offer clues to the object's generic characteristics, such as size, shape, and symmetry, which may strongly indicate whether the object is a UXO or clutter. One such feature came to light as the result of previous work in developing the spheroidal mode forward model within the spheroidal coordinate system. As discussed, within this coordinate system, the excitation and response of a UXO or any other object can be described in terms of scalar spheroidal modes consisting of associated Legendre functions. The spheroidal response modes each have a coefficient B_k^j which correspond to the kth mode of the spheroidal response due to the jth mode of the spheroidal excitation [12]. The B_k^j have been proven to be unique properties of an object in the sense that objects producing different scattered fields must have different B_k^j [12, 18]. For a coordinate system aligned

and centered on the target, B_k^j are completely independent of the excitation, orientation, and location of the object. Thus B_k^j values only depend on the physical properties of the object. Consequently, these B_k^j coefficients, which can be recovered from the measured signal, are appropriate inputs into classification algorithms.

4.4.1 Motivation for the Use of Spheroidal Mode Coefficients

The motivation for the use of B_k^j coefficients rather than parameters of a simpler model, namely the dipole model, stems from the comparison between the spheroidal mode model and the dipole model given in 2.2.2.2. The dipole model is insufficient to model composite objects. Characterizing objects solely by the associated polarizability factors, fitted to the measurement data in a least-squares sense, has no guarantee of uniqueness as shown by [77]. Furthermore, examples in Section 2.2.2.2 show that dipoles poorly characterize heterogeneous objects.

Therefore, this study proceeds with classification using B_k^j parameters. Some measurement configurations and associated data limitations may pose computational problems, limiting the number of modes that one can treat. But since prior work has shown that a significant number of B_k^j can be reliably obtained from noise-corrupted signals [18, 19], the focus here is on analyzing whether good classification is possible when accurate B_k^j are obtained. The relationship between the number of utilized B_k^j values and classification accuracy is also studied. Furthermore, the sensitivity tests will demonstrate the level of accuracy possible when the classification uses B_k^j derived from noisy signals.

4.5 Background on Learning Machines

As stated earlier, determining whether an object is a piece of discrete clutter or a UXO by using the B_k^j coefficients of the object requires an understanding of the relationship between the coefficient values and the physical nature of the object. One can easily hypothesize that this relationship must produce patterns in the B_k^j coefficients of particular objects. However, these patterns may be difficult to recognize by an unaided human. Such pattern recognition problems can be found in many other fields of study from handwriting analysis to face recognition [60, 90]. In many of these applications, features from the data are used to form correct conclusions about the data samples much like how B_k^j is used to classify objects in this study. The ability to form accurate conclusions about complex data using the selected features, however, requires an algorithm or "machine" to recognize or "learn" the relationship between such data and the features.

Machine learning is learning from experience: given features of some object, it is able to generalize the behavior of the system governing the object and then make predictions about the nature of the object. Most often this prediction involves labeling of the data. For example, suppose an object is characterized by features x and has some associated label y. Given some new x' data from a new object, one must infer the appropriate y' label. Supervised machine learning is one subset of general machine learning where examples with correct labels are first studied before predictions are made about new unlabeled examples. More specifically, given a set of l observations, consisting of an input vectors $x_i \in R^n, i = 1, ..., l$ and the associated labels y_i, the supervised learning machine finds the correct mapping

$x \rightarrow y$ for general data. This process to find the mapping is called "training." The initial set of x_i and y_i input vectors are appropriately named the "training data." The performance of a trained machine can then be evaluated with a set of new x_t test data for which the machine must perform the mapping. The correct associated y_t is known but withheld from the machine. The y_t^* that is found through the mapping is then compared to the true y_t to gauge accuracy. A machine is over-trained if it is only able to recognize and produce the correct output for x that are extremely similar to or even exactly like the x_i members of the training data. This scenario creates a machine that inaccurate for noisy data or slightly different input cases. On the other hand, an under-trained machine is simply too general and does not recognize enough of the specific underlying mapping between x and y, leaving it unable to correctly classify test examples. An ideal machine is capable of generalizing and finding the accurate labels for a very broad range of inputs. Once a learning machine is confirmed to be accurate in the aforementioned manner, it may be used to find the labels for new x where the associated y are truly unknown.

Many machine learning techniques have been shown to be highly capable of dealing with complex and large sets of input values. This method of classification using supervised learning has been applied to a wide range of topics such as data mining, finance [58], and diagnosing hereditary cancer using thousands of genes as input x [63]. Given that the UXO classification problem uses B_k^j values at several frequencies, the ability to handle a large number of features describing an object is also highly attractive. However, one might argue the use of complex pattern analysis algorithms is unwarranted if the relationship between

B_k^j and the physical properties of the object is very obvious. As described in the next section, research was done to demonstrate that this relationship is not simple and the use of machine learning is needed.

4.5.1 Motivation for the Use of Machine Learning Techniques

Beyond motivating the use of the B_k^j system, one should also demonstrate that, having obtained a set of B_k^j , the use of sophisticated classification methods like machine learning is necessary. Some information about the physical natural of the unknown target can be directly gleaned by examining the EMI response. For example, a permeable object would produce a strong Inphase response at low frequency while a non-permeable object would not. Therefore, one might believe such apparent patterns might also appear in the B_k^j values of the objects. For example, one might think the overall magnitude of B_k^j coefficients for an object would be related to the object's size. However, this relationship is not strictly true even for simple, homogeneous objects. Such strict correlation between large B_k^j values and large object size only exists for the very simple case of comparing two objects that are exact scaled versions of each other and of the same material. However, this study is most interested in collections of objects of variable shapes and composed of various materials. This degree of freedom and the choice of frequencies of interest will directly affect the B_k^j values under study. For example, Figure 4-3 shows low frequency B_k^j values from a small permeable spheroid and a larger non-permeable spheroid. The smaller spheroid clearly has larger B_k^j values at this frequency. For another example, in Figure 4-4 the objects' elongation is varied but the

material is the same for both. These two objects have the same volume. But one can find a frequency where the B_k^j of one is larger than the B_k^j of the other. In a third example, one can observe the magnitude of the B_k^j coefficient that corresponds to the z direction dipole response for uniform $\hat{z}$ magnetic field excitation over frequency in Figure 4-5 for two objects of the same size but different material. These values can vary quite a bit over frequency and one curve is not consistently greater than the other. And while the patterns in the data shown in the previous figures can be explained with basic known EMI behavior of metallic objects, the point is that these patterns are made much more complex by the simultaneous variability of object size, material, and shape. Therefore, the conclusion is that the B_k^j patterns and magnetic polarizability patterns are too complex to permit size classification by more simple means such as measuring overall B_k^j magnitude. What machine learning provides is the ability to characterize these patterns in a structured framework so that the classification is systematic.

4.5.2 Background on Support Vector Machine and mySVM

The main machine learning algorithm selected for use in this study is Support Vector Machine (SVM). SVM is a linear classifier where each input training vector $\vec{x}$ is a point that is mapped into an n-dimensional space with n being the length of the vector. The example shown in Figure 4-6 only depicts a 2-D space for clarity. The basic objective of an SVM is to find the optimal hyperplane, i.e. a plane in n-dimension space, that correctly separates the points of the two classes as completely as possible. In the example shown, the hyperplane is reduced

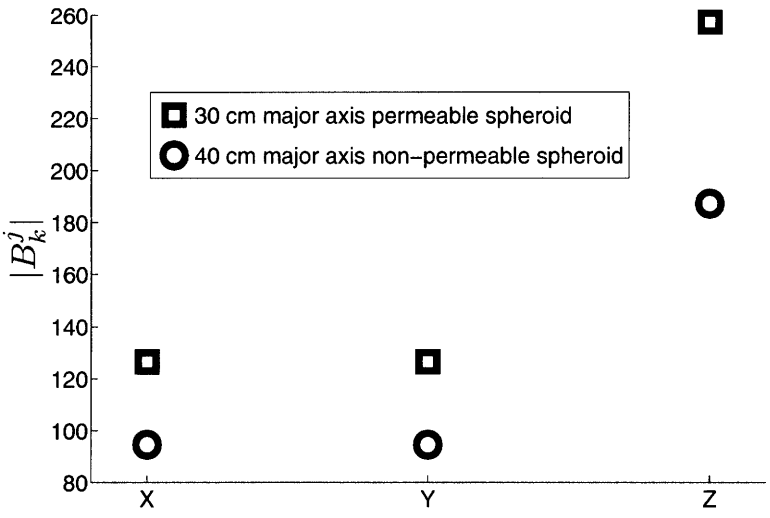

Figure 4-3: $|B_k^j|$ values corresponding to x, y, and z dipoles in response to uniform excitation in each corresponding direction. The smaller spheroid is permeable and the larger spheroid is non-permeable. These three B_k^j values of the smaller spheroid are all greater than the B_k^j values of a large sphere.

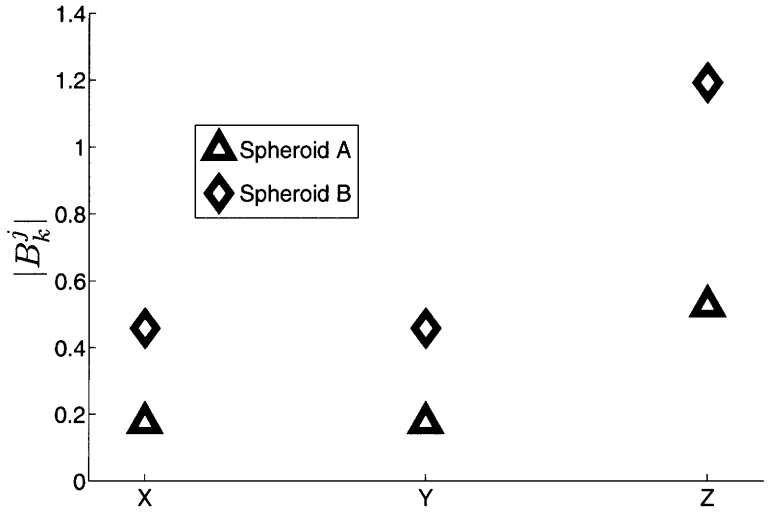

Figure 4-4: $|B_k^j|$ values corresponding to x, y, and z dipoles in response to uniform excitation in each corresponding direction. Spheroid A has an elongation ratio of 2 while spheroid B has a ratio of 1.5, and both objects are of the same material. Even though both objects have the same volume, at 2 kHz it is possible to have dissimilar B_k^j values.

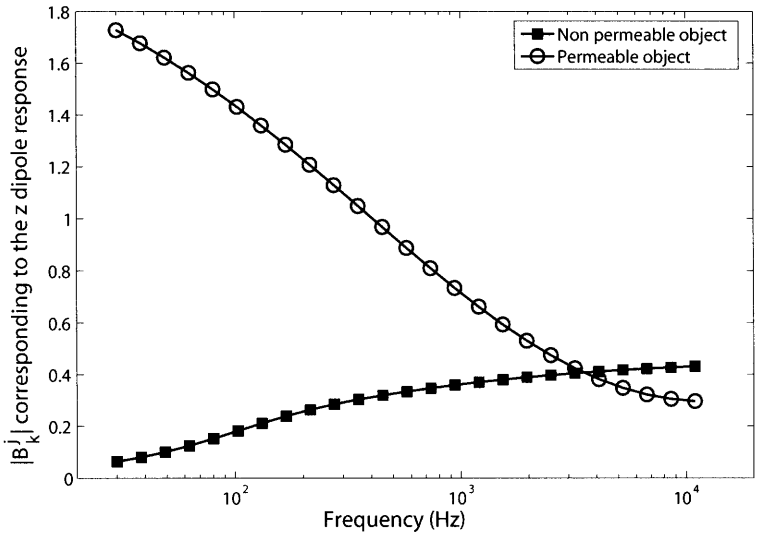

Figure 4-5: $|B_k^j|$ coefficient corresponding to z dipole moment as a function of frequency. These objects are of the same size but are of different materials. They produce z dipole responses that vary across frequency.

to a line. When a test vector is presented, a trained SVM only has to find on which side of the hyperplane the new point falls to determine its class. Therefore, the classification process is normally very fast, making it attractive for the purposes of this study. A constraint is that SVM can normally only do binary classification. However, this constraint is acceptable for this study: the output y is a binary value, being either -1 or +1, and represents the two possible classes of a physical trait that distinguishes UXO from clutter. For example, one can discriminate large objects from small objects. Thus the problem is a binary classification problem. One can then consider each input vector x_i to be the set of B_k^j for an object.

More specifically, suppose there are a total of M training points, indexed by t. Further, for each t data point, the corresponding binary label y_t is +1 or -1. As shown in Figure 4-6, there is a line which correctly divides, or "shatters" in SVM jargon, all the data into two classes. This divider can be defined by a normal vector $\vec{w}$. Therefore, finding the correct

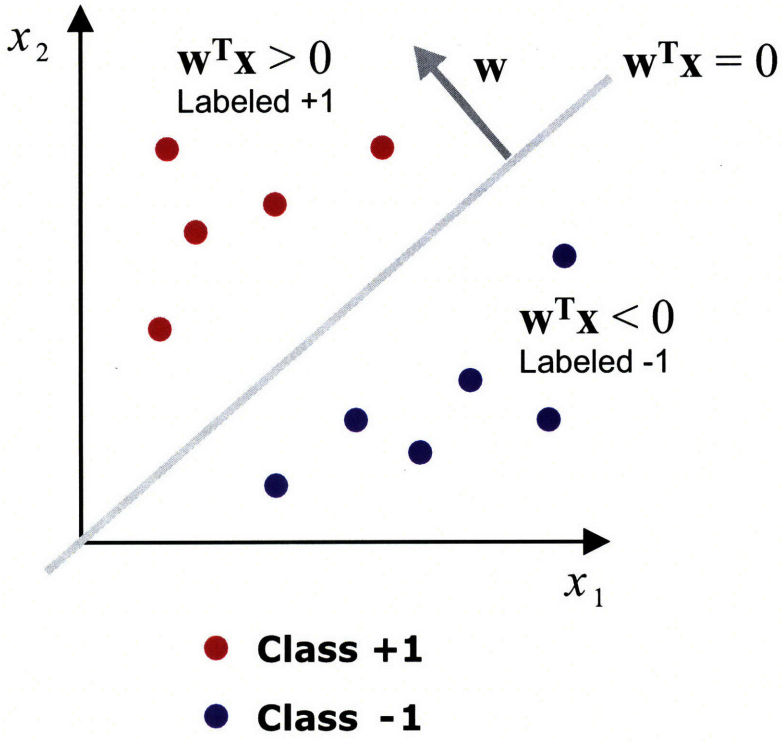

Figure 4-6: A line which correctly divides the data into two classes can be found in this example.

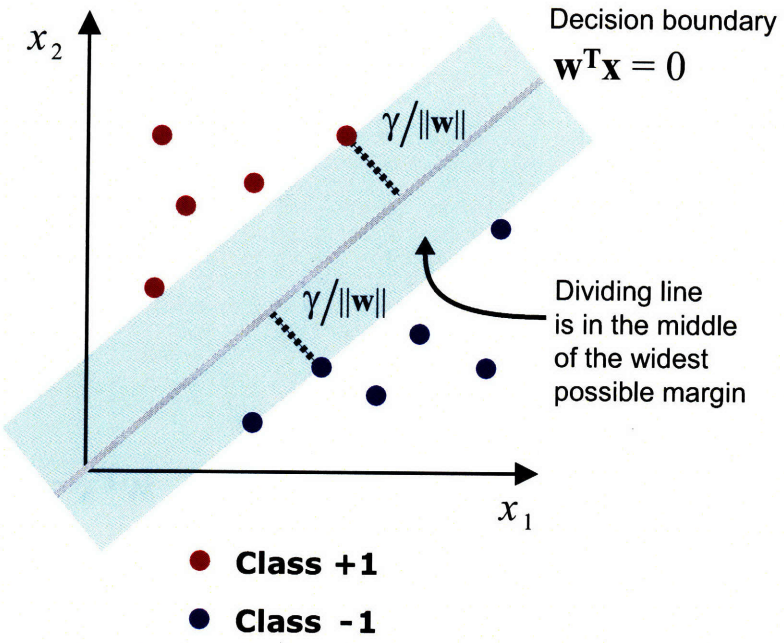

Figure 4-7: The most optimal line which correctly divides the data into two classes is shown in this figure.

divider is equivalent to finding a $\vec{w}$ that satisfies

$$y_t \vec{w}^T \cdot \vec{x_t} > 0 \tag{4.1}$$

for each t. However, one can also see from Figure 4-6 that there are many possible dividing lines and thus many possible solutions for $\vec{w}$. Common sense would lead one to choose the dividing line which has the largest margin possible from the nearest training data points as shown in Figure 4-7. This stipulation is akin requiring the divider to be in the center of the widest possible margin between the two groups.

Since this line will be used to classify new data, using a line much too close to any training data increases the likelihood of misclassification due to a smaller margin of error. Assume, then that there is some $\gamma > 0$ where $y_t \vec{w}^T \vec{x_t} \geq \gamma$ which ensures each example is classified

correctly with a finite margin. The distance between the dividing line and nearest data point can be shown to be $\gamma/\|\vec{w}\|$ [29]. Therefore, to ensure the widest possible margin, one needs to

$$\text{maximize } \gamma/\|\vec{w}\| \text{ subject to } y_t\vec{w}^T \cdot \vec{x_t} > \gamma. \tag{4.2}$$

The equivalent would be

$$\text{minimize } \frac{1}{2}\|\vec{w}\|^2 \text{ subject to } y_t\vec{w}^T \cdot \vec{x_t} > 1. \tag{4.3}$$

This equation is a quadratic programming problem where the objective is a quadratic with linearly constrained parameters. Solving this quadratic programming problem requires an optimization and search mechanism and is implementation dependent. Several quadratic programming solvers are available such as `quadprog` within Matlab.

The previous example is linearly separable and finding a line which correctly divides the data is straight forward. However, shown in Figure 4-8 are two examples of 1-D data where one is linearly separable and the other is not. The divider here is a single point rather than a line. However, this data can be mapped onto 2-D where $x_1 \rightarrow (x_1, x_1^2)$. Now the data is linearly separable as shown in Figure 4-9. In this manner, all non-linearly separable data can be mapped onto a higher dimension where it is linearly separable. The specific mapping used is generally implementation dependent and subject to much research in it of itself [68].

For further explanation of SVM and the mapping selection, the reader is directed to references [29, 85]. This study utilized mySVM, a freely distributed and highly optimized

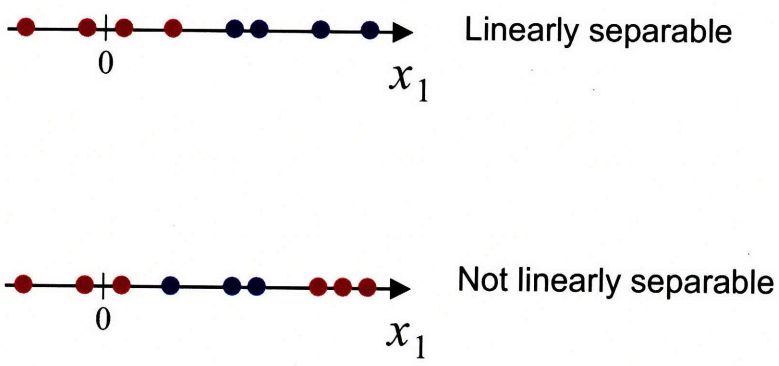

Figure 4-8: Examples of linearly separable and non-separable data in 1-D.

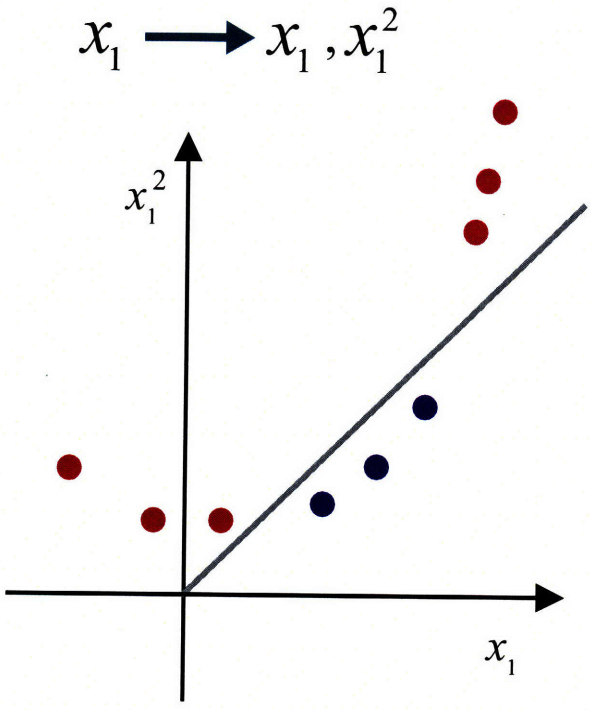

Figure 4-9: A specific mapping 1-D data into 2-D can transform the formerly non-separable data of Figure 4-8 into separable data.

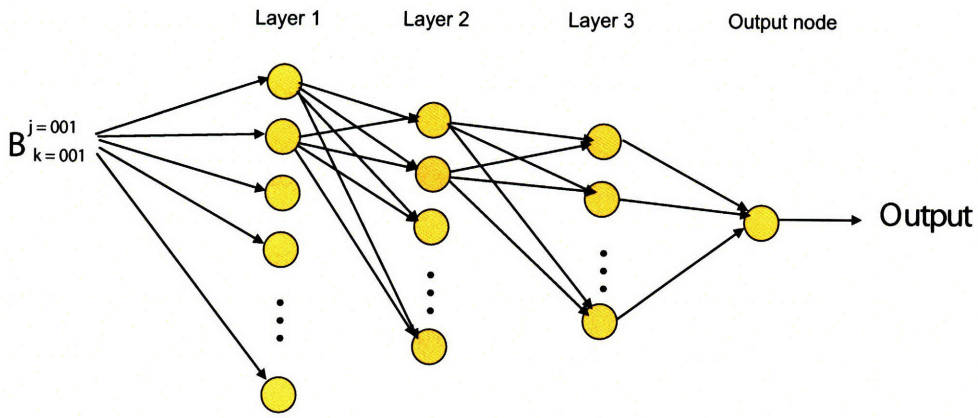

Figure 4-10: Examples of a topology for a three hidden layer neural network.

implementation of SVM based on SVMLight [65, 85]. For the experiments described in this chapter, mySVM operates in its "pattern matching" mode with a radial kernel function. Training of mySVM is very quick, converging in less than a minute for a 1800 member training set on a 3.6 GHz Pentium 4 machine with 3.5 GB of memory. mySVM automatically finds the ideal balance between over training and under training.

4.5.3 Background on Neural Networks

A NN consists of a collection of interconnected processing elements, called "neurons" to collectively perform the $x_i \rightarrow y_i$ transformation. The neurons each have an input and output with a transfer function and a bias. The neurons are organized into layers with outputs of one layer interconnected to the inputs of the subsequent layer. The output of the last layer provides the desired y_i.

Shown in Figure 4-10 is the topology of a neural network with three hidden layers. The node on the farthest right provides the output and is not considered hidden. Each arrow between the NN input and the nodes of the first layer or between different nodes has an

associated weight. Each node also has a bias. The biases and all the weights are first initialized to some random or preset value. To produce the correct output y_i, the difference between the calculated and expected outputs is examined for each member of the training data set. This difference determines how the weights and biases are incrementally adjusted during training to produce the correct mapping function. Like SVM, a trained NN is very fast in finding the output for a given input.

The adjustment and training process requires in-depth explanation and readers are provided with references [11, 92]. A great concern, however, is that a NN may be over trained. Cross validation and limiting the training cycles helps to prevent over training. An overly complex network with too many weights make cause the algorithm to be erratic and unreliable. The final architecture is highly dependent on the nature of the input data. Therefore, starting with a very simple network and then adding more neurons until low error on the training data and good cross validation performance is achieved is one method to obtain a reliable network [92].

4.5.3.1 Implementation of a Neural Network

Unlike mySVM which was developed elsewhere, the NN used in this study is developed by the author. Matlab's NN toolbox was utilized to efficiently implement a three hidden layer feed forward NN consisting of 10, 10, and 3 neurons in order from input to output. Since 112 values serve as input into the system, 24 node bias and 1253 weights between the nodes need to be determined to form a trained neural network. All nodes have a tan-sigmoid transfer function except the final output node which is a linear transfer function.

The weights and biases of the network are initialized with random values, taken from -1 to 1. The architecture of this neural network was found by starting with a 3 node, one layer network. Nodes were incrementally added to this layer but was not found to increase classification accuracy beyond 10 nodes. An additional 3 node layer was added. Increasing the number of nodes in this second layer did not produce an increase in accuracy beyond the 10th node. Finally, a third layer was added to created acceptable classification accuracy. While it may be possible that a comparable level of accuracy can be achieved by a three layer neural network with few nodes per layer, resolving the most optimal topology would require a more comprehensive search. Batch training was used: the weights between the nodes are updated only after all the training examples have been exposed to the network. Levenberg-Marquardt back-propagation was used in training. This type of back propagation was found in practice to provide the best results. While this training requires more memory, it is comparatively faster than other common training methods. Even so, training the NN is much slower than training the SVM. Where the SVM takes under a minute with 1800 training objects, the NN takes close to 20 minutes using the same computer.

One significant feature of the NN is that the inital weights and biases are random. Therefore, separate attempts to train with the same data will produce realizations of networks that have differing classification ability. In our experience, using a larger number of training samples helps to minimize but not completely remove the effects of unfortunate choices for initial weights and biases. The benefits of a large training set must also be weighed against the time needed by the forward model to generate the data. Therefore, for each set of training

data, NN is independently initialized and trained 10 times. The best performing NN is then selected for use.

4.6 Methodology

The study of using machine learning algorithms to infer an object's physical properties from associated B_k^j values of their response has four major steps to be discussed in the subsequent sections:

1. **Creation of Training Data**: SVM requires the B_k^j values of a large set of representative objects to form the training data. A large set is required to ensure that the trained SVM can generalize for all objects one may encounter. A forward model must be used to create this training data because is not normally possible to find and measure enough objects to create training data composed solely of real targets. Of the forward models available, the spheroid model is most suitable for the creation of the training data because it can predict the response of any arbitrary shaped spheroid target of any σ and μ value. This flexibility ensures the the training data will be broad and encompass many dissimilarly shaped objects.

2. **Creation of Test Data**: Unlike training data, test data need not be numerous and may be taken from forward models or from measurements. Synthetic test data, from forward models, may also include additive noise factors or other uncertainties which model the noise seen in measurement data.

3. **Obtaining B_k^j Values**: All synthetic data and measurement data are comprised of magnetic fields at various sensor locations. To form the appropriate inputs into the learning machines, the B_k^j values pertaining to the target must be extracted from these magnetic fields.

4. **Examining Accuracy of Trained Learning Machines**: Once the B_k^j values for the training data are obtained, the learning machines can be trained. Their level of error in classifying the test data will determine the ability of the learning machines to distinguish between objects with qualities similar to UXO from those with qualities unlike UXO. The effect of noise on classification accuracy is also investigated.

4.6.1 Object Modeling and Composition

This investigation uses three different object types. First, the simplest object is a single spheroid as shown in Figure 4-11(a). The spheroid has two possible permeability and conductivity values: either $\mu_r = 100$ with $\sigma = 2 \times 10^6$ S/m or $\mu_r = 1$ with $\sigma = 2 \times 10^7$ S/m. These values approximate steel and aluminum, two metals commonly present in UXO and clutter. The elongation of each spheroid, the ratio of major axis length to minor axis length, is taken from a uniform distribution ranging from 0.1 to 4. The volume is likewise random and uniformly distributed, ranging from 0.001 m^3 to 0.08 m^3 for all objects. The value of 0.04 m^3 is the cutoff between "large" and "small" objects. This range of values corresponds to the variety of UXO and clutter objects one would expect to encounter in the field. If different ranges of volumes are of interest, new training data can be created and the learn-

ing algorithms can be retrained to recognize different cutoff values. The orientation of the spheroids is always $\theta = 0$ rad with the axis of rotation parallel to the z axis.

These spheroids are modeled using the spheroid model. The main difficulty in the generation of synthetic data is the amount of time needed to create enough objects for the training set. To generate data for 1800 objects, around two days are needed on a 3.6 GHz Pentium 4 PC. While the computational time is substantial, the creation of the training data occurs infrequently: once a learning method is trained using a training data set, it may be repeatedly used to classify any object without requiring any further significant calculation. In this regard, classification by machine learning is much faster than identification by optimization which must proceed through the entire lengthy optimization process for every measurement with every library member.

The second type of object one can model is a heterogeneous object composed of two small spheroids that are coaxial and are separated by a distance of 1 mm as shown in in Figure 4-11(b). Thus the object is a body of revolution (BOR). Since it is composed of two different materials, it is referred to as a BOR composite object. This object is always positioned so that the gap is fixed at the center of the coordinate system. The two spheroids that form a composite object are always given two different permeability and conductivity values: $\mu_r = 100$ with $\sigma = 2 \times 10^6$ S/m and $\mu_r = 1$ with $\sigma = 2 \times 10^7$ S/m . The elongation of each spheroid is again random. The total volume of both spheroids ranges from 0.001 m^3 to 0.08 m^3. To obtain the response of a composite object, the magnetic field response of each spheroid is independently calculated and then summed. This study assumes that the

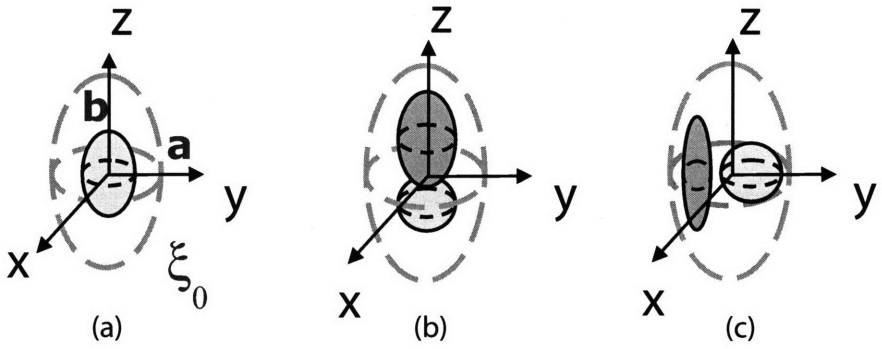

Figure 4-11: Three different configurations of spheroids: single, BOR composite, and non-BOR composite. The B_k^j of these three objects are used for SVM and NN training and testing.

interaction between the two spheroids does not affect the fields at the observation points which are at least a characteristic length away. As mentioned earlier, prior research has shown that this is a reasonable assumption even for closely spaced objects as long as one object is not permeable and the observation point is more than one characteristic object length away [73].

The third type of object under study is shown in Figure 4-11(c). This object is similar to the BOR composite object except now the axes are parallel to each other and the z-axis. The gap between the two spheroids is again 1mm and is positioned at the center of the coordinate system. This object is referred to as a non-BOR composite object.

The excitation calculated by the model of the GEM-3 sensor described in an earlier chapter. This model is validated and shown to be faster than other methods [78]. The GEM-3 instrument, the primary tool to produce EMI measurements, is manufactured by Geophex [93]. As mentioned earlier, this instrument consists of two current loop in a bucking coil arrangement to generated primary magnetic field. The secondary magnetic field is

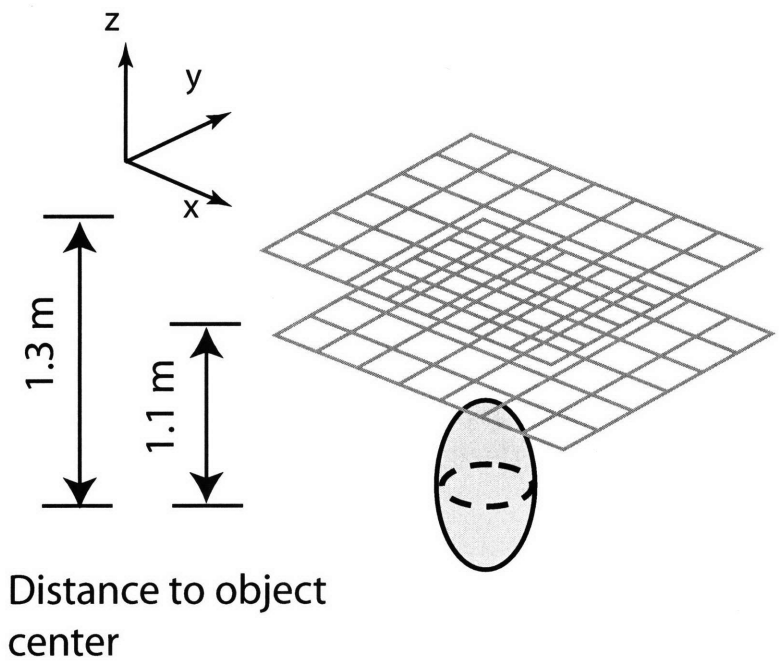

Figure 4-12: Diagram of the measurement locations used in the inversion process.

captured by the current generated on a pickup coil in the center of the instrument by $\partial B/\partial t$. However, the instrument reports this current in units that are proportional to the integral of magnetic flux over the receiver coil through a division by $i\omega$ of the receiver coil current as implemented in hardware and post-processing.

4.6.2 Retrieval of B_k^j from Magnetic Fields

For the training data and some of the test data, the B_k^j are recovered from magnetic fields generated from a forward model. The magnetic fields are sampled at at 578 points in space, thus ensuring the problem is overdetermined. These points were distributed over a 2 m by 2 m grid at two elevations, 1.1 m and 1.3 m from the center of the spheroid. Figure 4-12 gives a graphical depiction of this arrangement.

As before, only the lowest order modes are used, and they correspond to j = (0,0,1), (0,0,2), (0,1,1), (1,1,1), (0,0,3), (0,1,2), (1,1,2) and k = (0,0,0), (0,1,1), (1,1,1), (0,0,1), giving a total of 28 B_k^j coefficients. Previous work demonstrated that these low order modes dominate the solution and are sufficient to reproduce it [18]. The modes $(0,1,1),(1,1,1)$, and $(0,0,1)$ for k correspond to the magnetic dipole moments in x, y, and z directions for each excitation mode. Thus for each j, we are only solving for one more mode in addition to the three modes which correspond to the triaxial dipole moments. Each B_k^j is a complex value. But due to the limitations of the SVM algorithm, the real and imaginary parts are considered independent inputs when processing. For each object, we consider the B_k^j at two frequencies: one high at 10950 Hz and one low at 210 Hz. This choice of frequencies is due to the nature of the EMI response: these frequency extremes can capture the largest variation in an object's Inphase frequency response. Consequently, a vector of total length $n = 112$ serves as input for each object into the machine learning algorithm. This number is calculated from $28 \times 2 \times 2$, representing the 28 B_k^j , separated into real and imaginary parts, and at two frequencies.

The method of obtaining B_k^j from the magnetic fields can be applied to both measured data and synthetic data from a forward model that provides the EMI response of various objects. Both measured data and synthetic data are examined in the following sections.

It should also be stated that while it is true that one must know the actual location of objects to create the object-centered spheroidal coordinate system to solve for B_k^j , object position data can come from complementary techniques such as GPR. Furthermore,

subsequent sections show that this classification algorithm is robust enough to cope with a significant level of uncertainty in the object's position and orientation.

It should also be noted that since B_k^j comparisons must be made across many different objects, one needs to select one specific spheroidal coordinate system as the framework in which to retrieve B_k^j values. B_k^j values always pertain to a specified coordinate system as governed by the interfocal distance. The spheroid model supplies the B_k^j values in the spheroidal coordinate system which has the same interfocal distance as the target spheroid. However, the equivalent B_k^j values in a different spheroidal coordinate system can be found by calculating the expected secondary magnetic fields and solving for B_k^j in the new coordinate system as was done in Section 2.2.2.2.

4.7 SVM Classification Results

4.7.1 Large vs Small

For all tests, the training data is a set of 1800 objects that are evenly divided into the two possible classes of large and small. The test data set has 200 members and is generated independently from the training data set. Adequate classification can be achieved with as few as 600 training examples for the simple case of single spheroid test objects with no additive noise. However, past experience demonstrate that the more complex objects presented in the subsequent sections require larger training sets to be optimally classified. Therefore, to permit reasonable comparison of the classification performance for different objects, all

training sets have 1800 members. Many classification studies employ small training sets and larger test sets because the training sets, often derived from measurements and collected data, are difficult to obtain. However, the forward model can provide large amounts of training data within a reasonable amount of time so larger training sets are used.

In the first test, when single objects are classified by a trained SVM, only 2 objects are misclassified. Table 4.1 is the confusion matrix that of the result of classifying the test data. SVM misclassifies 2 objects out of a total of 200, yielding an error of 1%. For the sake of brevity, this error is used as the overall figure of merit as opposed to separate false positive and false negative rates. In most cases, the contribution to error was nearly equal between the false negatives and the false positives, or more appropriately false "small" and false "large" for classifying objects by size. The reader will be notified of cases where this observation is not true.

One can identify the members of the test data by assigned classification in the scatter plot shown in Figure 4-13. The horizontal axis of this plot is a rough metric for overall size of B_k^j while the vertical axis is the actual volume of the object. The errors made by SVM are concentrated close to the boundary between "large" and "small." While the clustering of markers suggests some correlation between object size and overall B_k^j magnitude, the relationship is not strict as we have discussed earlier. One can clearly see many large objects with lower B_k^j than smaller objects and visa versa.

Furthermore, the decision to use 28 B_k^j coefficients for each object comes about after examining the error rates created using more or fewer coefficients when classifying 200 single

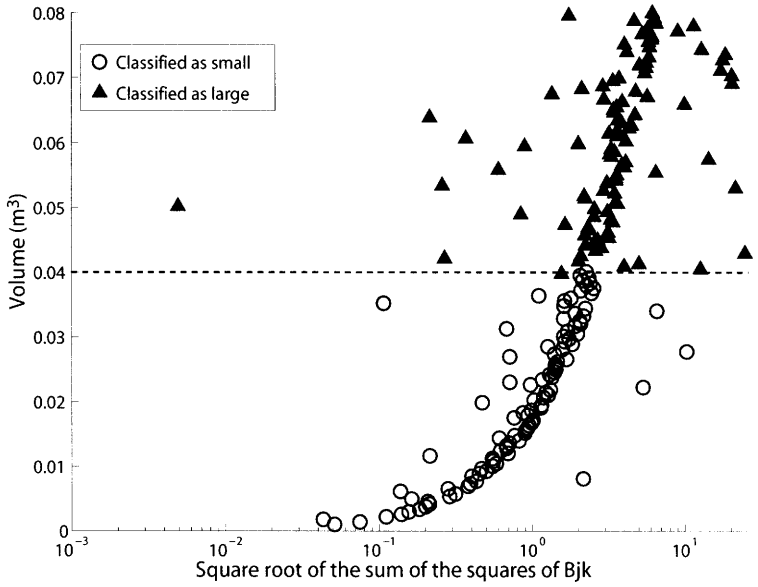

Figure 4-13: Scatter plot for SVM classification of single objects. Each marker represents one object, plotted against its corresponding true volume and square root of the sum of the squares of the 28 B_k^j used in classification. The marker's face is determined by its class as predicted by SVM. The horizontal dotted line represents the boundary between large and small objects.

Table 4.1: Confusion Matrix for SVM Classification of Single Objects

	True Large	**True Small**
Predicted Large	99	1
Predicted Small	1	99

Table 4.2: SVM Classification of Single Objects Using Various Number of Coefficients

	16 B_k^j	**28** B_k^j	**42** B_k^j
Percent Error	9.5%	1.0%	2.5%

spheroid objects as shown in Table 4.2. We aim to use the fewest, lowest order B_k^j coefficients that would still give good results. Recovering higher order B_k^j may be unreliable. This problem becomes even more apparent when recovering B_k^j from measured data [18]. However, using too few coefficients does not encapsulate enough information about the object and leads to higher classification error.

Table 4.3 shows how SVM is able to generalize for different types of objects. There are three sets of test data and three sets of training data. These three sets correspond to the three different types of objects as shown in Figure 4-11. All cases use 200 test objects and 1800 training objects. The lowest errors are generated when we train and test using the same type of object. When SVM is trained on single spheroids and tested on BOR composite objects or visa versa, it is able to generalize across these two object types to a certain degree. But it has difficulty classifying non-BOR objects when trained on any of the other two types or visa versa. For this table, the exact 50% errors were obtained when SVM simply classified all objects as large or all objects as small. A similar phenomenon created the 47.5% error where nearly all objects were classified as small. This unsuccessful classification may be due to the peculiarity of BOR objects in that they have values of zero for many specific B_k^j coefficients while non-BOR objects do not have this constraint [18]. Due to this very distinct difference in pattern, we expect SVM to have greater difficulty

Table 4.3: Table of Error for SVM Classification with Different Training and Testing Sets

	Train: Single (BOR)	**Train: Composite (BOR)**	**Train: Composite (non-BOR)**
Test: Single	1.00%	24.0%	50.0%
Test: Composite (BOR)	18.5%	3.00%	47.5%
Test: Composite (non-BOR)	50.0%	50.0%	1.50%

when generalizing across BOR and non-BOR objects.

However, when SVM is given sufficient training data, it can adequately classify all objects. Table 4.4 shows the effects of training on a combination of single and BOR composite objects and a combination of all three types of objects. Once again, the 50% error in this table is created when SVM classifies all objects as large. Remarkably, training on a combination of BOR composite and single objects allows SVM to be even more accurate in classifying BOR type objects. Furthermore, training with all three object types creates a more general SVM that can classify all objects with under 5% error.

For any classification technique to be of practical use, it must be able to generalize for a wide range of objects. Thus, this use of dissimilar training and testing objects characterizes the generalizability of each trained learning method. Furthermore, mixed training sets, comprised of two or more types of objects, helps to illustrate how broadening the scope of the training sets improves generalizability and leads to overall robustness.

Table 4.4: Table of Error for SVM Classification with Mixed Training Sets

	Train: Single and Composite (BOR)	**Train: All Three Types**
Test: Single	1.00%	2.50%
Test: Composite (BOR)	0.00%	4.50%
Test: Composite (non-BOR)	50.0%	4.50%

Table 4.5: Confusion Matrix for Neural Network Classification

	True Large	**True Small**
Predicted Large	99	0
Predicted Small	1	100

4.8 Comparison to Neural Network Classification

All the training and test data that are used to generate the results for SVM are also used for training and testing the implemented NN. Table 4.5 and Figure 4-14 show that the NN is able to achieve comparable and perhaps even slightly better results when compared to the SVM results for single spheroid classification.

Table 4.6 shows how well the NN is able to generalize for different objects. The NN has more difficulty generalizing for a test object type that differs from the training object type. While SVM trained on single objects produces an error rate of 18.5% when tested with composite objects, this error is significantly larger when the NN processes the same data. This suggests that our current NN has somewhat less ability to generalize between

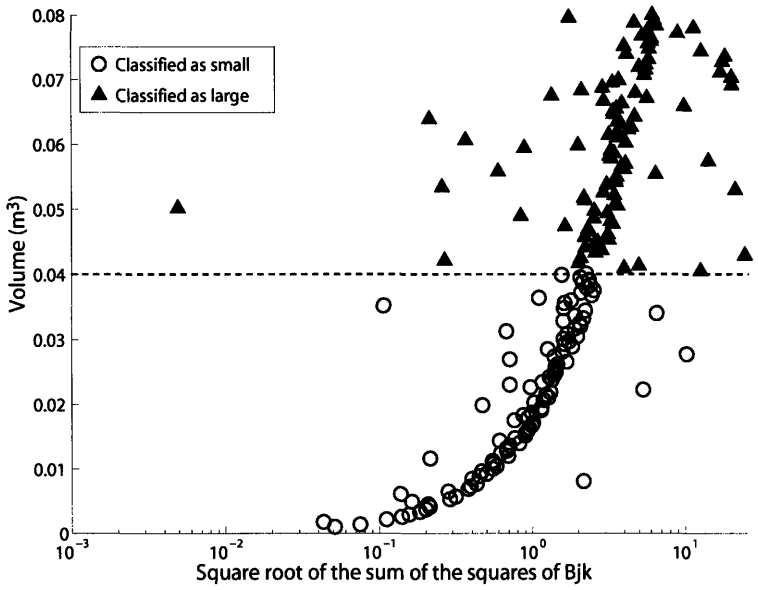

Figure 4-14: Scatter plot for NN classification of single objects. Each marker represents one object, plotted against its corresponding true volume and B_k^j magnitude. The marker's face is determined by its class as predicted by NN. The horizontal dotted line represents the boundary between large and small objects.

the single spheroid objects and the composite BOR object. However, once the NN is trained with all three types of objects, it is able to correctly classify all objects with low error as shown in Table 4.6. One interesting feature of the NN performance is that, unlike the SVM classification, the entries in the table where error is roughly 50% are created from nearly equal amounts of false "small" labels as false "large" labels.

4.9 Effect of Additive Gaussian Noise

As mentioned earlier, using dissimilar training and test objects is done to understand the limitations of each trained learning algorithm when exposed to entirely foreign objects. The wide variety of clutter objects and UXO makes understanding and minimizing this limitation

Table 4.6: Table of Error for NN Classification with Different Training and Testing Sets

	Train: Single (BOR)	**Train: Composite (BOR)**	**Train: Composite (non-BOR)**
Test: Single	0.500%	41.0%	50.5%
Test: Composite (BOR)	28.5%	1.50%	48.5%
Test: Composite (non-BOR)	49.0%	47.5%	3.50%

Table 4.7: Table of Error for NN Classification with Mixed Training Sets

	Train: Single and Composite (BOR)	**Train: All Three Types**
Test: Single	0.500%	1.50%
Test: BOR Composite	1.00%	3.00%
Test: non-BOR Composite	51.0%	2.00%

absolutely necessary for any classification technique to be of practical use. Another realistic obstacle to accurate classification is the effect of noise. This noise can be in the form of additive instrument noise and environmental noise which corrupts the received magnetic field. This noise in turn leads to small changes in the retrieved B_k^j coefficient. The relationship between the amount of change in seen B_k^j and the amount of noise in the EMI signal has already been investigated. Despite an addition of Gaussian noise that is 10% of the true field strength, B_k^j can be recovered accurately: for secondary responses at new measurement points, there is less than a 10% error between the direct prediction by forward models and the recovered B_k^j [18, 19]. For this investigation, it is then necessary for us to study how much that small change in B_k^j affects classification ability.

This study defines noise in terms of SNR, using additive Gaussian noise of 20dB SNR as an estimate of light background and instrument noise. First B_k^j are retrieved from noisy magnetic fields. Then the noise corrupted B_k^j are given to both the SVM and the NN. This study limits the investigation of additive noise effects to only single spheroid objects. The performance is outlined in Tables 4.8 and 4.9. Since the goal is to have both an SVM and a NN that can generalize for noisy data, we train both with clean training data, or noisy training data, or a combination of equal amounts of noisy and clean training data. In all cases, the training data is limited to 1800 members. Then noisy and clean test data are given to each trained learning algorithm. From the results it seems both NN and SVM have difficulty classifying noisy data if they are only trained on clean data. However, both methods have considerably lower error once they are trained on noisy data. NN is able to provide

Table 4.8: Table of Error for SVM Single Object with Noise

	Train: No Noise	**Train: 20dB SNR**	**Train: No Noise and 20dB SNR**
Test: No Noise	1.00%	4.00%	5.50%
Test: 20dB SNR	25.0%	8.50%	11.5%

Table 4.9: Table of Error for NN Single Object with Noise

	Train: No Noise	**Train: 20dB SNR**	**Train: No Noise and 20dB SNR**
Test: No Noise	0.500%	2.50%	2.00%
Test: 20dB SNR	24.0%	5.50%	5.00%

slightly lower error rates compared to SVM. Furthermore, training on noisy data does not cause NN to have any significant change in error rate when classifying clean data. Both methods show no further improvement if they are trained on both noisy and clean data. The effect of this training is confirmed when repeated on BOR and non-BOR composite objects as shown in Tables 4.10 and 4.11. Classification is much more difficult for composite objects. One can speculate that this phenomenon is due, in part, to the heavier reliance of the EMI response on higher order modes which are more difficult to recover accurately from noisy signals.

Table 4.10: Table of Error for Classification of BOR Composite with Noise

	SVM Train: 20dB SNR	**NN Train: 20dB SNR**
Test: No Noise	14.00%	9.50%
Test: 20dB SNR	17.00%	12.50%

Table 4.11: Table of Error for Classification of Non-BOR Composite with Noise

	SVM Train: 20dB SNR	**NN Train: 20dB SNR**
Test: No Noise	17.00%	12.00%
Test: 20dB SNR	20.50%	15.50%

4.10 Effect of Position Error

In the previous simulations, all objects were at fixed positions and aligned with the coordinate system. This arrangement, however, does not reflect real life situations where there may be uncertainties about the exact location of buried objects. It is therefore more realistic to estimate the location of an object and center the spheroidal coordinate system near the true center point of the target. This uncertainty will introduce noise into the recovered B_k^j coefficients. To study the effects of that noise, we recover the B_k^j from single spheroids which have four types of misalignments in position and orientation from the origin and orientation of the assumed coordinate system: depth deviation in z, lateral deviation in x, rotational deviation in θ, and rotational deviation in ϕ. These four types are summarized in Figure 4-15. The volumes and material properties of the objects are otherwise similar to the previous cases of single spheroids. From the modeled data, the B_k^j are inverted using an assumed coordinate system that is misaligned by a specified deviation. The deviation is generated randomly using a uniform distribution. Both training and test data are generated in this manner. While the NN shows slight improvement over the SVM, the significantly longer training time made the algorithm unattractive in for additional investigations where the permissible ranges of variation in x, z, θ, ϕ were not very well known. Therefore, the

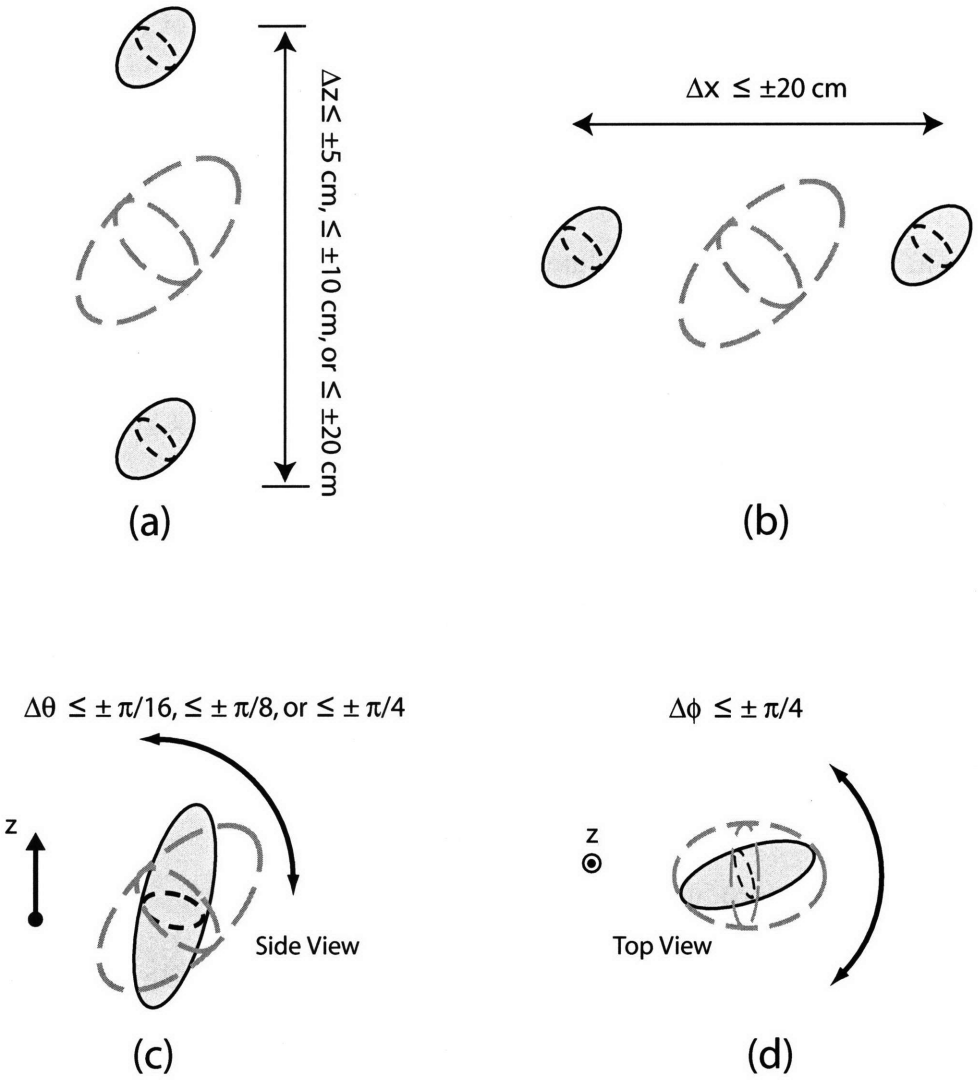

Figure 4-15: Figure showing the bounds on (a) z variation, (b) x variation, (c) θ variation, and (d) ϕ variation in the study on position and orientation uncertainty. All objects have random volumes, dimensions, and material properties.

SVM was chosen as the learning algorithm in this portion of the investigation.

For z variation, the centers of the spheroids are allowed to vary within a ± 5 cm range of random deviation (up to 5 cm below and above the center of the assumed coordinate system), a ± 10 cm range of random deviation, or a ± 20 cm range of random deviation, as depicted in Figure 4-15 (a). The object and the coordinate system are kept at a fixed θ angle of $\pi/4$ and a fixed ϕ angle of 0. While the dimensions of the modeled objects are determined randomly from a range of possible volumes and elongations, the largest possible dimension of the spheroids is 1 m.

Table 4.12 reports the errors for different combinations of testing and training data. As in the additive Gaussian noise cases, training with noisy data improves SVM's ability to classify noisy test data. We see that our method tolerates a ± 5 cm variation quite well with under 10% error when we use noisy training data drawn from either the ± 5 cm and ± 10 cm ranges. When the training data is drawn from the ± 5 cm range, our methods can obtain an under 10% error for ± 10 cm range test data. An uncertainty of ± 20 cm in either the training or the test data produces significantly less accurate results.

Next, we examine the effect of lateral deviation. Here the objects are permitted up to a ± 20 cm deviation in the x direction from the fixed center of the coordinate system. The object and the coordinate system are kept at a fixed θ angle of $\pi/4$ and a fixed ϕ angle of 0. This arrangement is depicted in Figure 4-15 (b). From Table 4.13, we see that a large lateral uncertainty has a much smaller effect than an equally large vertical uncertainty.

The third type of variation concerns object orientation. The coordinate system is oriented

Table 4.12: Table of Error for SVM with Z Position Deviation

	Train: No Deviation	**Train: ±5 cm Deviation**	**Train: ±10 cm Deviation**	**Train: ±20 cm Deviation**
Test: No Deviation	1.00%	2.00%	2.00%	7.00%
Test: ±5 cm Deviation	12.0%	1.50%	3.50%	38.0%
Test: ±10 cm Deviation	46.0%	7.50%	10.5%	21.5%
Test: ±20 cm Deviation	44.0%	22.0%	16.0%	36.0%

Table 4.13: Confusion Matrix for SVM Classification of X Position Deviation 20 cm

	True Large	**True Small**
Predicted Large	96	4
Predicted Small	4	96

Table 4.14: Table of Error for SVM with θ Orientation Deviation

	Train: No Deviation	**Train: $\pm\pi/16$ Deviation**	**Train: $\pm\pi/8$ Deviation**	**Train: $\pm\pi/4$ Deviation**
Test: No Deviation	1.00%	1.00%	3.50%	4.50%
Test: $\pm\pi/16$ Deviation	2.00%	2.00%	1.50%	3.00%
Test: $\pm\pi/8$ Deviation	1.50%	7.00%	1.50%	4.50%
Test: $\pm\pi/4$ Deviation	4.50%	4.50%	4.00%	6.00%

Table 4.15: Confusion Matrix for SVM Classification of ϕ Orientation Deviation

	True Large	**True Small**
Predicted Large	87	0
Predicted Small	13	100

at $\theta = \pi/4$ but the object's θ is permitted to vary up to $\pm\pi/16$, $\pm\pi/8$, and $\pm\pi/4$ from $\pi/4$. The ϕ angle is fixed at 0. This arrangement is depicted in Figure 4-15 (c). Table 4.14 shows that variation in θ orientation does not have a significant impact on the classification accuracy.

The final type of variation concerns object orientation in the ϕ direction. The coordinate system is oriented at $\phi = 0$ but the object's ϕ is permitted to vary up $\pm\pi/4$ from 0. The θ angle is fixed at $\pi/4$. This arrangement is depicted in Figure 4-15 (d). Table 4.15 shows that variation in ϕ orientation creates a classification error of 6.5% which is on par with the θ variation scenarios. The classification errors for all orientation variations are under 10%.

These results suggest that a depth accuracy of under 10 cm should be achieved to create

Table 4.16: Confusion Matrix for SVM Classification of Clutter Items and UXO

	True Large (UXO)	**True Small (Clutter)**
Predicted Large	4	0
Predicted Small	0	4

a viable solution for UXO discrimination. In addition, these results indicate that the larger effort should be placed in accurately resolving an object's depth rather than finding an object's orientation and x, y location with great precision.

4.11 SVM Results with Measurements

The SVM classification is then tested using data from measured objects. The B_k^j values were obtained from four UXO shown in Figure 3-4. Futhermore, the B_k^j values were obtained from clutter item 7 to 10 of Figure 4-1. The largest clutter item has a volume of 53 cm^3. The largest UXO has a volume of roughly 2000 cm^3 while the smallest has a volume of about 700 cm^3. Therefore, a new SVM training set with added Gaussian noise was created where the random spheroids had volumes within the range of 10 cm^3 to 2500 cm^3 with 300 cm^3 as the boundary between small and large. When the trained SVM was presented with B_k^j drawn from measurements of these four objects, it correctly distinguished the very large objects from the small objects as shown by Table 4.16.

Table 4.17: Confusion Matrix for SVM Classification of BOR Items and non-BOR Items

	True BOR	**True non-BOR**
Predicted BOR	100	0
Predicted nonBOR	0	100

4.11.1 BOR vs Non-BOR

Distinguishing BOR composite objects from non-BOR composite objects is another area of investigation. The 1800 member training data has equal parts BOR and non-BOR composite spheroids. When trained on this data, SVM is very accurate in classifying a similarly generated 200 member test set as seen in Table 4.17. This accuracy is likely due to the distinct and easily distinguishable pattern for the B_k^j of BOR objects. In BOR objects, only specific low order B_k^j are non-zero [18].

4.11.2 Homogeneous vs Heterogeneous

Investigation into the ability to distinguish homogeneous composite spheroids from heterogeneous composite spheroids is conducted in much the same way. Homogeneous composite spheroids are formed from two steel or two aluminum spheroids. Heterogeneous objects are formed from one steel and one aluminum spheroid. Steel has $\mu_r = 100$ with $\sigma = 2 \times 10^6$ S/m, and aluminum has $\mu_r = 1$ with $\sigma = 2 \times 10^7$ S/m as indicated in previous sections. All composite objects are BOR in shape. Once again, a 1800 member training set and 200 member test set are used. As shown in Table 4.18, classification accuracy is somewhat less than in previous cases and indicates a possible area for future study.

Table 4.18: Confusion Matrix for SVM Classification of Homogeneous and Heterogeneous Items

	True Homog.	**True Heterog.**
Predicted Homog.	71	1
Predicted Heterog.	29	99

4.12 Conclusion

In this chapter the problem of classification by volumetric size and other physical characteristics of metallic objects using their EMI response is solved by decomposing that response into B_k^j coefficients and then using a SVM and a NN to process those coefficients. The performance of each method is compared. Since one can demonstrate that there is no simple relationship between sizes of objects and the overall magnitude of their B_k^j coefficients and magnetic polarizabilities, learning algorithms may be useful in classifying these objects. Furthermore, both learning algorithms are able to generalize for different object types with varying degrees of success. Both algorithms are capable of classifying single objects when trained on BOR composite objects or visa versa. However, both have difficulty classifying non-BOR objects when trained on any of the other two types or visa versa. One can hypothesize that this increased error is due to the single spheroid also being BOR so the non-BOR objects are very different from the other two types. When trained on all three types of objects, both the NN and the SVM are able to classify all objects with a good degree of accuracy. Futhermore, screening out non-BOR objects from BOR objects can be done with high accuracy so that, theoretically, classification based on size need not encompass both BOR and non-BOR objects.

Some investigation is also conducted in classification by object heterogeneity or BOR characteristics with encouraging results. One aspect of machine learning which has not been included in this study is the topic of feature selection. The 28 low order B_k^j at two selected frequencies are an educated guess for which B_k^j are the most significant in classification. However, there may be more optimal subset of these B_k^j values at the currently used frequencies or other frequencies which serve as better inputs into learning machines. This facet of machine learning research is called "feature selection" [39] and may be a possible area for future work.

Furthermore, there is a possibility of developing this technique into a real time application. Training each learning method is not instantaneous but still within the realm of being practical. Once a learning algorithm is trained, it can be used for an extended period of time until the user feels more accurate training data is available. Therefore training need only be a rare occurence.

Generating synthetic training data is the most time consuming part of our research, but this data can be stored and used as long as the researcher deems the training data to be valid. The actual classification of test data by SVM or NN is nearly instantaneous. Solving for the appropriate B_k^j from measurements is also nearly instantaneous. Therefore, classification of a buried object as UXO or a piece of clutter can theoretically be obtained as quickly as the EMI measurements can be completed when the object position and orientation are known or are estimated within bounds such as those indicated earlier.

In addition, both methods show an ability to generalize for noisy test data when trained

with noisy data. This noise can be in the form of additive Gaussian noise or small variations in the position or orientation of the objects relative to the coordinate system. Training on noisy data helps to increase the accuracy of both learning algorithms when classifying objects with noisy B_k^j . In the analysis on the effects of uncertainty in object position and orientation, one can see that large deviations in an object's depth can significantly decrease the SVM classification accuracy. Since accuracy with noisy measured data is very critical for any classification method to be viable in the field, one can conclude that training must always be done using data with added noise and uncertainty to help increase the robustness of the classification method. However, this classification method and the DE optimization method described in the previous chapter have limitations in regards to the level of noise in the EMI responses. Various clutter suppression or signal separation [41] methods have been advanced. Integrating such methods into these inversion algorithms will further the work in realizing a practical, field deployable solution to the difficult problem of UXO inversion.

Chapter 5

Conclusion

This thesis covers both modeling and inversion of UXO. The modeling portion of the study focused on increasing accuracy over existing UXO models through more sophisticated modeling techniques and through accounting for the natural environment. It is concluded that permeable soil has very little effect on the response of buried UXO. The effect is essentially limited to a constant Inphase offset. Characterization and calibration of a non-adaptive sensor is also found to be possible when using measurements of canonical objects.

Identification of UXO is shown to be feasible when utilizing Differential Evolution. Through this method a target, its position, and orientation can be identified by comparing with library of specific object models. This identification process is shown to be accurate for low clutter conditions and for targets buried at shallow depths. However, Differential Evolution is slow and requires a comprehensive library.

Classification of UXO is shown to be possible through application of machine learning on the B_k^j of the target objects. These B_k^j can be used to distinguish between general UXO

and clutter. Use of both Support Vector Machines and Neural Networks creates accurate classifiers which can distinguish between objects physically resembling UXO from those which do not resemble UXO. Both of these classifiers, once trained, are fast and can be potentially used for in-situ, real time inversion. However, the great drawback of classification through the use of B_k^j is the requirement that an estimation of target position must be obtained beforehand.

There is research into methods to reduce noise and to estimate object location and orientation from measurement data. Therefore, both of these inversion methods may be improved up in the future to produce a practical discriminator for the important task of UXO remediation.

Bibliography

[1] *MPI: The Complete Reference (Vol.1), 2nd Edition.* The MIT Press, 1998.

[2] *MPI: The Complete Reference (Vol.2).* The MIT Press, 1998.

[3] C. O. Ao. *Electromagnetic Wave Scattering by Discrete Random Media with Remote Sensing Application.* PhD thesis, Massachusetts Institute of Technology, January 2001.

[4] C. O. Ao, H. Braunisch, K. O'Neill, and J. A. Kong. Quasi-magnetostatic solution for a conducting and permeable spheroid with arbitrary excitation. *IEEE Trans. on Geoscience and Remote Sensing*, 40(4):887–897, April 2002.

[5] B. E. Barrowes. *Electromagnetic Scattering and Induction Models for Spheroidal Geometries.* PhD thesis, Massachusetts Institute of Technology, January 2004.

[6] B. E. Barrowes, K. O'Neill, T. M. Grzegorczyk, X. Chen, and J. A. Kong. Broadband electromagnetic induction solution for a conducting and permeable spheroid. *IEEE Trans. on Geoscience and Remote Sensing*, 42:2479–2489, November 2004.

[7] C. E. Baum. *Detection and Identification of Visually Obscured Targets.* Taylor and Francis, 1998.

[8] L. P. Beard and J. E. Nyquist. Simultaneous inversion of airborne electromagnetic data for resistivity and magnetic permeability. *Geophysics*, 63(5):1556–1564, September-October 1998.

[9] T. Bell, B. Barrow, J. Miller, and D. Keiswetter. Time and frequency domain electromagnetic induction signatures of unexploded ordnance. *Subsurface Sensing Technologies and Applications*, 2(3):153–175, 2001.

[10] T. H. Bell, B. J. Barrow, and J. T. Miller. Subsurface discrimination using electromagnetic induction sensors. *IEEE Trans. on Geoscience and Remote Sensing*, 39(6):1286–1293, June 2001.

[11] C. Bishop. *Neural Networks for Pattern Recognition.* Clarendon Press, 1995.

[12] H. Braunisch. *Methods in Wave Propagation and Scattering.* PhD thesis, Massachusetts Institute of Technology, February 2001.

[13] H. Braunisch, C. O. Ao, K. O'Neill, and J. A. Kong. Magnetoquasistatic response of a distribution of small conducting and permeable objects. pages 1424–1426. Geoscience and Remote Sensing Symposium, IEEE, 2000.

[14] E. C. Brevik, T. E. Fenton, and A. Lazari. Soil electrical conductivity as a function soil water content and implications for soil mapping. *Precision Agriculture*, 7(5):393–404, December 2006.

[15] C. Bruschini. On the low-frequency EMI response of coincident loops over a conducting and permeable soil and corresponding background reduction schemes. *IEEE Transactions on Geoscience and Remote Sensing*, 42:1706–1719, 2004.

[16] Dwain Butler. Implications of magnetic backgrounds for unexploded ordnance detection. *Journal of Applied Geophysics*, 54:111–125, 2003.

[17] Y. L. Chang, L. S. Liang, C. C. Han, J. P. Fang, W. Y. Liang, and K. S. Chen. Multisource data fusion for landslide classification using generalized positive boolean functions. *IEEE Transactions on Geoscience and Remote Sensing*, 45(6):1697–1702, June 2007.

[18] X. Chen. *Inverse Problems in Electromagnetic.* PhD thesis, Massachusetts Institute of Technology, May 2005.

[19] X. Chen, K. O'Neill, T. M. Grzegorczyk, and J. A. Kong. Spheroidal mode approach for the characterization of metallic objects using electromagnetic induction. *IEEE Trans. on Geoscience and Remote Sensing*, 45(3):697–706, March 2007.

[20] S. Chikazumi. *Physics of Magnetism.* Wiley, 1964.

[21] T. Chiu and K. Sarabandi. Electromagnetic scattering interaction between leaves and thin branches. pages 300–302. Geoscience and Remote Sensing Symposium IGARSS, IEEE, 1998.

[22] M. Combrinck. *Development of an automated analysis of TDEM data for the delineation of a finite conductor in a conducting half space.* PhD thesis, University of Pretoria, 2006.

[23] Y. Das. A preliminary investigation of the effects of soil electromagnetic properties on metal detectors. volume 5415 of *Detection and Remediation Technologies for Mines and Minelike Targets IX.* SPIE, April 2004.

[24] Y. Das. Electromagnetic induction response of a target buried in conductive magnetic soil. volume 5794 of *Detection and Remediation Technologies for Mines and Minelike Targets X.* SPIE, March 2005.

[25] Y. Das. Effects of soil electromagnetic properties on metal detectors. *IEEE Trans. on Geoscience and Remote Sensing*, 44:1444–1453, June 2006.

[26] Y. Das. Time-domain response of a metal detector to a target buried in soil with frequency-dependent magnetic susceptibility. volume 6217 of *Detection and Remediation Technologies for Mines and Minelike Targets XI.* SPIE, April 2006.

[27] Y. Das. Effects of magnetic soil on metal detectors - preliminary experimental results. volume 6553 of *Detection and Remediation Technologies for Mines and Minelike Targets XII.* SPIE, April 2007.

[28] Y. Das and J. E. McFee. A simple analysis of the electromagnetic response of buried conducting objects. *IEEE Transactions on Geoscience and Remote Sensing*, 29(2):342–344, March 1991.

[29] R. Duda, P. Hart, and D. Stork. *Pattern Classification.* Wiley, 2001.

[30] B. P. D'Yakonov. The diffraction of electromagnetic waves by circular cylinder in a homogeneous half-space. *Bull. Acad. Sci.*, (9):950–955, 1959.

[31] E. B. Fails, P. A. Torrione, W. R. Scott, and L. M. Collins. Performance of a four parameter model for modeling landmine signatures in frequency domain wideband electromagnetic induction detection systems. volume 6553 of *Detection and Remediation Technologies for Mines and Minelike Targets XII Conf.*, Orlando, FL, 2007. SPIE.

[32] D. E. Ferguson. Fibonaccian searching. *Communications of the ACM*, 3(12):648, 1960.

[33] J. P. Fernandez, B. Barrowes, K. O'Neill, I. Shamatava, F. Shibitidze, and K. Sun. A data-derived time domain sea for uxo detection using the mpv sensor. volume 6953 of *Detection and Sensing of Mines, Explosive Objects, and Obscured Targets XIII.* SPIE, 2008.

[34] C. Flammers. *Spheroidal Wave Functions.* Stanford University Press, 1957.

[35] D. Fraser and G. Hodges. Induction-response functions for frequency-domain electromagnetic mapping system for airborne and ground configurations. *Geophysics*, 72(2):F35–F44, March-April 2007.

[36] D. C. Fraser. Magnetite mapping with a multicoil airborne electromagnetic system. *Geophysics*, 46(11):1579–1593, November 1981.

[37] N. Geng, K. E. Baum, and L. Carin. On the low frequency natural responses of conducting and permeable targets. *IEEE Trans. on Geoscience and Remote Sensing*, 37:347–359, January 1999.

[38] V. George and T. W. Altshuler. *Summary of the DARPA background clutter data collection experiment.* Ultra- Wideband, Short-Pulse Electromagnetics 4. Kluwer Academic, 1999.

[39] I. Guyon and A. Elisseeff. An introduction to variable and feature selection. *Journal of Machine Learning Research 3*, March 2003.

[40] H. A. Haus and J. R. Melcher. *Electromagnetic Fields and Energy.* Prentice Hall, 1989.

[41] W. Hu, S. L. Tantum, and L. Carin. Emi-based classification of multiple closely spaced subsurface objects via independent component analysis. *IEEE Trans. on Geoscience and Remote Sensing*, 42:2544–2554, November 2004.

[42] H. Huang and D. C. Fraser. Airborne resistivity and susceptibility mapping in magnetically polarizable areas. *Geophysics*, 65(2):502–511, March-April 2000.

[43] H. Huang, B. SanFilipo, and I. J. Won. Optimizing decision threshold and weighting parameters for uxo discrimination. *Geophysics*, 71(6):G313–G320, November-December 2006.

[44] H. Huang and I. J. Won. Conductivity and susceptibility mapping using broadband electromagnetic sensors. *Journal of Environmental Engineering and Geophysics*, 5(4):31–41, December 2000.

[45] Haoping Huang. Detecting metal objects in magnetic environments using a broadband electromagnetic method. *Geophysics*, 68(6):1877–1887, November-December 2003.

[46] A. A. Kaufman. *Geophysical Field Theory and Method, Part C: Electromagnetic Fields II.* Academic Press, 1994.

[47] G. W. C. Kaye and T. H. Laby. *Tables of Physical and Chemical Constants.* Longman Science and Technology, 1995.

[48] D. A. Keiswetter, I. J. Won, J. Miller, and T. Bell. Discriminating capabilities of multifrequency EMI data. volume 4 of *Geoscience and Remote Sensing Symposium (IGARSS)*, pages 1415–1417. IEEE, July 2000.

[49] D. K. Keiswetter, I. J. Won, B. Barrow, and T. Bell. Object identification using multi-frequency EMI data. In *Proc. UXO Forum.* 1999.

[50] J. A. Kong. *Electromagnetic Wave Theory.* EMW Publishing, Cambridge, MA, 2000.

[51] T. Lee and L. Thomas. The transient electromagnetic response of a polarizable sphere in a conducting halfspace. *Geophysical Prospecting*, 40(5):541–563, 1992.

[52] E. L. Miller, C. M. Rappaport, and G. D. Sower. A multiscale, statistically based inversion scheme for linearized inverse scattering problems. *IEEE Transactions on Geoscience and Remote Sensing*, 34(2):346–357, March 1996.

[53] C. D. Moss. *Numerical Methods for Electromagnetic Wave Propagation and Scattering in Complex Media.* PhD thesis, Massachusetts Institute of Technology, January 2004.

[54] C. D. Moss, T. M. Grzegorczyk, J. A. Kong, and K. O'Neill. A hybrid time domain solution of electromagnetic induction scattering from axisymmetric objects. page 308, Honolulu, Hawaii, October 2003. Progress in Electromagnetic Research Symposium (PIERS).

[55] C. D. Moss, K. O'Neill, T. M. Grzegorczyk, and J. A. Kong. A hybrid time domain method to calculate electromagnetic induction scattering from targets with arbitrary skin depth. pages 390–396. Applied Computational Electromagnetics (ACES), March 2003.

[56] Office of the Under Secretary of Defense. Report of the Defense Science Board Task Force on Unexploded Ordnance. December 2003.

[57] A. A. Osharin. Plane electromagnetic wave scattering by a spherical inclusion embedded in a lossy half-space. *SPIE: International conference on millimeter and submillimeter waves and applications*, 3465:502–508, July 1998.

[58] G. Paliouras, K. Vangelis, and C. D. Spyropoulos, editors. *Machine Learning and Its Applications.* Springer, 2001.

[59] L. Pasion, D. W. Oldenburg, S. D. Billings, and D. Sinex. Soil compensation techniques for the detection of buried metallic objects using electromagnetic sensors. *SPIE: Detection and Remediation Technologies for Mines and Minelike Targets XII*, 6553, 2007.

[60] R. Plamondon and S. N. Srihari. Online and off-line handwriting recognition: A comprehensive survey. *IEEE Transactions on Pattern Analysis and Machine Intelligence*, 22(1):63–84, January 2000.

[61] H. Preetz, S. Altfelder, and J. Igel. Tropical soils and landmine detection–an approach for a classification system. *Soil Sci. Soc. Am. J.*, 72(1):151–159, January-February 2008.

[62] K. Price, R. Storn, and J. Lampinen. *Differential Evolution.* Springer, 2005.

[63] M. Raza, I. Gondal, D. Green, and R. L. Coppel. Feature selection and classification of gene expression profile in hereditary breast cancer. In *Hybrid Intelligent Systems*, pages 315–320. IEEE Computer Society, 2004.

[64] E. Rey and D. Jongmans. A 2D numerical study of the effect of particle shape and orientation on the resistivity in shallow formations. *Geophysics*, 72(1):F9–F17, January-February 2007.

[65] S. Ruping. *mySVM-Manual.* University of Dortmund, Lehrstuhl Informatik 8 edition, 2000. http://www-ai.cs.uni-dortmund.de/SOFTWARE/MYSVM/index.html.

[66] A. Salem, T. Hamada, J. Asahina, and K. Ushijima. Detection of unexploded ordnance (uxo) using marine magnetic gradiometer data. *Exploration Geophysics*, 36:97–103, 2005.

[67] R. A. Schill Jr. General relation for the vector magnetic field of a circular current loop: A closer look. *IEEE Transactions on Magnetics*, 39(2):961–967, March 2003.

[68] B. Scholkopf, C. J. C. Burges, and A. Smola, editors. *Advances in Kernel Methods: Support Vector Learning.* MIT Press, 1999.

[69] G. Schultz and C. Ruppel. Inversion of inductive electromagnetic data in highly conductive terrains. *Geophysics*, 70(1):G16–G28, January-February 2005.

[70] I. Shamatava, F. Shubitidze, C. C. Chen, H. S. Youn, K. O'Neill, and K. Sun. Potential benefits of combining emi and gpr for enhanced uxo discrimination at highly contaminated sites. volume 5415 of *Proceedings of SPIE - The International Society for Optical Engineering*, pages 1201–1210, 2004.

[71] F. Shubitidze, K. O'Neill, S. A. Haider, K. Sun, and K. D. Paulsen. Application of the method of auxiliary sources to the wide-band electromagnetic induction problem. *IEEE Trans. on Geoscience and Remote Sensing*, 40:928–942, April 2002.

[72] F. Shubitidze, K. O'Neill, K. Sun, and I. Shamatava. Interaction between highly conducting and permeable metallic objects in the emi frequency range. pages 625–631. Annual Review of Progress in Applied Computational Electromagnetics, 2003.

[73] F. Shubitidze, K. O'Neill, K. Sun, I. Shamatava, and K. D. Paulsen. A hybrid full MAS and combined MAS/TSA algorithm for electromagnetic induction sensing. volume 19, pages 112–126. ACES(Applied Computational Electromagnetics Society) Journal, 2004.

[74] J. E. Simms, R. L. Van Dam, and J. M. H. Hendrickx. Classification of magnetic susceptibility anomalies and their relevance to uxo detection. *FastTIMES*, 10(2):48–51, 2005.

[75] W. R. Smythe. *Static and Dynamic Electricity.* McGraw-Hill, 3rd edition, 1968.

[76] J. A. Stratton. *Electromagnetic Theory.* McGraw-Hill, 1941.

[77] K. Sun, K. O'Neill, B. E. Barrowes, J. P. Fernandez, F. Shubitidze, I. Shamatava, and K. D. Paulsen. Dumbbell dipole model and its application in UXO discrimination. volume 6217. SPIE, April 2006.

[78] K. Sun, K. O'Neill, I. Shamatava, and F. Shubitidze. Application of prolate spheroid solutions in simulation of EMI scattering with realistic sensors and objects. pages 531–537. Applied Computational Electromagnetics (ACES), March 2003.

[79] K. Sun, K. O'Neill, F. Shubitidze, I. Shamatava, and K. D. Paulsen. Fast data-derived fundamental spheroidal excitation models with application to UXO discrimination. *IEEE Trans. on Geoscience and Remote Sensing*, 43:2573–2583, November 2005.

[80] S. L. Tantum, Y. Yu, and L. M. Collins. Bayesian mitigation of sensor position errors to improve unexploded ordnance. *IEEE Transactions on Geoscience and Remote Sensing Letters*, 5(1), January 2008.

[81] A. B. Tarokh, E. L. Miller, and I. J. Won. Statistical classification of buried objects from spatially sampled time or frequency domain emi data. *Radio Science*, 39(4), July-August 2004.

[82] L. Tsang, J. A. Kong, and R. T. Shin. *Theory of microwave remote sensing.* Wiley, 1985.

[83] J. van Bladel. *Electromagnetic Fields.* Hemisphere Pub. Corp., 1985.

[84] R. L. van Dam, J. M. H. Hendrickx, and B. et al Harrison. Spatial variability of magnetic soil properties. *SPIE: Detection and Remediation Technologies for Mines and Minelike Targets IX*, 5415, 2004.

[85] V. Vapnik. *Statistical Learning Theory.* Wiley, 1998.

[86] S. K. Verma and R. N. Singh. Transient electromagnetic response of an inhomogeneous conducting sphere. *Geophysics*, 35(2):331–336, April 1970.

[87] J. R. Wait. A conducting sphere in a time varying magnetic field. *Geophysics*, 16:666–672, 1951.

[88] J. R. Wait. *Electromagnetic Wave Theory.* Harper and Row, 1985.

[89] J. R. Wait and K. P. Spies. Quasi-static transient response of a conducting permeable sphere. *Geophysics*, 34(5):789–792, 1969.

[90] H. Wechsler. *Reliable Face Recognition Methods: System Design, Implementation and Evaluation.* Springer, 2006.

[91] D. Williams, Y. Yu, L. Kennedy, X. Zhu, and L. Carin. A bivariate gaussian model for unexploded ordnance classification with emi data. *IEEE Transactions on Geoscience and Remote Sensing Letters*, 4(4):629–633, October 2007.

[92] P. H. Winston. *Artificial Intelligence.* Addison-Wesley, 1993.

[93] I. J. Won, D. A. Keiswetter, and D. R. Hansen. GEM-3: A monostatic broadband electromagnetic induction sensor. *J. Environ. Eng. Geophys.*, 2:53–64, 1999.

[94] X. Xu, E. L. Miller, C. M. Rappaport, and G. D. Sower. Statistical method to detect subsurface objects using array ground-penetrating radar data. *IEEE Transactions on Geoscience and Remote Sensing*, 40(4):963–976, April 2002.

[95] C. Yin and G. Hodges. Simulated annealing for airborne em inversion. *Geophysics*, 72(4):F189–F195, July-August 2007.

[96] B. Zhang, K. O'Neill, T. M. Grzegorczyk, and J. A. Kong. Environmental effects on UWB electromagnetic induction inversion techniques and forward modeling of unexploded ordnance. page 127, Cambridge, Massachusetts, March 2006. Progress in Electromagnetic Research Symposium (PIERS).

[97] B. Zhang, K. O'Neill, T. M. Grzegorczyk, and J. A. Kong. Use of EMI response coefficients from spheroidal excitation and scattering modes to classify objects via SVM. volume 6217. SPIE, April 2006.

[98] B. Zhang, K. O'Neill, T. M. Grzegorczyk, and J. A. Kong. Support vector machine and neural network classification of metallic objects using coefficients of the spheroidal mqs response modes. *IEEE Trans. Geosci. and Remote Sens.*, 46(1):159–171, January 2008.

[99] Y. Zhang, L. Collins, H. Yu, C. E. Baum, and L. Carin. Sensing of unexploded ordnance with magnetometer and induction data: Theory and signal processing. *IEEE Trans. on Geoscience and Remote Sensing*, 41:1005–1015, May 2003.

[100] Z. Zhang and D. W. Oldenburg. Recovering magnetic susceptibility from electromagnetic data over a one-dimensional earth. *Geophys J. Int.*, 130:422–434, 1997.

[101] Z. Zhang and D. W. Oldenburg. Simultaneous reconstruction of 1-d susceptibility and conductivity from electromagnetic data. *Geophysics*, 64(1):33–47, January-February 1999.